MONASH University

Back-Contact Perovskite Solar Cells

Dorota Malwina Bacal

BEng. MSc.

A thesis submitted for the degree of *Doctor of Philosophy* at

Monash University in 2020

Department of Chemical Engineering

Under the Supervision of

Prof. Udo Bach

Dr. Doojin Vak

February 2020

Copyright notice

Abstract

The discovery of the perovskite photovoltaic material family in 2009 has shaken the world of solar cell research. As of today, perovskite solar cells (PSCs) have demonstrated efficiencies comparable to commercially available silicon devices and have the potential to become a viable marketplace alternative in the near future. In the world of fast approaching disaster caused by the global warming, any engineering solution allowing us to ease the transition to renewable energy production is desirable. Therefore, a core theme of the Thesis is to find ways to increase the efficiency of PSCs, thus make them more viable for large scale production.

A regular PSC consists of a photoactive perovskite material "sandwiched" in between two charge selective layers and electrodes. The structure used in this Thesis utilises quasi-interdigitated back-contact electrodes (QIBC), developed in collaboration between CSIRO and our research group. This architecture allows for a range of *in situ* measurements that are presented in this Thesis, which aim to understand the fundamental mechanisms of perovskite crystal growth and passivation.

The Introduction to this Thesis presents a review on the current status of global warming, its causes and consequences. It explains the percentage contribution of the main greenhouse gases (carbon dioxide, methane and nitrous oxide) to climate change, outlines their origin and the industry sectors which need to take immediate action. It is shown that the electricity and heat production sectors create nearly half of global carbon dioxide emissions. This could be mitigated by increasing the share of renewable electricity production in the global energy supply market. Furthermore, the Introduction gives a brief description of current advancements in all photovoltaic technologies and the history of PSC development.

The Literature Review focuses on perovskite crystal structure and material properties, as well as gives examples of functional layers commonly used in the field. The working principle of a solar cell based on a p-i-n junction is explained. Three different architectures of PSCs are described in detail: planar, back-contact (BC) and QIBC. Current research in BC and QIBC perovskite technologies is discussed. Furthermore, the Literature Review discusses the applications of said technologies in *in situ* measurements of perovskite materials, during film formation and post treatment processes.

The experimental work performed for this Thesis is divided into three Chapters. In the first, QIBC PSCs are measured *in situ* during the photoactive layer film formation. The structural, optoelectronic and photovoltaic measurements allow for determination of a favourable annealing time at a given annealing temperature. Those experiments were performed on methylammonium lead iodide ($MAPbI_3$) – the most common and studied photoactive perovskite; however, methods used in this Chapter can be easily transferred to other types of perovskites and thus, speed up the process of optimising their manufacturing process.

In the second experimental Chapter, QIBC PSCs undergo a post treatment - exposure to vapours of 4-tert-butylpyridine, 2-amyl pyridine and N,N-dimethylformamide. The pilot experiment allowed for the *in situ* observation of the influence of said vapours on the photovoltaic and optoelectronic performance of the devices. The experiment aims to define the favourable vapour dosage and time of interaction between the vapour and the perovskite material to achieve a better perovskite film quality through passivation or recrystallisation effects. Results of this experiment can be directly transferred to other $MAPbI_3$-based photovoltaic devices in order to boost their efficiencies.

The last experimental Chapter focuses on antireflective coatings for BC and QIBC PSCs. The experiments show that the application of a thin poly(methyl methacrylate) (PMMA) layer on top of a QIBC PSCs decreases the reflection from the perovskite/air interface. This significantly increases the photogenerated current and thus, the device efficiency. The PMMA layer simultaneously acts as an encapsulant, improving the durability of the devices by protecting the perovskite from the ambient atmosphere. Additionally, optoelectronic measurements show that PMMA passivates the trap states present at the top surface of QIBC perovskite device, thus, further boosting the photogenerated current.

A summary of all Chapters and future prospects can be found in the Conclusion of this Thesis.

Publications during enrolment

Hou, Q., Bacal, D.M., Jumabekov, A., Li, W., Wang, Z., Lin, X., Ng, S.H., Tan, B., Bao, Q., Chesman, A.S.R., Cheng, Y.B., Bach, U. (2018). Back-contact perovskite solar cells with honeycomb-like charge collecting electrodes. Nano Energy., 50, 710-716.

Jumabekov, A., Lloyd, J., Bacal, D., Bach, U., & Chesman, A. (2018). Fabrication of back-contact electrodes using modified natural lithography. ACS Applied Energy Materials., 1(3), 1077-1082.

Declaration

I hereby declare that this thesis is an original work of my research and contains no material which has been accepted for the award of any other degree or diploma at any university or equivalent institution and that, to the best of my knowledge and belief, this thesis contains no material previously published or written by another person, except where due reference is made in the text of the thesis.

Signature: ……
Print Name: **Dorota Bacal**
Date: ……..

Acknowledgements

I would like to thank my supervisors - Professor Udo Bach (Monash University) and Dr. Doojin Vak (CSIRO) for their support throughout my PhD candidature. I would also like to thank to Dr. Anthony Chesman (CSIRO) for offering his generous help and advice.

I am extremely grateful to all members of Monash Renewable Energy Lab - my colleagues and friends, especially: Dr. Jiangfeng Lu, Dr. Kevin Rietwyk, Dr. Sonia Raga, Dr. Qicheng Hou, Mr. Adam Surmiak, Dr. Xiongfeng Lin, Ms. Samira Aden, Dr. Askhat Jumabekov, Ms. Boer Tan, Dr. Wenxin Mao, Dr. Alexander Pascoe, Dr. Niraj Lal, Dr. Sebastian Fürer, Dr. Kira Rundel and Dr. David McMeekin who supported me during my candidature with their expertise and kind words.

I would like to thank my mentors Mr. John O'Brien and Dr. Rebecca Yee, who showed me the world of renewable energy outside the laboratory and constantly motivated me to discover more.

I acknowledge the Faculty of Engineering International Post-Graduate Research Scholarship (FEIPRS) and Commonwealth Scientific and Industrial Research Organisation (CSIRO) for covering my tuition fee and living expenses. I acknowledge the Australian Centre for Advanced Photovoltaics (ACAP) and the Australian Renewable Energy Agency (ARENA) as the main parties that financially supported my PhD project, as well as the financial support for my research, provided by CSIRO as part of a CSIRO Science Leader position of my supervisor, Professor Udo Bach.

This work was performed in part at the Melbourne Centre for Nanofabrication (MCN) in the Victorian Node of the Australian National Fabrication Facility (ANFF), as well as in Flexible Electronics Laboratory in Commonwealth Scientific and Industrial Research Organisation (CSIRO) and Nanofabrication Laboratory at Swinburne University. I would like to acknowledge scientific and technical support from Dr. Ricky Tjeung and Dr. Yang Lim.

Last but not least, I would like to thank my parents for their unlimited support and my closest friends who helped me to get through the rough moments, especially Dr. Hana Shiraz, Mr. Nicpon Kociuszko, Ms. Joanna Stec, Ms. Barbara Godek, Ms. Roxy Ruchovic, Mr. Toon Goris and Mr. Anton Weissbach.

Table of Contents

In 2100, people will find ludicrous the fact that we inhaled nasty fumes from cars on an everyday basis, the same way we find absurd that in the 1950s, applying radium-based products on the skin was normal. The difference is, we are aware of the consequences. They weren't.

1. Introduction

It is of the highest importance to recognise that the climate change we are currently experiencing is a direct result of human activity. Every day, our actions are shaping the future of the next generations living on this planet. As such, we have the unpleasant honour of deciding what kind of future this will be.

In the light of the recently released Special Report on "Global Warming of 1.5 °C" (SR1.5), by the Intergovernmental Panel on Climate Change (IPCC), there is no time for further questioning of the issue. We need to act now and to do this, we will need breakthrough technologies such as higher efficiency and cheaper photovoltaic solar cells.

1.1 Global warming

The term "global warming" refers to an increase of the mean global surface air and sea surface temperatures, averaged over a period of 30 years. [1] It is usually given in units of degrees Celsius, in relation to pre-industrial levels (years 1850 – 1900) for consistency, although the reference point can sometimes be variable due to the lack of, or limited, data from the aforementioned period. [2]

The current estimates by the IPCC, presented in SR1.5, already show a 1.0 °C increase in the global temperature versus the pre-industrial period, observed from the average of available datasets such as: Surface Temperature Analysis by The Goddard Institute for Space Studies, Global Surface Temperature by National Oceanic & Atmospheric Administration and data collected by the Climatic Research Unit of Hadley Centre, with missing data extrapolated by Hansen *et al.,* [3] Vose *et al.* [4] and Morice *et al.* [5] respectively, and additional corrections provided by Karl *et al.* [6] as well as Cowtan and Way. [7] Furthermore, according to SR1.5 and based on the above datasets, the average global temperature continues to increase at the rate of 0.2 (±0.1) °C per decade.

The increase in global temperature is attributed to the accumulation of so-called greenhouse gasses (GHGs) in the atmosphere, which absorb and re-emit infrared radiation. These GHGs include carbon dioxide, methane, nitrous oxide and fluorinated gases. Human activity and rapid civil development over the last few decades have given rise to an imbalance in natural concentrations of GHGs in the atmosphere. According to the 5th Assessment Report on Climate Change (AR5) by IPCC, [8] in 2010 the total annual anthropogenic emissions of GHGs reached 49 (±4.5) $GtCO_2$ eq/yr (giga tonnes of CO_2 equivalent per year), rising at a rate of 0.4 $GtCO_2$ eq/yr from 1970 to 2000 and at a rate of 1.0 $GtCO_2$ eq/yr from 2000 to 2010. The emissions are continuing to increase at a high rate [9]–[12] despite numerous mitigation

policies implemented on both global and national scales. The devastating consequences of the significant global average increase of 1.0 °C are already observable.

Multiple reports describe a rapid increase of global mean sea level, caused by melting of the polar ice caps. [13]–[17] As a result, islands, lowlands, and coastal areas are experiencing destructive soil erosion and eventually will become infertile. The decline of food security, along with the contamination of groundwater, are predicted to give rise to a wave of climate-change-caused human migration in the near future. [18], [19] Furthermore, the high atmospheric concentrations of carbon dioxide are enhancing hydrolysis in seawater, thus increasing the hydrogen ion concentration and reducing the pH of the ocean. [20], [21] The anthropogenic ocean acidification has a severe impact on marine lives and causes a rapid decline in coral reefs. [22]–[24]

Inland, many animal species and plants are under the danger of climate-change-induced extinction [25]–[28] as a result of habitat loss. [29] The environment and flora change [30] has given rise to animal migration to higher latitudes, estimated to be at a median rate of ~1.7 km/year and to higher elevations at a median rate of 1.1 m/year [30]–[32] which has far-reaching implications on ecosystems and human well-being. [33] For example, the spread of zoonotic and bacterial tropical diseases is already observed around the globe. [34]–[37] Due to global warming, the frequency and strength of extreme weather events is also expected to increase. [38] It is forecast that an intensification of extreme heat waves, heavy precipitation, floods, droughts, fire and extreme winds will be observed in the near furute. [39]

Knowing the devastating consequences of climate change, one should demand an immediate cessation of all anthropogenic emissions of GHGs. Unfortunately, even with instant net zero GHGs emissions, the global temperature will still experience temporary growth for the next few years. [40]–[42]

1.2 Greenhouse gasses in numbers

In the overall rising trend of the total global emissions, the percentage share of the main GHGs remains nearly constant over the last few decades. [43] The three main GHGs and their contribution to the total annual anthropogenic emissions in 2010 are shown on **Figure 1.1**.

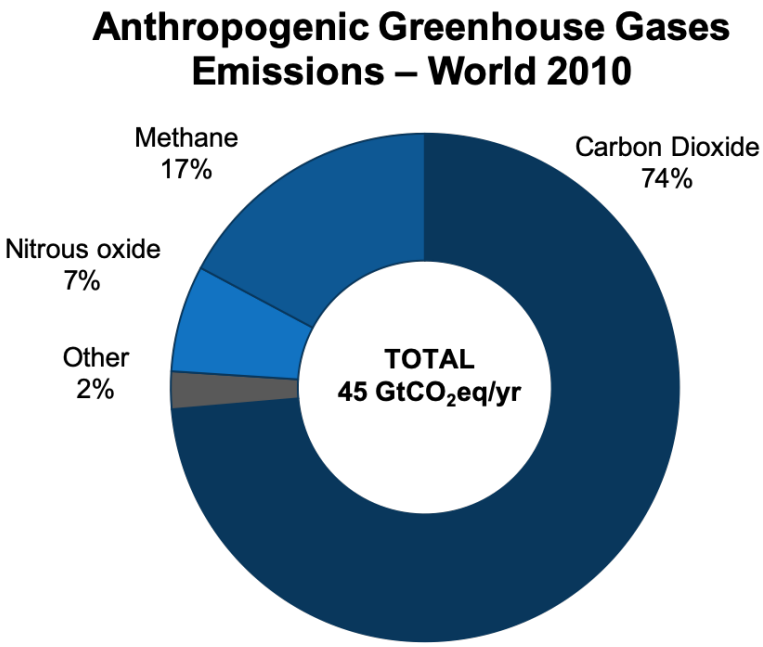

Figure 1.1. Percentage contribution of the main GHGs to the total annual anthropogenic emissions in 2010. Figure based on data from: [43].

The main sources of methane (17% of the total emissions) are agriculture and waste management. Nitrous oxide (7% of the total emissions) is mostly generated in agriculture and fossil fuel combustion. About 74% of the total emissions is credited to carbon dioxide released through combustion of fossil fuels and industrial processes (FFCIP), together with deforestation, land clearing for agriculture and soils degradation (FOLU).

As seen on **Figure 1.2**, the biggest contributor to carbon dioxide FFCIP emissions is the electricity and heat production sector (~50% of FFCIP), followed by transport (~20% of FFCIP) and manufacturing industries and construction (~20% of FFCIP).

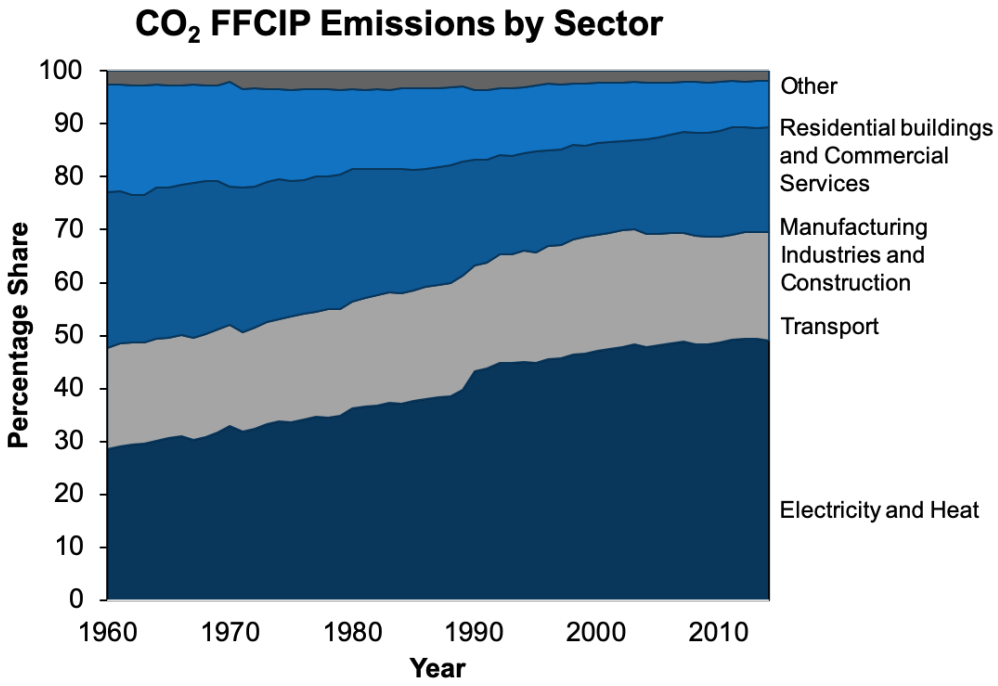

Figure 1.2. Carbon dioxide global emissions by sector. Based on data from: [44] under Creative Commons licence (CC BY-SA 4.0)

Global electricity consumption has increased rapidly over the last few decades at an almost linear rate of 400 billion kilowatt hours per year, [45] with no signs indicating that this trend will slow down in the foreseeable future, due to increases in both number and wealth of the global population. Additionally, with the decreasing price of energy storage solutions, the electrification of the transport sector is expected to become more prominent, [46], [47] shifting even more emissions to the electricity and heat production sector.

The growing need for supplying higher amounts of electricity, along with the consequences of its production, has forced people to search for its alternative sources. This has led to incredible growth in the renewable energy (RE) industry, which is currently responsible for meeting ~25% of the global electricity demand. [45]

1.3 Renewable energy production

Based on data collected by the U.S. Energy Information Administration, almost 70% of total global RE is currently produced by hydroelectric power plants around the world (**Figure 1.3**). [45] The hydroelectricity is generated through a rotation movement of a turbine, powered by a stream of water, thus, through the conversion of kinetic energy into electricity. Unfortunately, the high water current requirements, seasonal weather dependence, and large up-front costs limited the growth of this sector, which is currently experiencing a stagnation. Similarly, wind

turbines (16% of the global RE) require a specific environment of constant, stable wind (e.g. smooth and coastal areas, or mountain passes) and large upfront capital investment.

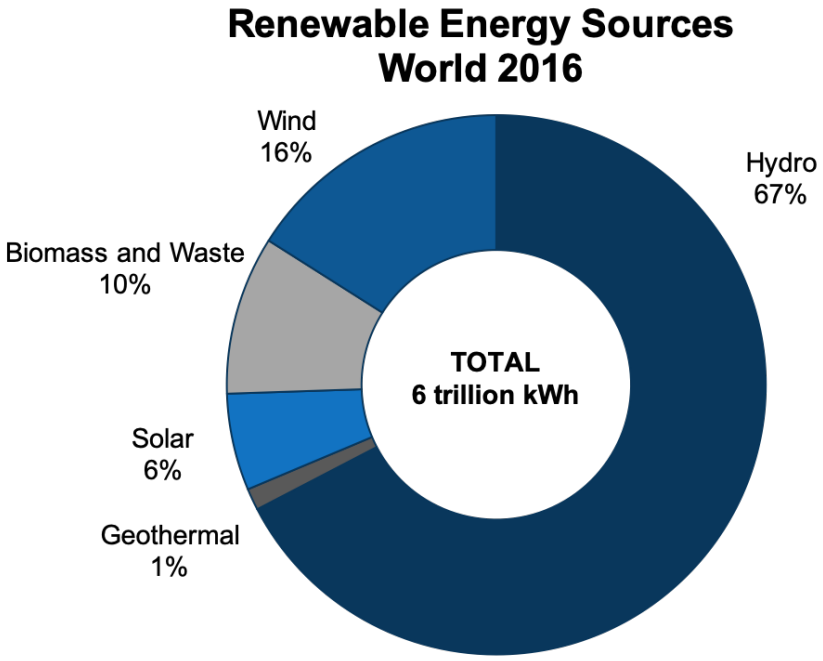

Figure 1.3. Percentage share of electricity production from renewable sources. Based on data from: [45]

Interestingly, solar energy, (currently sharing only ~6% of the global RE generation) is the fastest growing sector of the RE sector, and has grown more than tenfold since 2010. [45] This comes as no surprise, considering the number of distinct advantages of solar energy over the other renewable energy sources.

Unlike hydro and wind plants, solar panels (also known as photovoltaic modules) do not require any specific environment and can be installed anywhere around the globe (compromising on efficiency in areas with lower solar irradiance). Solar technology is easily scalable from small residential systems of a few kilowatts to large solar plants of hundreds of megawatts capacity. For small systems - the solar electricity can be used on the spot, and does not require connection to the grid, which makes it particularly attractive for remote and offshore areas applications.

Solar electricity production does not involve any ongoing GHGs emissions, apart from the ones released during the manufacturing process of photovoltaic (PV) modules. An average energy payback time for commercial polycrystalline silicon solar cells is 3.1 years. [48] Furthermore, a carbon footprint of solar electricity is at the range of tens of grams of CO_2 eq/kWh for different types of solar panels and its geographical location, [49]–[53] which is an

order of magnitude lower than the coal, lignite, oil, and natural gas electricity carbon footprint reported elsewhere. [49], [53]–[58]

Generating electricity from biomass has become a matter of controversy in the RE field. [59] On one hand, the biomass (e.g. trees) captures GHGs during the process of photosynthesis, but on the other hand, the biomass has to then be burned in order to generate heat and electricity. The process of releasing carbon dioxide through biomass burning takes place much faster than capturing it through the growth of plants. It also leads to the creation of local GHG hot spots, and therefore (unlike solar panels) the biomass power plants are usually placed far from urban areas. Furthermore, deforestation causes a loss of habitat for native species and endangers forest biodiversity. Trees are largely contributing to the reduction of GHGs concentrations in the atmosphere through natural carbon sequestration [60] and are currently estimated to store ~30% of annual anthropological carbon emissions. [61]

Finally, a significant advantage of the solar panels is their low maintenance requirement. In solar panels, the electricity is generated by directly converting the sun energy into electrical energy, without employing any moving parts. The typical conservation includes regular rinsing of the panels with water to avoid dirt accumulation, as well as inspecting the electronic components (i.e. cables, connectors, inverter).

1.4 Financial feasibility and return on investment time of silicone solar modules

The aforementioned advantages of PV modules have drawn public attention to small-scale silicon solar panels utilised for residential purposes, as well as of big investors financing large-scale solar farms. This has significantly accelerated the development of the manufacturing industry of PV modules and impacted the price of solar panels. Over the last few decades, together with an increasing installed capacity of PV modules, the average price of solar modules has dropped more than ten-fold, to the price of ~0.60 $/Wp (American dollars per watt peak) and it is currently still slightly decreasing (**Figure 1.4**). [62]

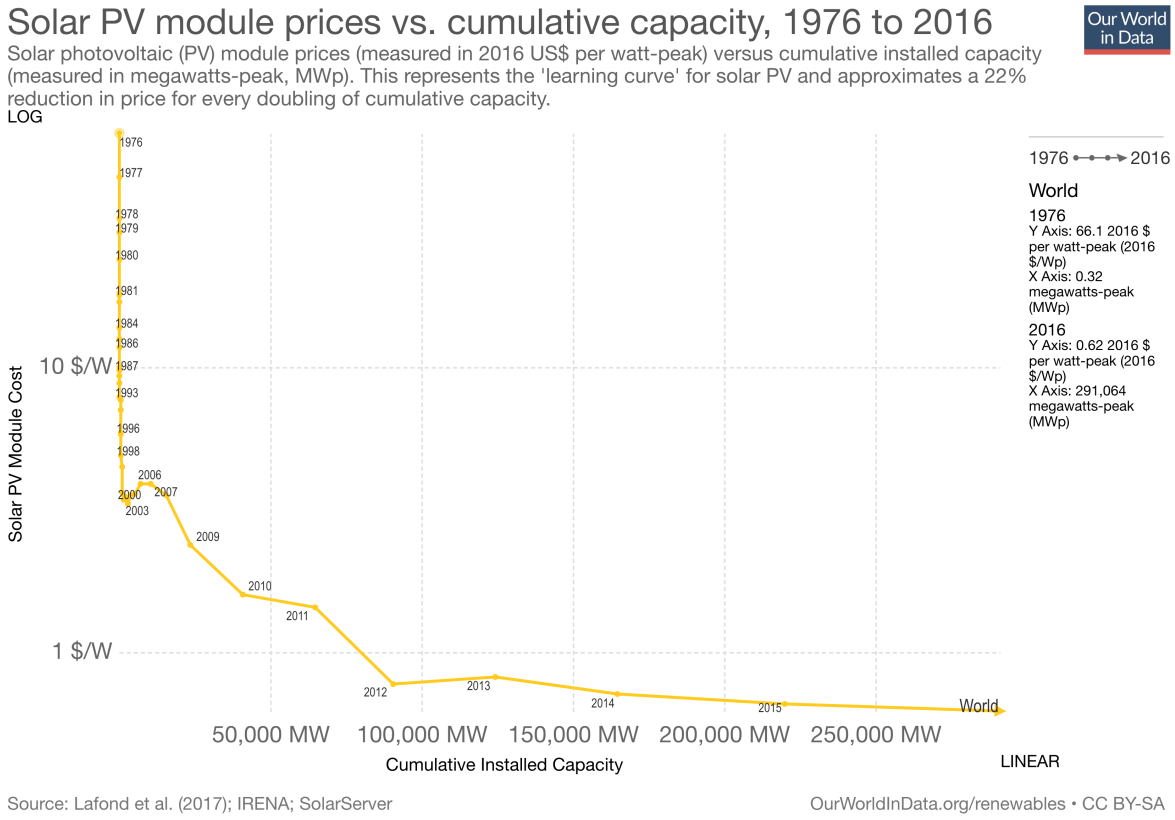

Figure 1.4. Price of PV modules per watt peak over time and cumulative installed capacity. Y scale logarithmic. Reprinted from: [62] under Creative Commons licence (CC BY-SA 4.0)

As seen in **Figure 1.4**, the global average price of silicon PV modules decreased rapidly between 1976 and 2000. This was mainly caused by the growth of manufacturing infrastructure and development of solar-grade silicon treatment processes. [63] The price has continued to decrease further during the last few years, due to the economies of scale. Despite that, solar panels are still relatively expensive and there is no indication that this price will decrease significantly in the near future. Additionally, the payback period of silicon PV modules differs notably according to the geographical location. Even with financial support of government rebates in highly developed countries, the payback period varies between a few to over a dozen years, very rarely dropping below 5 years. The possible ways of enhancing the financial feasibility of PV modules include a decrease in the price of current technology, an increase in the power conversion efficiency (PCE) of PV modules or a transition to a new, cheaper and/or more efficient technology.

The governmental financial support for installing PV modules is likely to continue worldwide in the near future, considering the international commitments of the reduction of GHGs emissions, declared by the majority of countries in the world. The first global initiative on the mitigation of climate change was adopted in 1992 (New York) and enforced in 1994. The United Nations Framework Convention on Climate Change (UNFCCC), whose main

objective is the "*stabilization of greenhouse gas concentrations in the atmosphere at a level that would prevent dangerous anthropogenic interference with the climate system*" [64] was signed by 195 and ratified by 187 Parties to UNFCCC, as of 20th of November 2019. [65] This document is the first official international expression of a globally shared will to reduce the anthropological GHGs emissions.

Although only qualitative, the Framework gave a basis for creating the Kyoto Protocol [66] in 1997, during the Third Conference of Parties (COP) as well as the Paris Agreement (PA), adopted in 2015, during the twenty-first COP. These two documents describe the process for Parties to declare their nationally determined contributions (NDCs) to the reduction of global emissions and set a timeline for achieving it. The Parties of UNFCCC committed to "*Holding the increase in the global average temperature to well below 2°C above pre-industrial levels and pursuing efforts to limit the temperature increase to 1.5°C above pre-industrial levels, recognizing that this would significantly reduce the risks and impacts of climate change*" (Art 2 of PA). However, the Paris Agreement does not impose any penalties on the Parties not meeting their NDCs, making their contribution to climate crisis mitigation entirely voluntarily. Despite this, the significant investment in the renewable energy sector is expected to continue to increase globally over the next few decades.

Another way of decreasing the payback period of silicon solar panels is an increase in its PCE, assuming a fixed price: a larger production of electricity means more savings on the electricity bill and eventually, a faster repayment of the initial investment. **Figure 1.5** shows the progression of PCE of different types of solar cells over time. [67] The champion silicon solar cells (in blue) are currently able to convert 26.6% [68] of the incident light into electricity and 27.6% [69] with the addition of a light concentrator.

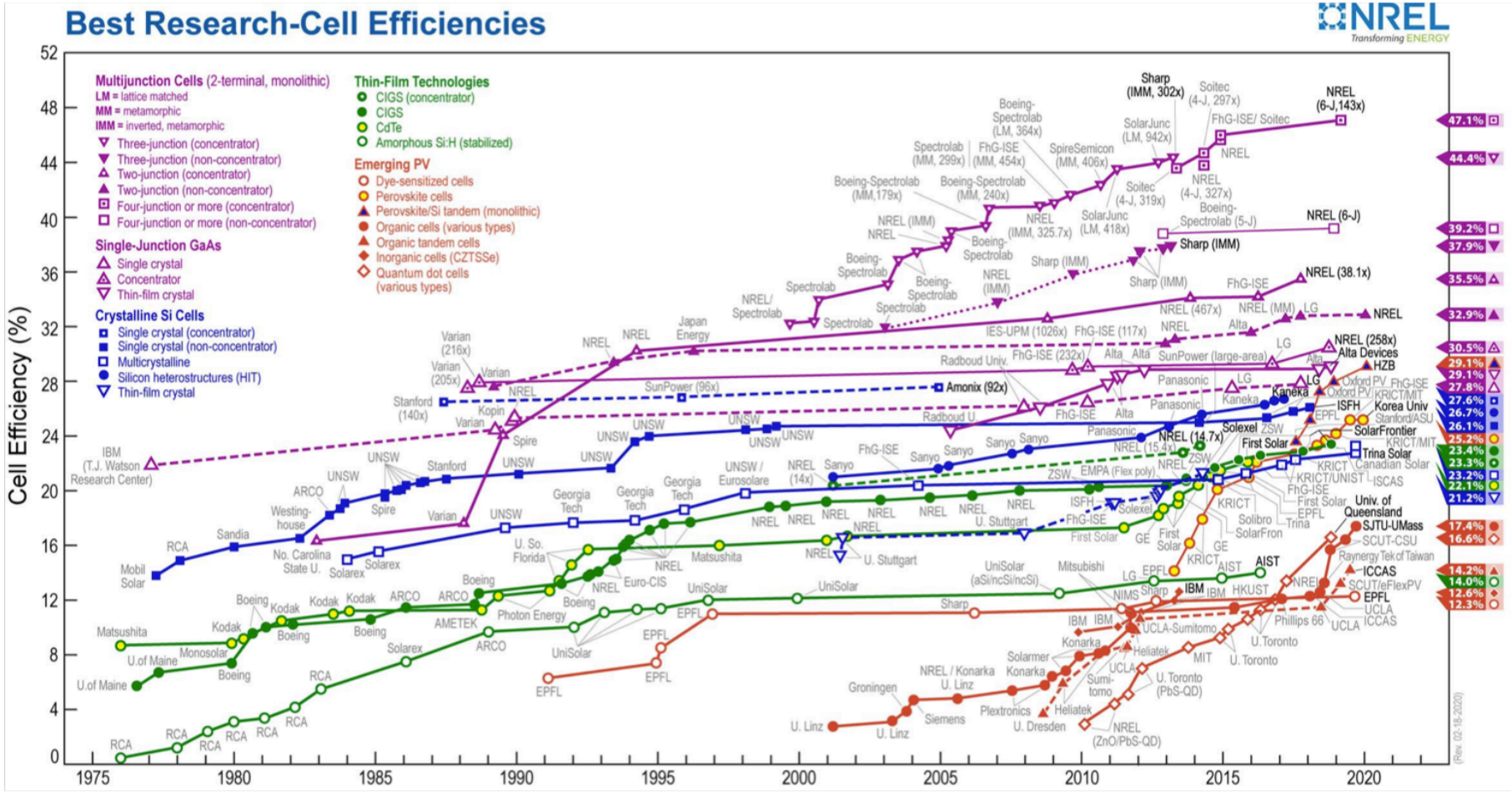

Figure 1.5. The best performing solar cells by category over time. This plot is courtesy of the National Renewable Energy Laboratory, Golden, CO. [84]

As seen in **Figure 1.5**, the increase in PCE of silicon solar cells is rather slow over the last few decades. This comes as no surprise, considering the fact that the silicon processing technology was adopted from the electronics industry and it is mature. Furthermore, the champion silicon solar cells are nearly approaching their Shockley-Queisser limit [70] of 32.23%, which represents the maximum PCE that can be achieved by an ideal single junction solar cell with a semiconductor band gap energy of 1.1 V. [71]

1.5 Multijunction solar cells, thin film solar cells and emerging solar technologies

Multijunction solar cells (**Figure 1.5**, in purple) exceed significantly the PCE of silicon solar cells. The current world record is held by a four junction solar cell comprised of active layers of GaInP/GaAs//GaInAsP/GaInAs, converting 46% of the incident light into the electricity, under a concentrated illumination of 508 suns. [72] Moreover, the theoretical Shockley-Queisser limit calculated for a multijunction solar cell with an infinite number of layers is 68.2% for 1 sun illumination intensity and 86.8 % for 45 900 suns intensity (assumed to be the highest physically possible), indicating there is still significant potential to improve today's technology. [73] Unfortunately, due to the complex structure of multi-junction solar cells, their manufacturing process is rather complicated and expensive. Therefore, regardless of their performance, the applications of multijunction solar cells are, so far, mainly limited to high-tech space missions, the military and wherever the sun-exposed surface area is relatively small, but the energy demand is high.

Inorganic thin film technologies (**Figure 1.5**, in green) demonstrate PCEs comparable with silicon solar cells. Their exceptionally high absorption coefficient [74] allows for saving on the raw feedstock material (which unfortunately consists of rare and toxic elements), without compromising on the efficiency. The champion copper indium gallium selenide (CIGS) solar cell has a PCE of 23.3% [75] and 22.9% [76] with and without a concentrator (15 suns), respectively, followed by cadmium telluride solar cells (champion 22.1% [67]). Thin film inorganic solar cells are currently available on the market, despite the initial problems with their scalability. [77], [78] However, the complexity of manufacturing and the toxicity and rareness of the feedstock materials has limited the competitiveness of these solar cells. The commercial world demands cheaper solar energy with additional features, such as flexibility, lightness in weight, aesthetic values and semitransparency. New technologies are emerging in the PV world that have the potential to combine all of those attributes (**Figure 1.5**, in red).

Dye-sensitized solar cells (DSSCs) have the highest seniority amongst all emerging, or next-generation, technologies. Thanks to a variety of dyes with different bandgaps, DSSCs are available in a wide range of colours. Furthermore, DSSCs absorb low intensity light

efficiently, allowing for the absorption of diffused ambient light as well as an artificial light, [79] and are based on nontoxic and inexpensive materials. Because of this, they are particularly interesting for indoor applications. Unfortunately, the relatively low PCE (11.9% champion [67]) and stagnation in efficiency improvements over the past few years limits the commercialisation of DSSCs.

A few years ago, organic solar cells and quantum dot-based solar cells exceeded the PCE record of DSSCs, reaching 15.6% and 16.6% respectively. [67] However, their success has been overshadowed by the biggest breakthrough in the PV world of last few decades – the discovery of perovskite photoactive material.

1.5.1 The rise of perovskite solar cells

The slow progress in emerging solar technologies was dramatically disrupted in 2009, when Kojima *et al*. reported an efficiency of 3.81% using nanoparticles of $CH_3NH_3PbI_3$ as a replacement of a dye in DSSCs. [80] This technology was termed "perovskite" and the rapid increase in PCE of perovskite solar cells (PSCs) over the next few years quickly caught the attention of the scientific world [81] (**Figure 1.5**, in red). In 2013, both Science and Nature announced PSCs as one of the top ten breakthroughs of the year. [82], [83] This contributed to an almost exponential growth in the number of scientific papers and citations in the field, followed by the enormous rise in perovskite solar cells' efficiency (**Figure 1.6**). Today the most efficient PSC converts >25% [84] of the incident light into electricity in the planar structure and 28% [85] when combined with a silicon solar cell in a tandem configuration.

A small number of companies around the world have committed to commercialising PSCs in the near future, with the current leader, Microquanta, producing perovskite minimodules with certified PCE of 17.9%. [86] Nevertheless, there is still an urgent need for further development of the technology. In particular, the long-term stability (lifetime) of perovskite solar cells is an issue. Also, some of the intrinsic mechanisms of the perovskite material are yet to be fully understood (e.g. the origin of the hysteresis.) Additionally, the interface engineering, as well as surface trap states passivation, seem to play a big role in PSC performance, and need to be addressed. It is also essential to develop and optimise scalable methods of perovskite deposition. Furthermore, the efficiency of PSCs can be further enhanced by considering different device architectures e.g. the back-contact (BC) configuration deployed in the most efficient silicon solar cells.

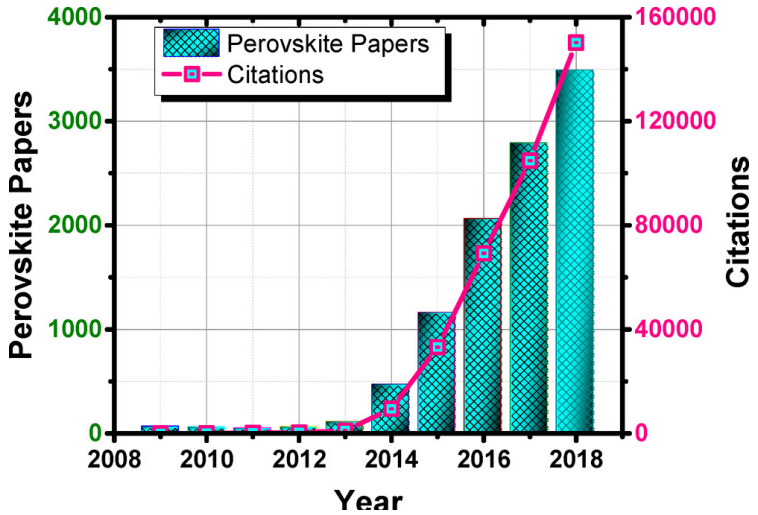

Figure 1.6. Number of scientific papers and number of citations in the field of perovskite solar cells in years 2009 – 2018. (Source: Web of Science, Clarivate Analytics March 3, 2019). Reprinted with permission from: [87]. Copyright 2019 American Chemical Society.

2. Literature Review

2.1 Perovskite material properties

The term 'perovskite' refers to the family of materials exhibiting a crystal structure ABX_3. The structure was first observed in 1839 by Gustav Rose in calcium titanium oxide, and later characterised by the Russian mineralogist, Lev Alekseyevich von Perovski, from whom it inherited its name. In the perovskite crystal, a larger A cation occupies a corner of a cubic structure (0,0,0) with a smaller B cation at the body centred position (½,½,½), surrounded by octahedral of X anions (½,½,0) (**Figure 2.1**).

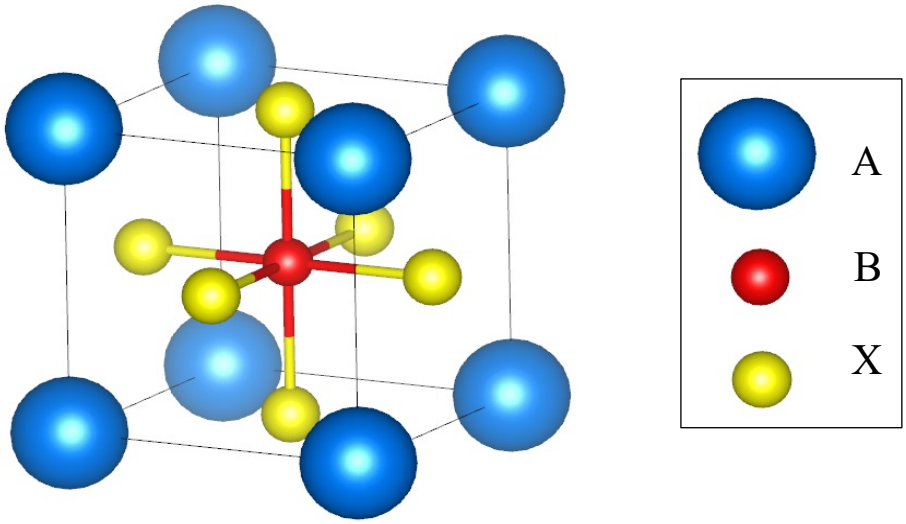

Figure 2.1. Perovskite crystal structure ABX_3. A and B represent cations. C represents an anion.

In order to create a stable perovskite crystal, it is critical to consider the Goldschmith tolerance factor and the octahedral factor. [88], [89] The Goldschmidt tolerance factor is defined as a ratio of distances A – X and B – X in an idealised solid-sphere model. The octahedral factor, proposed by Le *et al.,* [90] compliments the tolerance factor and is defined as a ratio of radii of the cation *B* over the radii of anion *X*:

$$t = \frac{R_A + R_B}{\sqrt{2}(R_B + R_X)} \qquad \mu = \frac{R_B}{R_X}$$

where R_A and R_B are the ionic radii of the corresponding cations and R_X is the ionic radius of an anion.

The tolerance and the octahedral factors differ for different types of perovskite, depending on the crystal component selections. This influences the shape of the unit cell. [91] A cubic structure, corresponding to the P*m3m* space group (**Figure 2.1**) is most likely for t = 0.89 – 1.0, whereas tetragonal or orthorhombic structures appear for lower t and hexagonal structures for higher t. [92], [93] For perovskite halides the octahedral factor lies between 0.442 and 0.895. [93]

The tolerance and the octahedral factors provide a guideline for perovskite formability, although the aforementioned values are describing a necessary, but not sufficient condition, in order to achieve the desired symmetry. Other circumstances, such as heat, crystal boundaries and defects, as well as oxidative/reductive environments, can affect the crystal structure of the perovskite material.

Temperature has a huge impact on the structural properties of the perovskite material. As an example, the unit cells of methylammonium lead iodide ($MAPbI_3$) (the most studied out of all perovskite materials) undergoes phase transitions from tetragonal structure (existing at room temperature) to cubic (above ~54 °C) or to orthorhombic structures (below ~ -111 °C). [94] This is caused by a rotation of the MA^+ cation inside of the perovskite unit cell around its C–N axis, with a faster movement observed for higher temperatures. [95] Furthermore, first-principles calculations performed by Geng *et al.* show that the MA^+ molecule changes its C–N axis orientation at different temperatures, which has an influence on the Pb–I bond length an Pb–I–Pb angle and thus the stability and electronic properties of the material. [96] These structural changes appear for all perovskite materials at very distinct, unique temperatures.

The most widely used *A* cations in PSCs are: methylammonium $CH_3NH_3^+$ (MA^+) with R = 1.8 Å, [97] formamidinium $CH(NH_2)_2^+$ (FA^+) with R = 1.9−2.2 Å [98] and caesium (Cs^+) with R = 1.65 Å [99] or a mixture of these three. Cation *B* represents a metal cation, usually lead (Pb^{2+}), although many efforts are being made to replace it with tin (Sn^{2+}) due to toxicity reasons [100] (R = 1.19 Å and R = 1.1 Å, respectively). Anion *X* is usually a mixed halide material made of iodine (I^-) with R = 2.20 Å and bromine (Br^-) with R = 1.96 Å or chlorine (Cl^-) with R = 1.81 Å. [99]

Mixing between the aforementioned components not only influences the shape of the perovskite crystal, but also affects the electronic properties of the material. Changing the B–X bond length and B–X–B bond angle allows for tuning of the bandgap of these perovskites between 1.1 and 2.3 eV, [100]–[103] with smaller bandgap appearing for larger octahedrons and larger bond angles. [104] It was shown that increasing the electronegativity of component X leads to an increase in valence character of the B–X bond, leading to a wider bandgap. [105], [106] As observed in numerous studies, the choice of cation A, also has an impact on the

perovskite bandgap, with bigger molecules decreasing the bandgap size and thus red shifting the absorption spectra. [107], [108] Although, the first principle modelling performed by Amat *et al.* on group of $APbI_3$ materials shows that the interaction of cation A with other atoms in the crystal lattice through H−I hydrogen bonds plays an equally important role in shaping the energy bands of the material. [109]

The adjustable absorption spectrum, together with a sharp absorption edge, [110] are some of the biggest advantages of perovskite PV materials. Thanks to those properties, perovskites have found application in tandem solar cells (SCs), either as perovskite-perovskite tandem SCs [111] or with silicon SCs, further increasing their efficiency. [112], [113] Moreover, the bandgap tunning affects the aesthetics of the perovskite solar cells. As presented in numerous studies, changing the ratio of different cations and anions in perovskite materials allows for a deposition of films in almost every colour of the visible spectrum. [98], [108], [114] An example of bandgap tuning caused by the composition change can be observed on **Figure 2.2** on an energy diagram (a) and as a matrix of different colours of solar cells made of different compositions of perovskites (b).

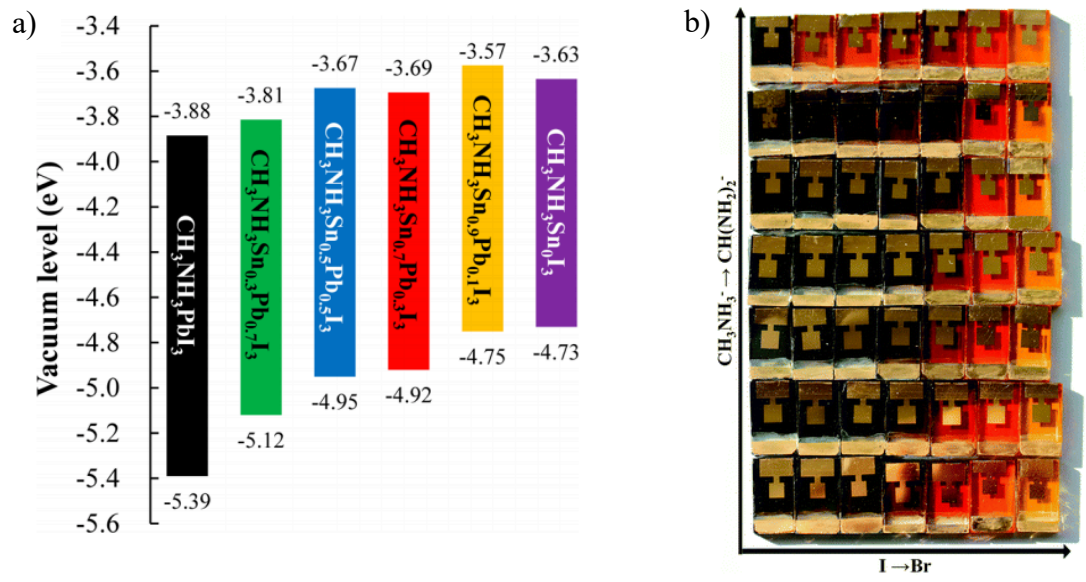

Figure 2.2. Change of the bandgap of perovskite material caused by the change in its composition. (a) Tuning of the band gap from 1.51 eV to 1.10 eV by increasing the tin concentration. Reprinted from: [115] with permission of the American Chemical Society. (b) A matrix of different rations of cations MA^+ and FA^+ mixed with different ratios of I^- and Br^- in $APbX_3$ perovskites. Change of the bandgap is represented by the colour of the perovskite material. Reprinted from: [108] with permission of The Royal Society of Chemistry.

The unique combination of excellent optical and electronic properties, distinguish perovskite from the crowd of emerging PV technologies. Due to its low crystallisation energy

barrier (56.6 – 97.3 kJ mol^{-1} [116] compared to 280 – 470 kJ mol^{-1} for amorphous silicon, [117]) perovskite can be deposited via numerous low-temperature processes from solution, which makes it particularly appealing for large-scale industry production. [118], [119] Furthermore, a space-charge-limited current study performed by Huang *et al.* estimated the trap-state density of crystalline perovskite: ~10^9 – 10^{10} cm^{-3}. [120] This value is significantly lower than in case of other thin film technologies (polycrystalline Si: ~10^{13} – 10^{14} cm^{-3}, CdTe/CdS: ~10^{11} – 10^{13} cm^{-3}, CIGS: ~10^{13} cm^{-3}) [88], [121], [122] and comparable to the best intrinsic silicon and GaAs results. In an ideal case, charges would travel within one perovskite crystal until they reach the electrode, but there is no method for depositing single crystals in a sandwich architecture. However, in planar perovskite SC charge transport takes place in vertical direction and due to the submicrometric thickness of the planar structure, charges travel inside of one crystal most of the time. Nevertheless, the trap state density calculated in the same study by Huang *et al.* for polycrystalline perovskite is ~10^{15} – 10^{17} cm^{-3}, which is still comparable with other existing technologies.

Perovskites show very low exciton binding energies (in range of tens of meV [123]–[126]), which means that the process of creating free charge carriers in the material is relatively easy. In contrast, this process is one of the main causes of decreasing the open circuit voltage in organic solar cells, where the binding energy can reach 1eV. [127] Furthermore, relatively long carrier diffusion lengths in perovskite materials reduce the probability of charge recombination, thus increasing the number of extracted charges and hence, the photocurrent. The typical values reported in the literature for perovskite polycrystalline films ranges from few hundred nanometres up to 1 μm, [121], [128], [129] however, Dong *et al.* were able to achieve diffusion lengths greater than 175 μm in perovskite single crystals. [122]

All of the advantages of perovskite materials have sparked interest in commercialising PSCs and contribute to the rapid development of this technology.

2.2 Working principle of perovskite solar cells.

The role of the perovskite layer in the device is to absorb the incident light and convert it into free charge carriers (electrons and holes). Subsequently, the charges need to be extracted from the perovskite and transported to the electrodes. The carriers' extraction occurs thanks to an internal electric field, occurring inside of the perovskite material. This field is induced by adding two charge selective layers and creating an n-i-p junction (regular SCs) or p-i-n junction (inverted SCs). This gives a driving force for electrons and holes to move in opposite directions, towards their corresponding electrodes. The average carrier lifetime in perovskite material is

in the order of hundreds of nanoseconds, [129]–[131] hence, to avoid the recombination, the process of charge carrier extraction has to be much faster.

2.2.1 Energy diagram

The working principle of perovskite solar cells can be explained by an energy diagram, presented on **Figure 2.3** The incident photon is absorbed by the perovskite photoactive material (1). The energy of the photon is used to excite an electron from the valence to the conductive band. The electron leaves behind a hole (2). The bandgap of the perovskite material determines the lowest energy of the photons that can be absorbed, with $CH_3NH_3PbI_3$ requiring a minimum of ~ 1.50 – 1.55 eV. [132] The excited electron travels in the direction of the electron selective layer (ESL), towards a lower energy state and eventually reaches the cathode. Simultaneously, the hole travels in direction of the hole selective later (HSL), towards a higher energy state and eventually reaches the anode (3). The energy difference between the conductive band of the perovskite material and LUMO of the ESL creates a driving force for the electrons' extraction. Similarly, the energy difference between the valence band of the perovskite material and HOMO of the HSL creates a driving force for the holes' extraction. Furthermore, the difference of HOMO level of the HSL and the LUMO level of the ESL determines the maximum open circuit voltage that can be obtained by the device.

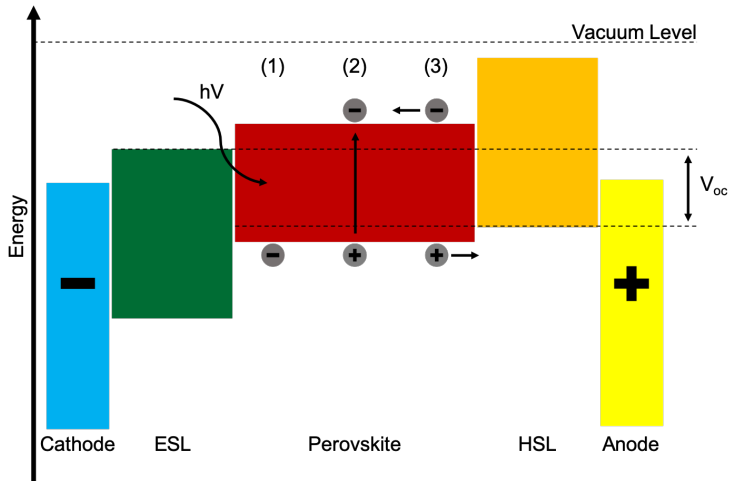

Figure 2.3. Energy diagram of a perovskite solar cell, showing the working principle of the device: free charges created in perovskite layer are extracted by corresponding charge selective layers and travel towards the electrodes.

The choice of ESL and HSL materials strongly depends on their band gap alignment with a chosen type of perovskite. The charge selective layers also need to be characterised by a good charge mobility and low traps density to avoid charge recombination. Furthermore, in conventional planar PSCs at least one of the charge selective layers must be highly transparent

in the wavelength range of perovskite absorption, in order to allow photons to reach the perovskite material. Additionally, the deposition process of the charge selective layers must not harm the underlaying films. All of these requirements, together with a long term and good temperature stability, significantly limit the range of available charge selective layer options.

Until now, the properties of numerous organic and inorganic materials were studied for charge selective layers applications. All of them find their use in different device architectures and in conjunction with different types of perovskite material. **Figure 2.4** shows the energy diagram of the most frequently used charge selective layers, together with representative perovskites and work functions of commonly used electrodes.

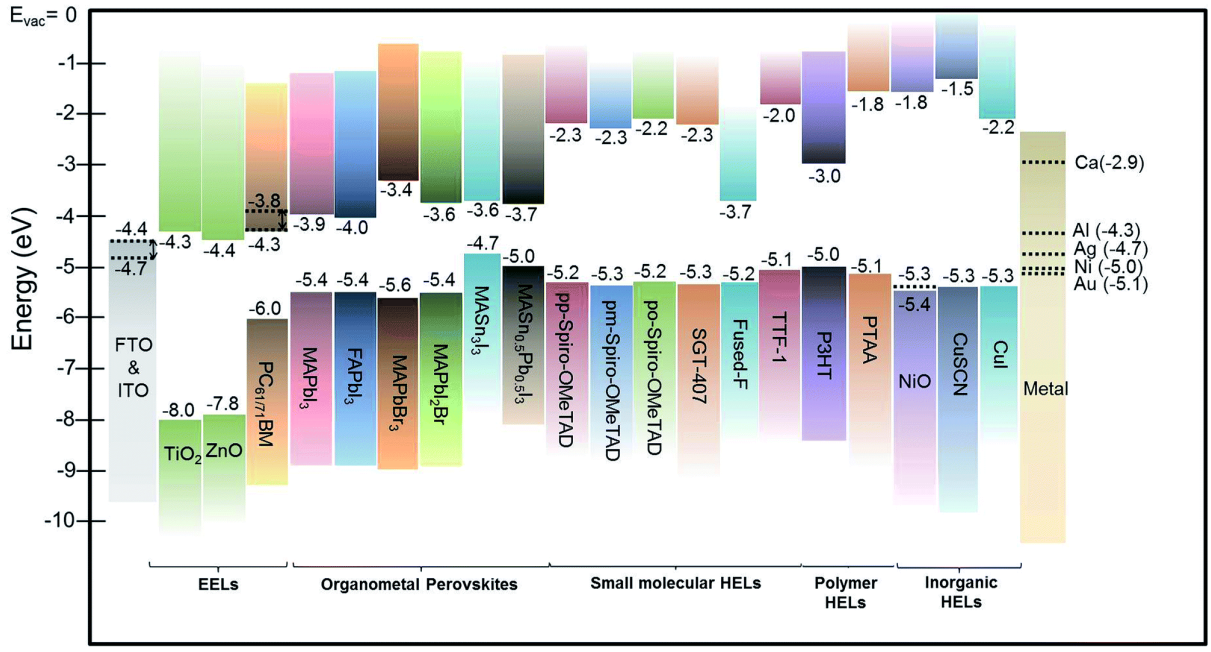

Figure 2.4. Energy diagram of representative perovskites, charge selective materials and electrodes (dotted lines represent the work function). Reprinted from: [133] with permission of The Royal Society of Chemistry.

2.2.2 Electron selective layers

As mentioned above, the role of the ESL is to extract electrons from the perovskite material and transport them to the cathode. Simultaneously, the ESL works as a buffer layer for holes, blocking their pathway towards the cathode, thus suppressing recombination.

One of the most commonly used ESL in PSCs is TiO_2. This is due to its good band alignment with most of the photoactive perovskite materials, high transparency and a sufficiently long electron lifetime. [134] The most efficient perovskite solar cells usually contain a mix of compact and mesoporous titania layers. This combination allows for a pinhole-free buffer, stopping holes from recombining with the cathode, and simultaneously, a

maximised contact surface area penetrating the perovskite layer to enhance the electron extraction. A mesoporous layer of TiO_2 can be deposited via screen printing – a process well developed for DSSCs. [135] A compact layer of TiO_2 is usually deposited via spray pyrolysis, due to a good and repeatable layer quality, as well as the ease of this process. [136] Both of those deposition methods require an annealing step at a high temperature, up to 500°C, which, unfortunately exceeds the melting point of most flexible substrates, thus limiting the device applications. The use of low temperature titania deposition methods (e.g. atomic layer deposition ALD from titanium isopropoxide and water, [137] or UV-assisted spin-coating [138]) usually requires a compromise on the layer quality and thus the device efficiency. Furthermore, as in the case of ALD, it significantly increases the time for device preparation and requires a high vacuum.

Other inorganic electron selective materials, such as ZnO and SnO_2, have slowly begun to gain popularity thanks to their low temperature deposition processes (e.g. DC sputtering, [139] printing, [140] spin-coating [141]) and favourable bandgaps. In comparison with titania, ZnO is characterised by a much higher electron mobility. [142], [143] However, studies show that ZnO encourages the thermal degradation of the solar cell. [144]–[146] Devices employing SnO_2 very often suffer from severe hysteresis. [147] To date, the highest efficiencies obtained with SnO_2 and ZnO are ~21% [148] and ~16% [149], [150] respectively.

The most popular organic ESL used in an inverted structure is [6,6]-phenyl C61 butyric acid methyl ester (PCBM), with its low temperature, solution deposition process and the efficiencies exceeding 20%. [151] However, this ESL is known for a high nonradiative recombination caused by uncompleted coverage of the underlying perovskite layer. [152] To mitigate this issue, the layer of PCBM can be backed up by a thermally evaporated lithium fluoride and C_{60}/bathocuproine, [153], [154] adding not only cost but also complicating the device fabrication process.

2.2.3 Hole selective layers

HSLs extract the holes from the perovskite material and transport them to the anode, and simultaneously stop electrons from going this direction.

The most common HSL used in PSCs is 2,2',7,7'-tetrakis-(N,N-di-p- methoxyphenyl-amine)9,9'- spirobifluorene (Spiro-OMeTAD), first applied as a HSL in solid state DSSCs. [155] Currently, different variations of Spiro-OMeTAD are synthesized by changing the positions of the two methoxy substituents to improve its electronic properties. [156] The standard method of depositing Spiro-OMeTAD usually includes spin-coating from a chlorobenzene solution with small additives of 4-tert-butyl pyridine (TBP) and lithium-

bis(trifluoromethanesulfonyl)imide (Li-TFSI). The additives enhance the conductivity of Spiro-OMeTAD, however, studies show that Li-TFSI is hygroscopic and harmful to the long term stability of PSCs. [157], [158]

Organic polymer materials are widely used as HSLs in PSCs. Polytriarylamine (PTAA) was applied as a hole selective layer of a previous champion perovskite cell. [159] The layer is usually spin-coated on top of perovskite in toluene solution with an additive of Li-TFSI and TBP. Another polymer, poly(3,4-ethylenedioxythiophene)-poly(styrenesulfonate) (PEDOT:PSS), is widely used in an inverted structure. It can be deposited, among other methods, by spin-coating [160] or printing [140] on a glass or plastic substrate covered with a transparent conductive oxide. PEDOT:PSS and its derivatives are particularly interesting for large scale flexible PSCs. This is due to its low temperature and scalable deposition methods, as well as a good resistance to cracking. [161], [162] Additionally, Snaith *et al*. developed a method of depositing a layer of PEDOT:PSS directly on top of perovskite material, creating a regular (non-inverted) PSC. [163]

A wide range of inorganic materials have been studied for application as an HSL. These are particularly interesting for BC PSC, because of its well-developed selective deposition methods. This means that the HSL can be deposited selectively on top of one of the electrodes, even though both BC electrodes are already present on the substrate. As an example, CuSCN can be electrodeposited following the method developed by Chappaz-Gillot *et al*. [164], [165] on top of an electrode that is negatively charged versus a reference electrode. Furthermore, metal oxides, such as NiO and Cu_2O, can be obtained through the thermal oxidation of a prepatterned metal electrode resulting in a similar effect. [166], [167] Other widely used and scalable methods of deposition of inorganic HSLs include doctor blading, [168] [169] spray coating, [170] sputtering [171] and spin-coating. [160], [172], [173] The inorganic HSLs are characterised by a high chemical stability, high hole mobility and low cost. Unfortunately, none of the inorganic HSL have led to the efficiencies obtained with their organic equivalents.

2.2.4 Electrodes

The role of electrodes in PSC is to collect the charges from charge selective layers and transport it to the grid. The planar architecture of PSCs requires at least one of the electrodes to be transparent in order to allow the photons to reach the perovskite material. Therefore, wide bandgap transparent conductive oxides (TCO), such as indium tin oxide (ITO) and fluorine doped tin oxide (FTO), are widely used in the PSC field. Various types and patterns of TCO coated glass and plastic substrates are commercially available.

The back (not necessarily transparent) electrode is usually made of gold, silver, aluminium, nickel or copper. These electrodes are usually deposited via physical vapour deposition methods. The best results in efficiency and perovskite device stability are obtained with gold; the other materials are used whenever the cost of the device plays a significant role. [174]

2.3 Architectures of perovskite solar cells

Originally, perovskite solar cells are manufactured in a planar configuration (**Figure 2.5a**). This architecture consists of a perovskite layer sandwiched in between two of the charge selective layers and complemented by the positive and negative electrodes. The layers can create a n-i-p (regular) or p-i-n (inverted) junctions. Additionally, one of the charge selective layers can be enriched with an additional, mesoporous layer.

Multiple benefits discussed below are arising from the adaptation of an interdigitated (IBC) and quasi-interdigitated back-contact (QIBC) architecture of the device (**Figures 2.5b** and **Figure 2.5c** respectively). In those configurations, both of the electrodes rest at the bottom of the device, however, the n-i-p junction charge transport rules remain unchanged.

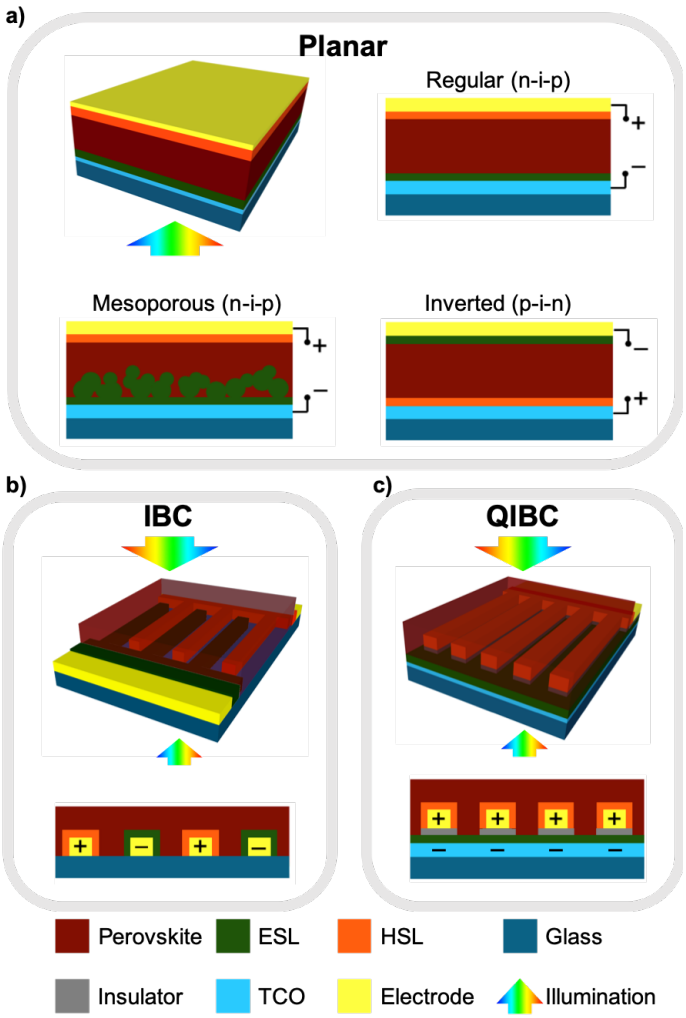

Figure 2.5. Different architectures of PSCs. (a) 3D drawing of regular planar perovskite solar cell and its cross-section as well as cross-sections of planar regular mesoporous and an inverted planar structure. (b) 3D drawing of interdigitated back-contact (IBC) perovskite solar cell and its cross-section. (c) 3D drawing of quasi-interdigitated back-contact (QIBC) perovskite solar cell and its cross-section.

2.3.1 Planar perovskite solar cells

The planar architecture of PSCs evolved from DSSCs, where perovskite was initially used as a replacement for a dye. The structure reported in 2009 by Miyasaka *et al.* [80] consisted of $CH_3NH_3PbI_3$ nanoparticles deposited on a mesoporous layer of titania (ESL), resting on compact titania/FTO coated glass (anode) and an organic electrolyte solution containing lithium halide and halogen (HSL), sealed with a Pt-coated FTO glass (cathode).

Overtime, the outstanding photovoltaic properties of perovskite became more prominent, as Snaith *et al.* [175] reported the enhanced charge extraction of perovskite-sensitized SC. In the same work, they replaced the mesoporous titania layer with insulating alumina and measured a device efficiency exceeding 10%. This indicated the redundancy of

the mesoporous layer of titania and gave rise to the current form of the planar perovskite solar cells.

The main advantage of the planar structure is a simple arrangement and ease of fabrication; however, many research groups still complement the device with the addition of a thin layer of a scaffold material (such as TiO_2, Al_2O_3 or ZrO_2) to increase the contact area between the perovskite and ESL and suppress the charge recombination at the interface. [176] As seen of **Figure 2.5a**, in the planar architecture perovskite material is sandwiched between the ESL and HSL. The charge transport takes place in the direction perpendicular to the device plane. The solar cell is illuminated from the bottom (glass) side, therefore the bottom electrode and one of the charge selective layers must be transparent. Thanks to the relatively high absorption coefficient, reaching values even few orders of magnitude higher than for crystalline silicon, [110], [114] PSC belong to the group of thin film solar cells. According to the study performed by Im *et al*. on a TiO_2 film coated with $CH_3NH_3PbI_3$ nanodots, its absorption coefficient at 550 nm is around 1.5×10^4 cm^{-1}, [177] giving a maximum penetration depth of this light ~660 nm. [178] Hence, the typical thickness of the perovskite layer applied in the planar configuration SC is on order of few hundred nanometres, comparing to a submillimetre thick silicon used in silicon solar cells. Similar perovskite thickness values were obtained by Minemoto *et al.* through the modelling of the ideal perovskite device. [179] Nevertheless, efficiencies above 5% were still obtained with perovskite thicknesses as low as 55 nm in order to produce semitransparent PSC. [180] Furthermore, a slight decrease in the efficiency of perovskite devices is observed for a thicknesses greater than 0.5 μm, caused by a reduction of the electric field inside of the photoactive layer. [179]

Planar PSCs suffer from transmission losses (parasitic light absorption), caused by the bottom electrode and one of the charge selective layers. Similarly, in silicon solar cells, the top electrode (having a form of silver stripes) is shading the surface of the solar cell. This gave rise to the development of back-contact electrodes for solar cells, which are the main focus of this Thesis.

2.3.2 Interdigitated back-contact perovskite solar cells

The IBC architecture for silicon solar cells was first proposed in 1975 by R. J. Schwartz. [181] Thanks to the low series resistance of the electrodes (determined by their thickness), this new architecture was particularly interesting for application in concentrator solar cells. As soon as 1985, IBC silicon solar cells reached an efficiency exceeding 20%. [182] A few years later, Honda demonstrated the large-scale production of IBC silicon solar cells, based on a photolithography method, for application in a solar vehicle, Honda Dream. [183] Despite a

remarkable efficiency of IBC silicon solar cells, these devices did not pass a feasibility test, due to their complicated and costly manufacturing process. However, over time the technology spread across other types of solar cells, including DSSCs [184] and most recently perovskite solar cells.

The structure of an IBC PSC is pictured on **Figure 2.5b**. The IBC electrodes lay on the bottom of the device and consist of two comb-shaped electrodes, covered by HSL and ESL. A perovskite layer is deposited on the top of the pre-made electrode pattern, as a last step of the device fabrication. This avoids a number of processing issues encountered in the fabrication of planar PSCs, affecting the quality of the photo absorbing layer. As an example, methods used to deposit materials on top of the perovskite layer in the planar structure are constrained by the chemical compatibility with the perovskite material (i.e. cannot dissolve or interact with the perovskite layer in an unwanted and uncontrollable manner); whereas in the IBC structure this problem is eliminated. Furthermore, the IBC architecture not only eliminates the transmission and/or shading losses of the initial flux, but also allows for illumination of the SC from the top and the bottom sides of the device. The double-side illumination of planar PSCs is also possible if both electrodes and charge selective layers are transparent (or semi-transparent), which further limits the choice and thickness of functional materials.

In an IBC PSC, the charge transport occurs in the direction parallel to the device plane; whereas, in the planar structure charges travel perpendicularly to the device plane. Due to the micron and sub-micron range charge diffusion length in polycrystalline perovskite material, the gap between rear electrodes has to be of similar dimensions or smaller in order to collect the charges efficiently. The distance between the electrodes plays a crucial role in the IBC device performance, therefore, the manufacturing process of IBC electrodes is rather challenging and requires the use of sophisticated equipment and a clean room facility. One of the methods allowing for manufacturing such structure is photolithography, described in detail in Chapter 3 of this Thesis. In this technique, a limiting factor, constraining the minimum size of the electrodes is the occurrence of the UV light diffraction on the patterned mask. The diffracted light causes an overexposure of the photoresist and a failure to obtain the photoresist pattern. The effects of this diffraction become more prominent as the width of the electrodes becomes narrower. Thus, the smallest pattern of IBC electrodes obtained by our research group has an electrode width of 4 μm and the gap between the electrodes of 4 μm, still significantly exceeding the career diffusion length in perovskite materials. [185] Other research groups working in the IBC PSCs field produce devices with the gap width of the order of hundreds of micrometres. [186], [187]

Narrowing the gap between the positive and negative electrodes increases the possibility of a short circuit between the electrodes. As we observed, this is usually caused by the imperfections of the photoresist pattern (e.g. local overexposure, caused by a ununiform light source or uneven photoresist thickness) or insufficient lift off. In order to tackle this issue, our research group was the first to propose the use of quasi-interdigitated back-contact electrodes for perovskite solar cells. [188]

2.3.3 Quasi-interdigitated back-contact perovskite solar cells

The structure of a QIBC PSC is pictured on **Figure 2.5c**. This architecture is a hybrid of a planar and the IBC devices. One of the rear electrodes is comb-shaped, whereas the other one is planar. Both of the electrodes are covered with their corresponding charge selective layers and are separated by a layer of an insulator. This architecture holds all the advantages of a traditional IBC structure (i.e. the lack of transmission and shading losses, perovskite deposition as a last step of the device fabrication, double-sided illumination), simultaneously vastly reducing the possibility of an accidental short circuit of the electrodes. The method of fabrication of QIBC PSCs developed by Jumabekov *et al.* [188] allows for fabricating a comb-shaped electrode with teeth width of 2 μm and the gap between the teeth of 2 μm. However, given the position of the electrodes and thus, the modified direction of the charge transport, the longest distance that charges need to travel to reach an electrode is shorter than this value.

Numerical simulations performed by Ma *et al.* [189] show that decreasing the distance that charges need to travel in order to reach their corresponding electrode plays a significant role in the device performance. By varying a width of the gap between the IBC electrodes from 100 nm to 50 μm, Ma noticed a drastic drop in the short circuit current (from 23.6 mA cm^{-2} to 4.7 mA cm^{-2}) and the efficiency (from 22.1% to 4%) of the simulated device. The fill factor of the simulated device was also reduced for gap widths of 1 μm and above. This is caused by the reduction of the electrical field between the electrodes, affecting the charge collection efficiency of the IBC devices. In the same work, Ma suggested that adopting the QIBC electrodes for perovskite devices may be beneficial for the device performance, because in this structure the cathode and the anode are separated only by a several hundred nanometres thick insulating layer.

The need to decrease the distance between the electrodes became even more pronounced in the study performed by Lin *et al*. [190] In his work, Lin observed an increase in density of grain boundaries (GBs) in perovskite material when the layer was deposited on top of the gold IBC electrodes. This was compared to the density of GBs in perovskite materials deposited on a glass slide, as well as on a glass slide/flat gold layer substrate. It was discovered

that the topography and wettability of a substrate plays a significant role in the morphology of the perovskite layer. A larger density of perovskite GBs increases the charge recombination at the grain/grain interfaces, thus reducing the efficiency of the device. Hence, narrowing the distance which charges need to travel in order to reach the electrode (and thus the number of GBs on their way) may be a crucial step to increase the efficiency of the IBC and QIBC perovskite devices.

Strategies to minimise the charge travelling distance involve modifying the shape of the comb electrode, as well as developing new techniques for device fabrication, which exceed the limits of photolithography. In the structure proposed by Hou *et al.* the comb-shaped electrode was replaced by a honeycomb-like one (HQIBC electrodes). [191] Despite the use of photolithography, Hou was able to obtain circular gaps with a diameter of 2.7 μm, and a 1.3 μm spacing between the edges of the circles (**Figure 2.6**), shortening the charge pathways and simultaneously improving the robustness of the structure.

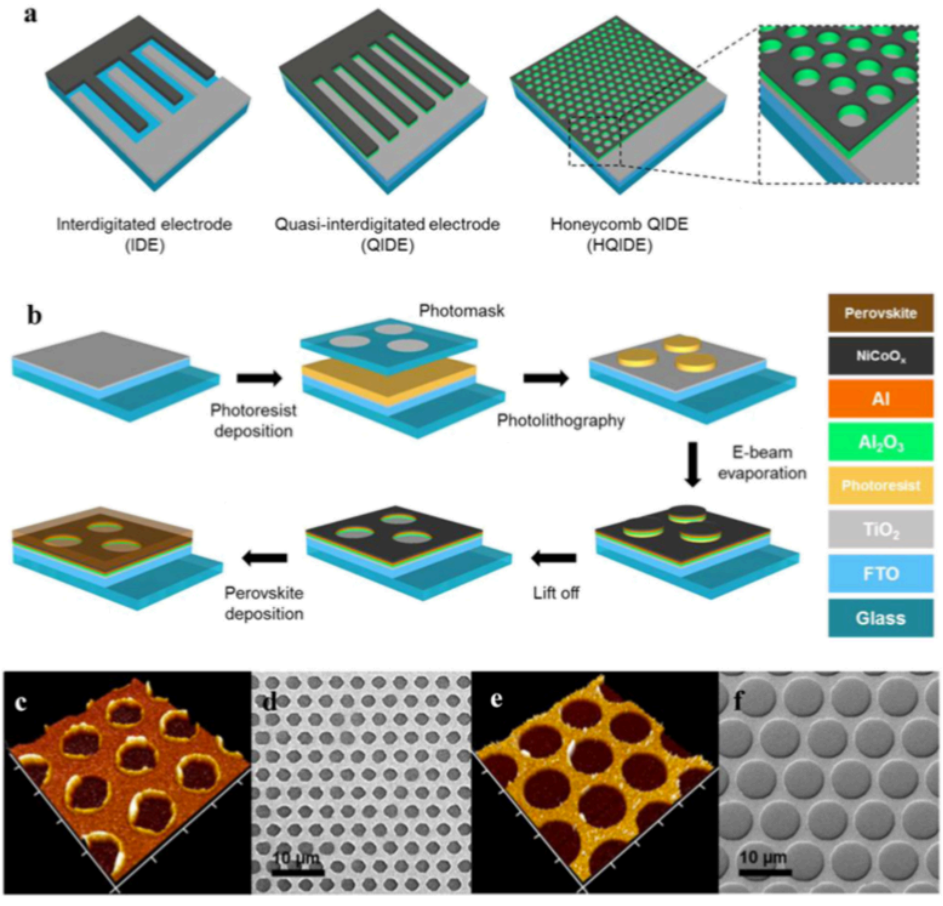

Figure 2.6. (a) A comparison of the interdigitated back-contact electrodes, quasi-interdigitated back-contact electrodes and honeycomb quasi-interdigitated back-contact electrodes. (b) Diagram showing the process of manufacturing of the honeycomb quasi-interdigitated back-contact electrodes via photolithography. (c, e) AFM images of the honeycomb quasi-interdigitated back-contact electrodes of different sizes. (d, f) Corresponding SEM images of

the electrodes. Figure reprinted with permission from: [191] RightsLink® by Copyright Clearance Center.

In another study Jumabekov *et al.* attempted to developed a new method of manufacturing HQIBC electrodes, eliminating the photolithography step. [192] Using a modified natural lithography technique, Jumabekov deposited polystyrene nanobeads on top of a glass/FTO/TiO_2 substrate which created a mask for the deposition of an insulating layer and the cathode. This process was followed by the lift-off of the beads, oxidation of the cathode and the deposition of the perovskite layer (**Figure 2.7**). The density of the deposited beads was then significantly increased by Hou, [193] using a self-assembly nature of the beads, rather than surface functionalisation.

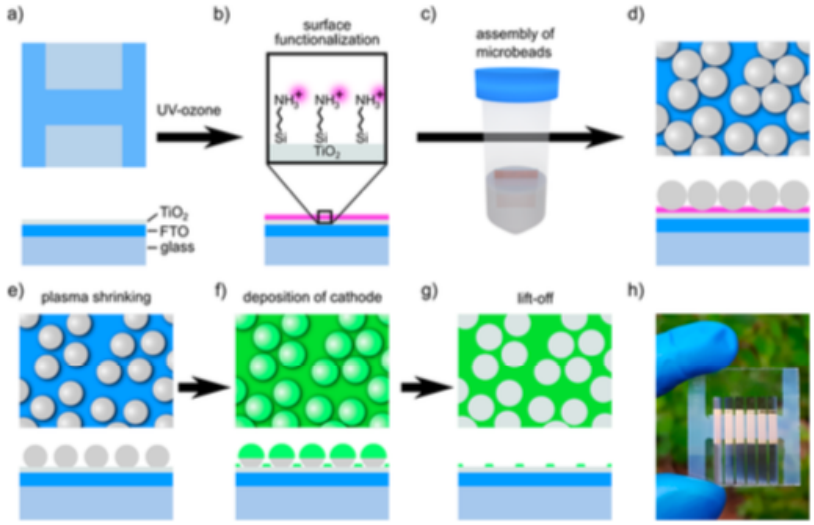

Figure 2.7. (a-g) Diagram showing the process of manufacturing of the honeycomb quasi-interdigitated back-contact (HQIBC) electrodes via modified natural lithography method. (h) Visual camera picture of a substrate containing 6 separate HQIBC devices, prior to perovskite deposition. Reprinted with permission from: [192]. Copyright (2019) American Chemical Society.

2.4 Applications of back-contact electrodes in perovskite solar cells field

The numerical simulations of back-contact perovskite solar cells performed by Ma *et al.* confirm that these devices have the potential to exceed the efficiencies of their planar analogues. In comparison to the planar architecture, back-contact devices are characterised by an advantageous light utilization (no transmission losses, no shading losses) and should theoretically generate a larger photocurrent. However, as of today, the efficiencies obtained with the IBC and QIBC perovskite devices cannot compete with the champion planar perovskite solar cells. This technology is relatively new and due to the low efficiencies have not attracted much attention from the broader research community. Nevertheless, a few

interesting applications of the back-contact electrodes were reported during the last few years, some of which gave inspiration to the experiments performed for the purpose of this Thesis.

2.4.1 Studies of electronic properties of the perovskite material using back-contact electrodes

The first back-contact perovskite device was reported by Xiao *et al.* [194] In his study, Xiao presented IBC perovskite devices, with both electrodes made of gold, without the use of any charge selective layers. The energy diagram of the so-prepared device was symmetric and did not provide any driving force for the charge extraction. Hence, measured under illumination, the solar cells did not generate any photocurrent. However, upon poling with a strong bias prior to the measurement, Xiao observed a temporally induced photocurrent, whose direction depended on the direction of the poling bias. The existence of this switchable photocurrent was attributed to the ion migration inside of the perovskite material. Drifting ions, accumulated next to the electrodes, induced a temporary p- and n- doping in the perovskite material, and created a driving force for charge separation and extraction. A similar effect was observed by Xiao on planar devices, also without charge selective layers, as well as in other studies performed by the same research group. [195], [196] The minimum distance between the cathode and anode of IBC electrodes used in Xiao's experiments was 8 μm, far exceeding the charge career diffusion lengths in perovskite material. However, in this experiment, the IBC electrodes were used to examine the fundamental properties of perovskite material, rather than creating an efficient device.

Similarly, the IBC electrodes used by Pazos-Outón *et al.* [186] were applied to examine electronic properties of the perovskite material. In this study, Pazos-Outón observed generation of photocurrent in perovskite material even at distances greater than 50 μm away from the IBC electrodes. Considering that the charge diffusion length in perovskite is a fraction of this distance, the charge transport in perovskite material must take place through multiple photon absorption – charge diffusion – radiative recombination – photon reabsorption processes ("recycling of photons"). This may be the reason why IBC perovskite devices with largely spaced electrodes are still able to generate photocurrents. Thanks to the IBC electrodes, Pazos-Outón was able to discover the effects that could not be observed with planar devices. This experiment also suggested the favourable application of perovskite materials in concentrator solar cells, where radiative recombination is dominant.

A great application of back-contact electrodes was presented by Alsari *et al.,* [187] who performed *in situ* measurements of the perovskite material during film formation. Alsari used the fact that perovskite deposition is the last step of device fabrication. This allows for the *in situ* electronic measurements of the device. This experiment was the inspiration for work

included in Chapter 4 of this Thesis. Traditionally, the method of perovskite deposition used in this study ($MAPbI_3$, prepared from MAI:$PbCl_2$ and hydroiodic acid and PbI_2 as additives, in N,N-dimethylformamide) requires annealing of the perovskite for 2 h at 100 °C. [197] However, Alsari was able to track the evolution of the devices' performance during annealing at few different temperatures and determine the time when the performance reaches its maximum.

In his work, Alsari used IBC electrodes, separated by a 100 μm gap, which, most likely, affected the electronic measurements of the perovskite material. The maximum photocurrent density obtained by Alsari was lower than 200 μA cm^{-2}, and with a FF of ~25%, the device efficiencies were negligible. In comparison, the gas-assisted method of deposition of perovskite used in Chapter 4 ($MAPbI_3$, prepared from MAI and PbI_2, in N,N-dimethylformamide) requires far shorter annealing times (10 min). [198] The QIBC electrodes used for this study are characterised by an incompatibly shorter charge traveling pathways. Furthermore, all devices presented in Chapter 4 demonstrated a measurable efficiency.

Numerous studies show that the morphology of the perovskite layer has a direct influence on the efficiency of perovskite devices. [199], [200] In the same time, the morphology is affected by the deposition methods and the environment in which this process was performed. Factors, such as the temperature and time of annealing, the concentration of individual components in precursor solution, the presence of additives, humidity, controlled solvent or antisolvent vapour exposure during the deposition play a crucial role in the process of manufacturing of highly efficient perovskite devices. In the crowd of so many variable parameters, the *in situ* measurements of perovskite material during film formation are a useful tool in the process of defining the most favourable conditions.

2.4.2 Other applications of back-contact electrodes in perovskite solar cells field

Coupled optical-electrical modelling performed by Adhyaksa *et al.* [201] show the superiority of application of QIBC PSC in tandem perovskite/silicon solar cells. In his work, Adhyaksa was comparing three different architectures of tandem perovskite/silicon solar cells, presented in **Figure 2.8**. The conventional tandem solar cells (TSCs) are fabricated in either 2- or 4-terminal architectures. 2-Terminal TSCs require current-matching of the sub-cells, to allow both devices to work close to their maximum power point (MPP). In this configuration, both sub-cells are connected in series and the output current is limited by the cell that produces lower current at given applied voltage. In contrast, both sub-cells in the 4-terminal TSCs work independently, however the device suffers from transmission and reflection losses occurring at the interface of the sub-cells. The structure proposed by Adhyaksa consists of 3 terminals: the

patterned QIBC top cathode and IBC electrodes, located at the bottom of the silicon sub-cell. The sub-cells are separated from each other by an electron selective layer, which injects electrons generated in perovskite to the bottom (silicon) sub-cell. By modelling such structures, Adhyaksa obtained a 32.9% power conversion efficiency of 3-terminal TSC, whereas 2- and 4-terminal reached 24.8% and 30.2% respectively.

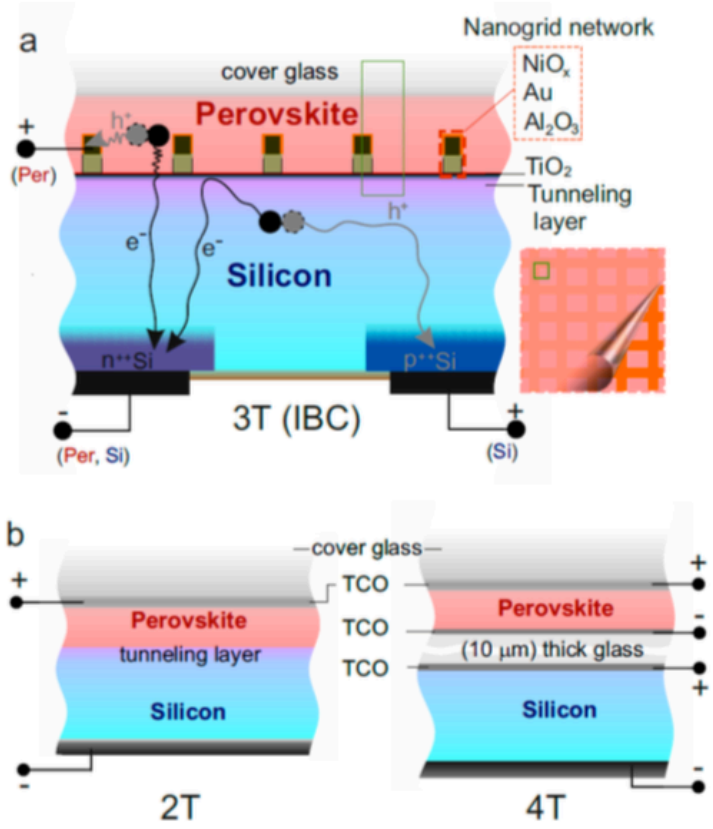

Figure 2.8. (a) 3-terminal tandem perovskite/silicon solar cell. Top (perovskite) solar cell has QIBC architecture, bottom (silicon) solar cell has IBC architecture. (b) 2-terminal tandem perovskite/silicon solar cell. Both solar cells have a planar architecture and share the electrodes. The solar cells are separated by a tunnelling layer. (c) 4-terminal tandem perovskite/silicon solar cell. Both solar cells have a planar architecture and separate electrodes. Reprinted with permission from: [201] Copyright (2017) American Chemical Society, under Creative Commons Attribution Non-Commercial No Derivative Works (CC-BY-NC-ND) 4.0 license.

An interesting application of QIBC electrodes was presented by DeLuca *et al.* [202] In his study, DeLuca manufactured transparent electrodes for the creation of semitransparent perovskite solar cells. In this device, the bottom flat electrode was made of FTO, with a TiO_2 electron selective layer deposited via spray pyrolysis. The comb-shaped ITO electrode was made through a photolithography technique and subsequently covered with a hole selective layer of copper(I) thiocyanate, deposited via an electrochemical method. Despite its rather low efficiency (1.7%), DeLuca showcased a new potential material choice in QIBC electrodes for

application in the tandem solar cells field. This is because the transparent QIBC electrodes allow for transmission of the unabsorbed light by through the device, rather than being reflected from the metal contacts. This light can be then absorbed by the bottom sub-cell of the tandem configuration.

Recently, Wong-Stringer *et al.* [203] reported a new process of manufacturing BC electrodes for flexible PSCs. In his work, Wong-Stringer embossed a polymer substrate to obtain grooves, presented on **Figure 2.9**. Thanks to the directional e-beam evaporation, the walls of the grooves were subsequently coated with the electrodes and charge selective layers. As a last step, so-prepared substrate was covered with a perovskite material.

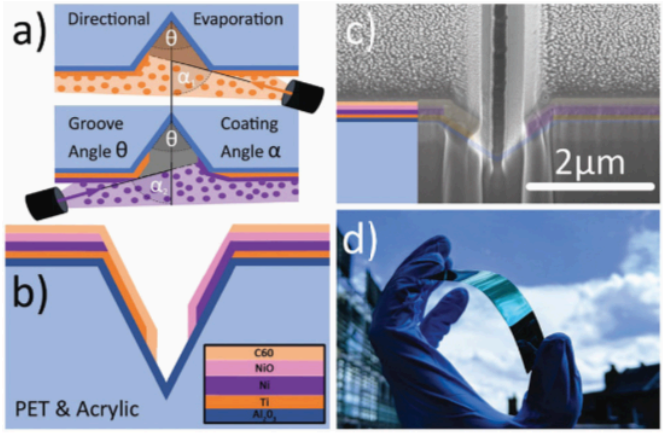

Figure 2.9. (a) Directional evaporation of the electrodes and charge selective layers on top of the patterned flexible substrate. (b) Schematic illustration of so-prepared back-contact electrodes. (c) Scanning electron microscope image of the back-contact electrodes. (d) A visual image of the flexible substrate with back-contact electrodes, prior to perovskite deposition. Reprinted from: [203] under Creative Commons Attribution 3.0 Unported Licence.

In Wong-Stringer's device, a single groove acts as a solar cell, demonstrating stabilised efficiencies as high as 7.3% (J_{SC} = 22.33 mA cm^{-2}, V_{OC} = 0.91 V, photoactive area: 6.4x10^{-5} cm^2). By interconnecting 16 of the grooves in series, Wong-Stringer created a micromodule, with open circuit voltages up to 14.6 V. However, the efficiencies measured on so-prepared micromodule dropped significantly (η = 2.63%, J_{SC} = 0.42 mA cm^{-2}), due to the large, photo - inactive space between the grooves. It is clear that the devices presented by Wong-Stringer need further optimisation. However, one must remember that this study was the first attempt showing a new method of fabrication of BC electrodes. Interestingly, all techniques used in electrodes fabrication are applicable to roll-to-roll processing and may potentially be implemented in large scale production of BC PSCs.

2.5 Passivation of perovskite solar cells. Post-treatment strategies.

The multilayer nature of PSCs leads to multiple interfaces between the functional layers: TCO/ESL, ESL/Perovskite, Perovskite/HSL, HSL/rear contact, rear contact/air. Those interfaces cause numerous trap states – "hot spots" for charge recombination, which largely contribute to the current loss in PSCs. The trap states are formed by crystal defects at the surface of a layer, where the external halide ions of perovskite cannot bind with their (missing) neighbouring atoms. Those ions possess under-coordinated valence electrons that attract photogenerated holes and recombine with them, decreasing the photocurrent. Similarly, the trap states are present at the GBs of the perovskite material itself (perovskite/perovskite interface)

To address this issue, many efforts were undertaken to passivate the interfaces and GBs in PSCs, resulting in significant increase in device performance, improved stability and reduced hysteresis. Examples of the strategies used to passivate surfaces of the charge selective layers include: coating it with a thin layer of an insulating polymer, [204] [205] or self- assembled monolayers, [206]–[211] or carboxyl groups, [212] as well as doping of the material. [213], [214]

Interestingly, modulated surface photovoltage spectroscopy studies performed by Supasai *et al.* [215] show the self-passivation nature of GBs in a $MAIPb_3$ layer in the presence of excess PbI_2. This hypothesis was also investigated by time-resolved femtosecond transient absorption spectroscopy experiments, performed by Wang *et al.* [216] It was discovered that PbI_2 – rich perovskite layers show slower relaxation rates, in comparison to the samples with stoichiometric PbI_2:MAI ratios and PbI_2-poor perovskite crystals. This observation was credited to the passivation of the perovskite GBs by PbI_2. It was reported in other studies that the excess PbI_2 causes a reduction in hysteresis [217] and an increase in the open circuit voltage. [218] In contrast, many researchers believe that the presence of unreacted PbI_2 in the perovskite layer has a negative impact on the device performance. Upon increasing the concentration of PbI_2 in the precursor solution, Jacobsson *et al.* [219] observed a decrease in open circuit voltage of the device and an increase in the hysteresis. Similarly, Liu *et al.* [220] observed that PbI_2-rich PSCs undergo illumination and humidity degradation much faster than the regular devices. Additionally, other studies show that the deficiency of PbI_2 can lead to self-passivation of $MAIPb_3$ GBs by MAI [221] and increased stability in humid environments, [222] as well as that a thin MAI layer deposited on top of the perovskite material can passivate the perovskite/HSL interface. [223]

The ideal PbI_2:MAI stoichiometry ratio of perovskite precursor solution is still a matter of dispute in perovskite field. Recently, researchers reported passivation of GBs, achieved by adding PCBM [224] or graphene quantum dots [225] to the precursor solution. PCBM can also

be deposited on top of the perovskite layer (surface passivation) and diffuse into the perovskite GBs (GBs passivation) upon a heat treatment. [226]

Different post-treatment strategies are used in the process of reducing the number of defects and passivation of the perovskite material, some of which gave the motivation for experiments included in Chapter 5 of this Thesis. Studies show that exposing the perovskite layer to a methylamine vapour allows for the recrystallisation of this material and forms a new perovskite film with less defects. [227] This "healing method" results in decreased charge recombination and increased charge carrier lifetimes. Additionally, studies show that the exposed samples are characterised by a significantly improved stability. [228], [229] It is important to mention that the methylamine vapour does not passivate perovskite GBs, however, the recrystallisation process largely decreases the number of GBs and thus, the number of trap states present at perovskite/perovskite interfaces. A similar strategy was presented by Zhu *et al.* [230] In his work, Zhu significantly improved the crystallinity of a perovskite film and reduced the number of pin holes in the layer by exposing it to N-N dimethylformamide vapour. This was done by multiple cycles of vapour fumigation (perovskite dissolution) and sample annealing (perovskite recrystallisation) in an inert atmosphere. So-prepared samples showed decreased hysteresis, a significant increase in photogenerated current as well as higher open circuit voltage. Zhu was able to boost the average initial efficiency of devices from ~5% to ~10% after six recrystallisation cycles.

Interesting results were reported by Abate *et al.* in 2014, [231] which shined a light on the fundamental mechanisms taking place during the passivation process. In his work, Abate discovered that the presence of under-coordinated halide anions causes charge accumulation at the perovskite/HSL interface, leading to an unfavourable charge density profile within the HSL and the perovskite layer. This reemphasised the need for surface passivation. Abate passivated the top surface of the perovskite layer by immersing it in iodopentafluorobenzene (IPFB) for few minutes. Through solid state ^{13}C and ^{19}F nuclear magnetic resonance measurements, he observed that IPFB molecules self-assemble on the surface of $MAPbI_3$ and create halogen bonding with the perovskite crystal (**Figure 2.10**)

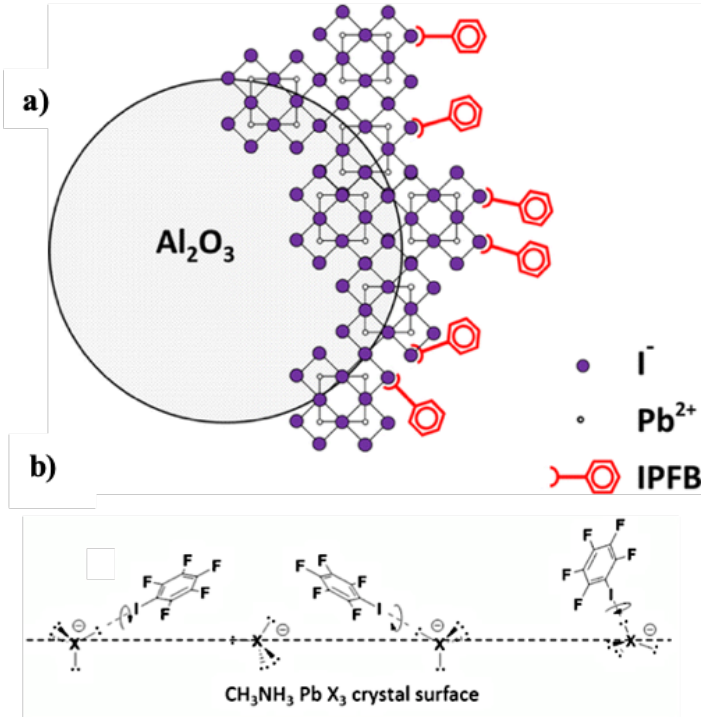

Figure 2.10. Surface passivation of $MAPbI_3$ by IPFB. (a) Schematic illustration of IPFB molecules attached to the perovskite crystals. (b) Self – assembly of IPFB on the crystal surface. Reprinted from: [231] under American Chemical Society Licence (2019).

Noel *et al.* [232] performed similar experiments using pyridine and thiophene to passivate the top surface of perovskite layer. However, instead of dipping the sample into those Lewis bases, she diluted a small volume of the passivators in chlorobenzene and spin-coated on top of the perovskite layer prior to HSL deposition. The method developed by Noel improved the control of perovskite-passivator interaction, as she was able to tune the amount of the passivating agent by varying its concentration in the solution. Through photoluminescence measurements, Noel observed a significant decrease in nonradiative recombination and a longer charge carrier life time for all post-treated samples. On average, the power conversion efficiency of the devices increased from 12.1% to 14.3% (for thiophene) and 15.5% (for pyridine).

This work was then continued by Yue *et al.*, [233] who combined the passivation and HSL deposition steps. He mixed different pyridine-based additives into the HSL solution and spin-coated it on top of the perovskite layer. All passivated samples performed better than the reference (not passivated) sample. However, he observed that over time perovskite surface crystals exposed to pyridine, 4-tert-butyl pyridine (TBP) and 4-amylpyridine (4AP) undergo corrosion by forming a new complex with the additive, as shown by XRD diffraction patterns. This additional XRD peak was also observed during the experiments preformed in Chapter 5 of this Thesis. On the other hand, additives with long-alkyl-chain at their *o*-position (2-

amylpyridine (2AP) used in this study) can passivate the perovskite surface without damaging it. Hence, samples passivated with 2AP show superior long-term stability during the 900 hours - long efficiency measurement test, in comparison to pyridine, TBP and 4AP.

Another interesting study was performed by Jain *et al.,* [234] who exposed perovskite layers to a pyridine vapour. Jain observed that upon exposure, the perovskite undergoes an optical bleaching, followed by the recovery of the perovskite black phase. The exposure/recovery process was performed at room temperature, in ambient as well as in a nitrogen atmosphere. The recovered perovskite film shown much larger grain size and increased light absorption. The improved quality of the recovered film was also observed via photoluminescence studies. In comparison to the non-treated samples, solar cell devices featured with pyridine-treated perovskite layer showed larger short circuit currents, significantly larger open circuit voltage and a negligible hysteresis, which in total doubled the device efficiencies.

The studies presented above can be significantly improved by utilising QIBC electrodes. In all cases where the passivating agent was spin-coated on top of the perovskite layer, the ideal amount of the reactant is unknown. In order to find the desired ratio of reactant volume to the perovskite surface area, one has to manufacture hundreds of planar solar cells, varying the concentration of the reactant in the spin-coated solution. This process has to be followed by the deposition of the remaining functional layers and photovoltaic measurements.

The pyridine vapour exposure was performed in an uncontrolled environment, simply holding the sample above a beaker with the evaporating reactant for one minute. The amount of pyridine interacting with the perovskite surface is unknown and the influence of the ambient temperature on the evaporation rate was not investigated. Similarly, the ideal volume of DMF and methylamine used in the recrystallisation studies was not investigated due to the workload needed to define it.

The pilot experiment introduced in Chapter 5 of this Thesis allows for a quick determination of the reactant volume (or mass) to achieve a desired effect at given process parameters, saving weeks of work. A higher level of control was introduced by diluting the reactant vapour with a nitrogen gas and performing the experiment in a nitrogen atmosphere. The *in situ* electronic measurements allow us to observe a real time reaction of the solar cell performance to the gas exposure and to stop the experiment when the efficiency reaches its peak. The results of this experiment can be directly transferred to the planar devices to further boost their efficiency.

3. Experimental Methods

3.1 Sample preparation

All photovoltaic devices presented in this Thesis share the same architecture, utilising quasi-interdigitated back-contact electrodes, presented in **Figure 2.5c**. The samples are manufactured using a modified method, previously published by Jumabekov *et al.* [188] The procedure can be split into 6 stages, pictured on **Figure 3.1**.

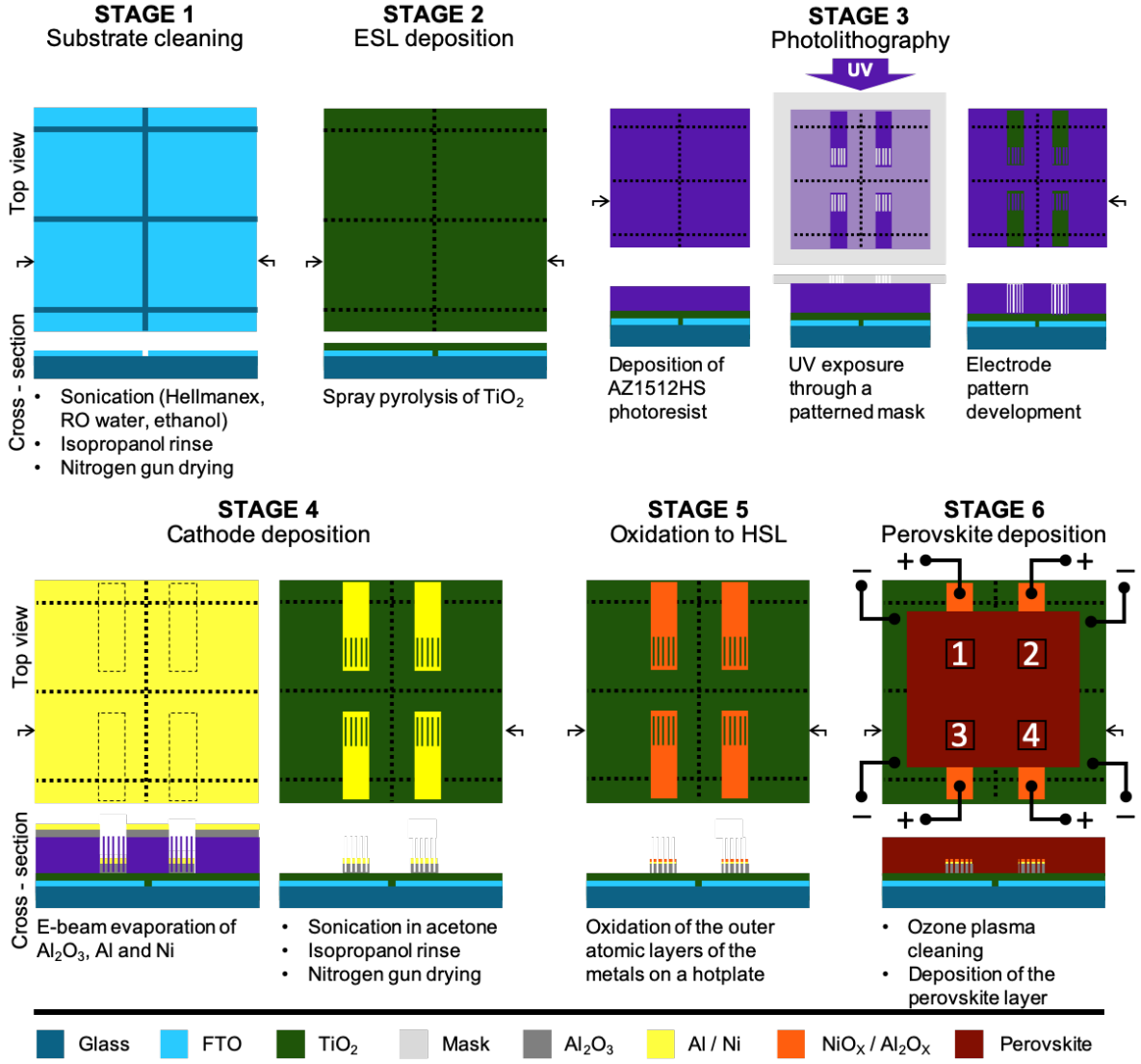

Figure 3.1. Sample preparation divided into 6 stages: substrate cleaning, deposition of ESL layer, photolithography, deposition of a cathode, oxidation to HSL shell and deposition of perovskite. The final sample consists of 4 separate solar cells.

The process starts with substrate cleaning (**Figure 3.1, STAGE 1**). 25 × 25 mm patterned FTO-coated glass pieces are sonicated for 15 min in Hellmanex (v/v 1:99 in RO water), then in RO water (10 min), and ethanol (15 min). Next, the substrates are rinsed with isopropanol and dried with a nitrogen gun.

Subsequently, the TiO_2 layer is deposited via spray pyrolysis (**Figure 3.1, STAGE 2**). In this process, the substrates are heated to 500 °C (approximate rate 15 °C/min) and kept at this temperature for 10 min. Next, a solution of titanium diisopropoxide bis(acetylacetonate) (v/v 1:19 in isopropanol) is uniformly sprayed across the substrate. After the deposition, the temperature of the glass is maintained at 500 °C for an additional 10 min and then allowed to cool to room temperature while remaining on the hot plate. The TiO_2 layer acts as an electron selective layer, resting on top of the FTO anode.

So-prepared substrates undergo photolithography in order to achieve the comb-shape pattern of the cathode (**Figure 3.1, STAGE 3**). An approximately 2 μm thick layer of AZ1512HS photoresist is spin-coated onto the substrate (acceleration: 1000 rpm/s for 8s, constant speed: 8000 rpm for 30 s, deceleration: 1000 rpm/s for 8 s) and baked for 2 min at 110 °C. Next, the samples are exposed to UV light (specific power 14.73 mW cm^{-2} at 365 nm, 2.6 s), through a patterned chrome photomask. The structure is then developed in AZ726MIF (v/v 3:1 in water) for approximately 1 min.

As a next step, the cathode of the solar cell is deposited, preceded by an insulating layer that separates the electrodes (**Figure 3.1, STAGE 4**). An approximately 150 nm thick layer of Al_2O_3 (insulator) is deposited using an e-beam evaporator, followed by ~30 nm of Al and ~50 nm of Ni (metals). The photoresist is removed by sonication in acetone for approximately 10 min (lift-off process). The substrates are rinsed with isopropanol and dried with a nitrogen gun.

The hole selective layer is created by annealing the samples on a hotplate at 300 °C for 15 min (**Figure 3.1, STAGE 5**). In this process, the outer atomic layers of Ni and Al undergo an oxidation to form a NiO_x and Al_2O_x shells surrounding the cathode.

As a final step of the sample preparation, all substrates are treated for 10 min with ozone plasma, and immediately after the perovskite layer is deposited (**Figure 3.1, STAGE 6**). In Chapter 4 and Chapter 5 of this Thesis, a methylammonium lead iodide perovskite layer was deposited via a gas-assisted method. In Chapter 6 the mixed-cation and mixed-anion $Cs_{0.05}FA_{0.79}MA_{0.16}PbI_{2.49}Br_{0.51}$ perovskite was deposited via an antisolvent method. Both methods utilise a centrifugal force in order to achieve a few hundred nanometre-thick, homogenous perovskite layers. The perovskite deposition methods are described later in this Chapter.

So-prepared samples consists of 4 solar cells (active area 0.04 cm^2). Due to the pre-patterned FTO substrate, all solar cells can be measured independently. In contrast, our previously reported devices consisted of 6 solar cells, all sharing the same FTO anode. Hence, the devices very often suffered from an interconnection, which was particularly disruptive during the electronic measurements. **Figure 3.2a** shows an image of the sample. The area marked in red was magnified with optical microscope (**Figure 3.2b**).

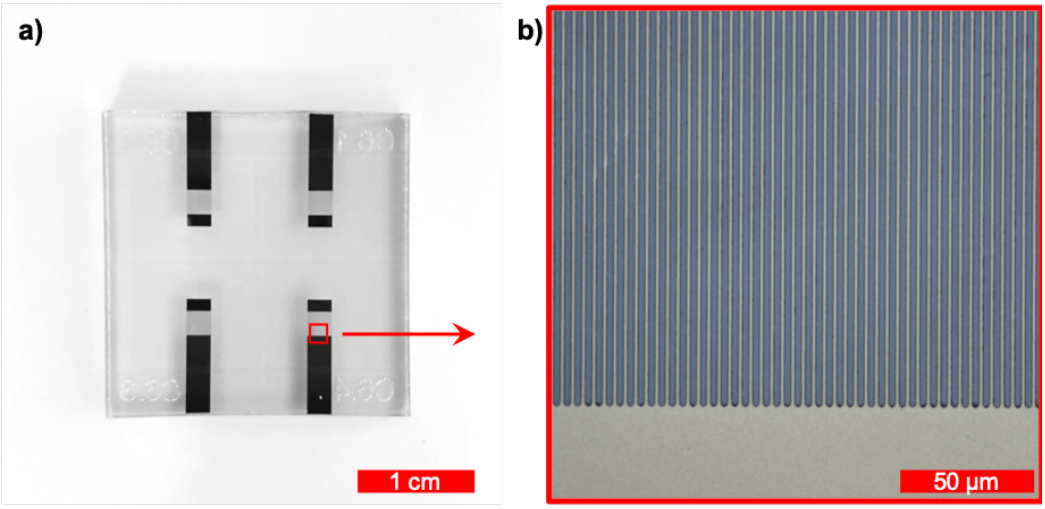

Figure 3.2. (a) a visual camera image of the top view of the sample, with (b) magnified area taken with optical microscope.

The profilometer analysis of the electrode after completing STAGE 5 of device fabrication (without the perovskite layer) is presented on **Figure 3.3a**. The area coloured with red represents a comb-shaped cathode.

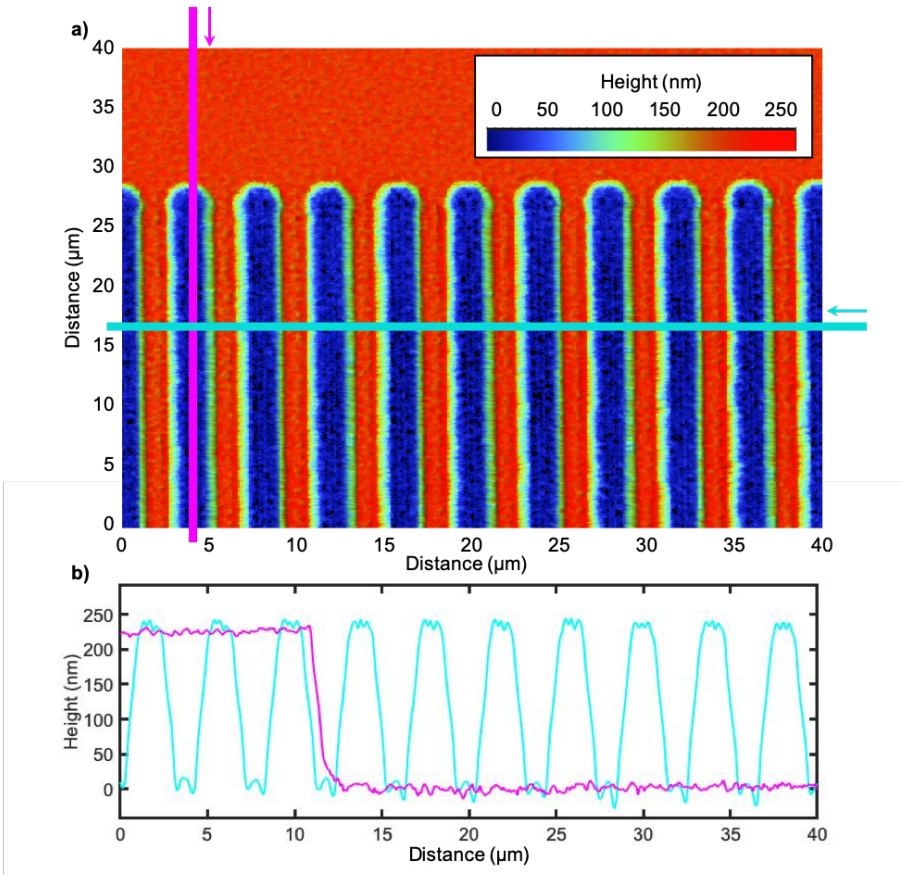

Figure 3.3. (a) Profilometer image of the top view of the electrode. (b) Profiles of the device taken in the parallel (pink) and vertical (cyan) direction to the comb-shaped electrode.

The profilometer measurement shows a slight slope of walls of the comb-shaped electrode **Figure 3.3b**. However, the ratio of the area of interfaces HSL/perovskite and ESL/perovskite is still approximately 1:1. The small size of the features (cathode width – 2 µm, gap width – 2 µm) requires pushing the resolution of the photolithography to its very limits. Hence, optimising the photolithography parameters (i.e. photoresist thickness, UV exposure time, sample development time) is crucial in the process of manufacturing the QIBC electrodes. A slight nonuniformity of the UV light source or variation of the photoresist thickness across the sample can result in UV overexposure (wider gap width) or UV underexposure (narrower gap width) and influence the mechanism of charge collection.

3.2 Deposition of the photoactive perovskite layer.

Spin-coating is the most widely used technique of depositing perovskite films on the laboratory scale. This method allows for obtaining a uniform film on a relatively small substrate and with a minimum use of the precursor solution.

3.2.1 Gas-assisted method for deposition of methylammonium lead iodide

In Chapter 4 and Chapter 5 of this Thesis the photoactive perovskite material was deposited via a gas assisted method, developed by Huang *et al.* [198] A 50 wt% stoichiometric solution of CH_3NH_3I and PbI_2 in DMF was prepared and deposited in a nitrogen atmosphere. Approximately 40 μL cm^{-2} of precursor solution was spread on the substrate before spinning. The samples were spin-coated at 6500 rpm for 30 s (acceleration 6500 rpm). A stream of nitrogen gas was introduced at 2.5 s for the duration of 10 s. In Chapter 4, the spin-coating process was followed by *in situ* measurements during annealing at various temperatures. In Chapter 5 all samples were annealed at 100 °C for 10 min. This process results in deposition of ~600 nm / 400 nm (QIBC cathode / anode) thick layer of $CH_3NH_3PbI_3$ ($MAPbI_3$).

3.2.2 Antisolvent method for deposition of a mix-cation perovskite film

In Chapter 6 of this Thesis, the photoactive perovskite layer was deposited via an antisolvent method. The precursor solution was prepared in a nitrogen atmosphere by dissolving CH_5IN_2 (1 mmol), PbI_2 (1.1 mmol), CH_3NH_3Br (0.2 mmol) and $PbBr_2$ (0.22 mmol), CsI (0.065 mmol) in 1 mL of mixed solvent of DMF:DMSO (v/v 4:1) to achieve a final composition of $Cs_{0.05}FA_{0.79}MA_{0.16}PbI_{2.49}Br_{0.51}$ with a concentration 1.32 M. Deposition of the perovskite was achieved by spin-coating 50 μL cm^{-2} of the precursor solution using a two-step program: 10 s at 1000 rpm (1000 rpm s^{-1} ramp) and then 20 s at 6000 rpm (6000 rpm s^{-1} ramp). 200 μL of chlorobenzene was deposited onto the spinning substrate 5 s prior to the end of the second step. The substrates were then annealed in the dark at 100 °C for 1 h and then allowed to cool down to room temperature naturally. All procedures were carried out in a N_2-filled glove box. This process results in deposition of ~600nm/400nm (QIBC cathode/anode) thick layer of $Cs_{0.05}FA_{0.79}MA_{0.16}PbI_{2.49}Br_{0.51}$.

3.3 Solar simulator measurements of perovskite solar cells

The most common instrument used for the examination of the solar cells is a solar simulator. During the solar simulator measurements, devices are illuminated with a lamp (usually Xenon), equipped with a filter, which imitates the solar spectrum. The samples are kept under Standard Measurement Conditions (Air mass 1.5 spectrum, light intensity 100 mW cm^{-2}, cell temperature of 25 °C). The standardised methods for solar cells measurements are crucial for comparing device performances between different research centres. Additionally, all champion solar cells (with record efficiencies) are examined by independent certified test centres (e.g. National Renewable Energy Laboratory NREL, USA).

Current-voltage characteristic measurement allows for determining the value of the power conversion efficiency (PCE, η) of a solar cell, alongside with its other electronic parameters, such as short circuit current density (J_{SC}), open circuit voltage (V_{OC}) and a fill factor (FF). The measurement is performed by applying voltage bias across the terminals of an illuminated solar cell and recording a photogenerated current. During the measurement, the voltage undergoes linear sweeping within a predefined range and the current recorded at different bias values gives the shape of the I-V curve. The voltage can be altered from lower to higher values (forward scan) or in an opposite direction (reverse scan). The photocurrent is usually presented in units of mA cm^{-2} (current density) to ease the comparison between solar cells of different photoactive areas. An example of a current density – voltage (J-V) characteristic is presented on **Figure 3.4**.

The power density (P_ρ) curve is generated by multiplying the values of voltage and its corresponding photocurrent density. The maximum power point (MPP) determines a value of voltage (V_{MPP}) at which a solar cell should be operated to give a maximum power density output ($P_{\rho(OUT)} = \max$). J_{MPP} represents the corresponding current density.

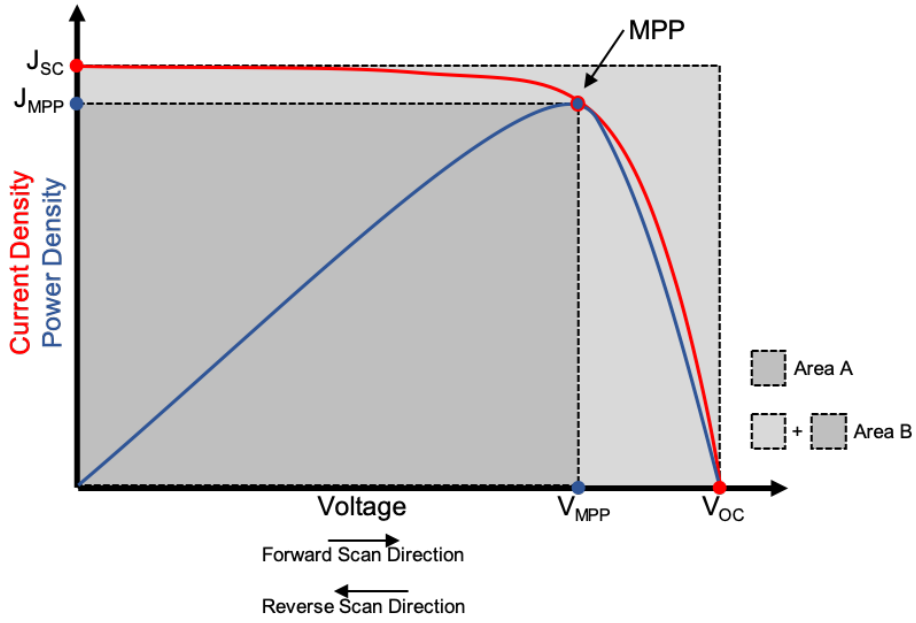

Figure 3.4. An example of a current density-voltage characteristic of a solar cell with a corresponding power density curve.

As shown on **Figure 3.4**, the V_{OC} represents a bias voltage, at which the measured photocurrent is equal to zero and J_{SC} represents the highest photocurrent density generated by a solar cell, without the bias voltage.

The FF of a solar cell is measured according to the equation:

$$FF = \frac{V_{MPP}\, J_{MPP}}{V_{OC}\, J_{SC}}$$

Graphically, it is a ratio of Area A to Area B marked in different shades of grey on **Figure 3.4**.

Under ideal conditions, the J-V graph of a solar cell would have a nearly quadratic shape, with the length of the sides determined by values of J_{SC} and V_{OC}. This solar cell would generate a photocurrent close to its short circuit value at any voltage from range 0 - V_{OC}. The FF of such solar cell would have a value approaching 1. In practice, parasitic resistive losses (series resistance and shunt resistance) and charge recombination cause "rounding" of a J-V curve and reduce the value of the FF. [235] Hence, the FF can be understood as a parameter describing the quality of a solar cell.

With such defined parameters, the efficiency of a solar cell generating power density $P_{\rho(OUT)}$ under the illumination of power intensity $P_{\rho(IN)}$, can be calculated using the equation:

$$\eta = \frac{P_{\rho(OUT)}}{P_{\rho(IN)}} = FF\frac{V_{OC}\, J_{SC}}{P_{\rho(IN)}} = \frac{V_{MPP}\, J_{MPP}}{P_{\rho(IN)}}$$

The J-V characteristics are performed with the intention of determining a steady-state power output of a solar cell. However, organic solar cells and dye-sensitised solar cells are known for showing different efficiency values, caused by light soaking prior to the measurement. [236]–[240] Similarly, the measurement of silicon solar cells can be influenced by extremely fast voltage sweep rate. [241] In other words, the J-V curves can appear different, depending on how its measurement was performed. This phenomenon is called a hysteresis.

Perovskite solar cells are infamous for experiencing significant hysteresis. The results of J-V measurements differ for different scan rates and when the cell is preconditioned (e.g. light soaking, high bias poling voltage). Unlike other types of solar cells, perovskite-based devices show hysteresis behaviour when measured in opposite scan directions, even at extremely slow scans and without any preconditioning. [242]–[244]

The origin of the hysteresis is the source of dispute within the perovskite community. One possible explanation of this phenomena can be related to ion migration within a perovskite material. Studies show that upon illumination, the excess ions present in the perovskite film

are able to travel towards either side of the film, causing a charge build-up. [245]–[248] Others suggest that the hysteresis may be related to the internal defects within perovskite material. Those defects are creating trap states for holes and electrons. The traps fill up under the open circuit voltage condition and undergo a discharge once the cell is scanned towards short circuit. Under the short circuit condition, the traps are emptied and charges are extracted to corresponding charge selective contacts. The traps fill up again during the forward scan, showing up as a decrease of the photogenerated current on the J-V curve. [242], [249]

The hysteresis phenomenon created the need to establish a strict protocol for reporting perovskite device efficiencies (i.e. reporting the scan rates and avoiding any preconditioning of the devices) and complementing the J-V scans with additional measurements, such as stable power output measurements or maximum power point tracking.

During the stable power output measurement, an illuminated solar cell is kept at a bias voltage for prolonged time. The value of the applied bias is calculated as an average of V_{MPP} measured in reverse and forward directions of the J-V scans. The power output is a result of multiplication of the applied bias and the photogenerated current. The measurement is continued until the photogenerated current (thus also the power output) reaches a stable value. In contrast, during the maximum power point tracking, the value of applied bias is not set to a constant value. A computer controlled potentiostat, will search for a bias voltage, at which the product of multiplication of photogenerated current and the bias voltage is maximum. In practice, the applied bias will oscillate around the V_{MPP} value and correct it if necessarily, to reach the maximum power output. Similar to stable power measurement, the maximum power output tracking is continued until it reaches a stable value.

3.4 Materials

The list of materials used in this Thesis together in the corresponding suppliers are listed in **Table 3.1**

Table 3.1. List of materials used in experimental parts of this Thesis, with corresponding suppliers.

Material	Supplier
Lead (II) iodide (99.9985%)	Alfa Aesar
Methylammonium bromide	GreatCell Solar
Formamidinium iodide	
Methylammonium iodide (≥99%, anhydrous)	
Lead (II) bromide (99.999%)	Sigma-Aldrich
Cesium iodide (99.999%)	
N,N-dimethylformamide (anhydrous, 99.8%)	
Chlorobenzene (anhydrous, 99.8%)	
Dimethyl sulfoxide (anhydrous ≥99.9%)	
2-propanol (anhydrous, 99.5%)	
Titanium diisopropoxide bis(acetylacetonate) (75 wt. % in isopropanol)	
Poly(methyl methacrylate) (average Mw ~996,000 by GPC)	
2-amylpyridine (≥97%)	
4-tert-butylpyridine (98%)	
Ethanol (for cleaning)	Univar
Acetone (for cleaning)	
2-propanol (EMPARTA) (for cleaning)	Merck
Hellmanex® III (for cleaning)	Hellma

Additionally, FTO-coated glass was FTO-P003 (<15 ohm/sq), high-purity nitrogen (99.999%; $O_2 \leq 2$ ppm, $H_2O \leq 0.1$ ppm) was used in all operations and whenever N_2 is mentioned.

4. *In situ* structural, optoelectronic and photovoltaic evolution of back-contact perovskite solar cells during film formation

4.1 Chapter introduction

An undeniable advantage of quasi-interdigitated back-contact perovskite solar cells (QIBC PSCs) is the possibility of performing *in situ* electronic measurements during the annealing of the perovskite layer. In contrast, in a conventional planar architecture, the photoactive perovskite film is sandwiched between two charge selective layers and the electrodes, and it is not possible to perform electronic measurements until the final electrode layer has been deposited.

Due to the presence of the BC electrodes during the deposition of the photoactive layer, one can directly track the evolution of the electronic properties of a perovskite film during its crystallisation. [187] This experiment has the potential to significantly accelerate the optimisation of deposition parameters. An obvious example of a tuneable process parameter is the annealing time. The optimum annealing time changes depending on the composition of the deposited perovskite and the solvents used in the process, [250], [251] annealing temperature [252], [253] and atmospheric conditions inside of the inert glovebox, [254] among many others. Conventionally, based on all of those variables, determining the ideal annealing time required manufacturing a large number of solar cells to create statistically significant optimised values and to eliminate experimental errors. [255]–[257] In contrast, the *in situ* tracking of the solar cell performance allows for the determination of the optimal time using only one device. Similarly, another application of *in situ* electronic measurements can be determining the ideal duration of vapour exposure during the solvent vapour-assisted deposition of perovskite. [258]–[260]

In this Chapter, a systematic *in situ* study of the structural, optoelectronic and photovoltaic properties of $MAPbI_3$ perovskite films on quasi-interdigitated back-contact electrodes (QIBC) has been performed during the layer formation at different annealing temperatures. The *in situ* open circuit voltage, short circuit current and J-V tracking measurements show the trends in charge extraction mechanisms and the evolution of the device performance. Additionally, the *in situ* photoluminescence measurements show changes in quenching mechanisms over time. The *in situ* X-ray diffraction analysis, complemented by SEM images, revealed the perovskite crystals growth process and the Scherrer analysis allowed for calculation of the evolution of the perovskite crystallite size.

Methylammonium lead iodide ($MAPbI_3$) was chosen as a photoactive material in this study due to its desirable properties, such as long carrier lifetimes (up to 3 ms), phenomenal charge

carrier mobility (up to 60 $cm^2\ V^{-1}\ s^{-1}$) and long diffusion lengths. [121], [198] Additionally, the ease of $MAPbI_3$ deposition (described in detail in Chapter 3 of this Thesis), i.e. at relatively low temperatures and short annealing duration, allowed for the thermal effects on the charge collective layers and the conductivity of the electrodes not to be considered in this study.

4.2 Results and discussion

As a first step, an FTO-coated substrate, of the same size as the substrates used in other experiments of this Chapter, was placed on a hotplate preheated to 40, 60, 80 or 100 °C, and was continuously monitored by a thermal camera. This was done in order to examine the time needed for the sample to reach the temperature of the hotplate.

4.2.1 Thermal imaging

The thermal images collected at the moment of first interaction (0 s), as well as after 10, 20, 30 and 40 s on the hotplate, are presented on **Figure 4.1a**. Due to the difference in emissivity of the FTO-coated glass and the metal surface of the hotplate, the temperature of the measured sample is compared to a reference sample already at a stabilised temperature. For the same reason, the area around the reference and measured samples visible on the figure appears darker than the reference sample. This gives the illusion of the temperature of the hotplate being lower than the temperature of the heated glass. Furthermore, the combination of reflection, thickness and physical state changes that occurs during the solution drying process and perovskite formation, causes even more complex changes in emissivity over time. Therefore, during those measurements, the samples were not coated with the photoactive layer. These conditions were accepted as a limitation of the thermal imaging method.

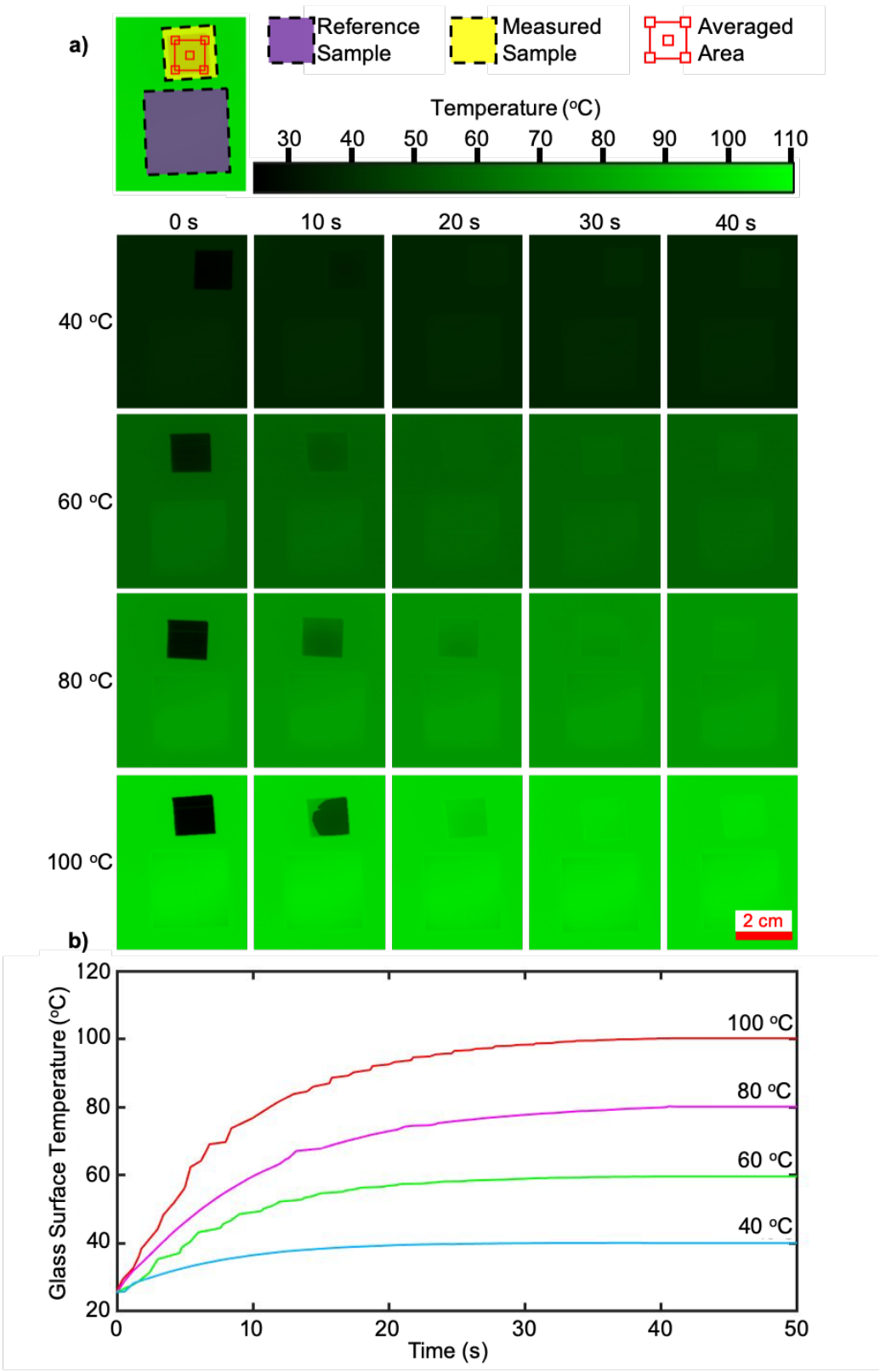

Figure 4.1. (a) Thermal images of the FTO-coated glass substrate (marked in yellow in the legend) and a reference sample (purple) placed on a hotplate set at different temperatures. Images taken after 0, 20, 30 and 40s. (b) Temperature of the top surface of the glass substrates measured over time. The curves are a result of a calculated average temperature over the area marked in red.

The *in situ* temperature measurements of the samples are summarised on **Figure 4.1b**. The curves represent the temperature of the top glass surface, calculated as an average over the area marked in red.

As seen in the graph, the top surface of the glass requires approximately roughly 20 s to achieve 40 °C when placed on a hotplate set to the same temperature. As expected, the heat exchange occurs faster with a greater difference in temperatures between the glass substrate and the hotplate. Therefore, the substrate needs only roughly 7, 4 and 2 s to achieve 40 °C when placed on a hotplate set to 60, 80 and 100 °C, respectively.

The initial rapid rise of the glass temperature slows down as the temperature of the substrate that of the hotplate. Hence, the final temperature of the substrate was achieved after ~35 s for the sample placed on 60 °C and roughly 40 s and 43 s for samples placed on 80 °C and 100 °C. The heating rate of a glass substrate is expected to further decrease once the sample is covered with a perovskite solution. This is due to the energy of heat being transferred to the latent heat of vaporization of the solvent and the formation of the perovskite crystals.

4.2.2 Perovskite crystal growth

The crystallisation process of the perovskite was studied using *in situ* X-ray diffraction measurements (XRD). In preparation for this experiment, a perovskite solution was spin-coated on top of a flat stack of TiO_2, Al_2O_3, Al, Ni, NiO_x layers deposited onto an FTO-coated glass substrate. Prior to the annealing step, the substrate was transferred to the XRD chamber and placed on a heating element. The first measurement (30 s long) was taken at room temperature. The stage temperature was then rapidly increased to 40, 60, 80 or 100 °C, while diffraction patterns were collected every 10.8 s for 15 min. Next, two additional diffraction patterns collected over 30 s at the temperature of the experiment and after the sample was cooled down back to the room temperature.

Figure 4.2a shows the time evolution of diffraction patterns of perovskite annealed at 40, 60 80 and 100 °C. The colours represent peak intensity, with red standing for the highest and blue for the lowest intensity. The intensity is calculated as a square root of the number of counts in order to enhance the brightness of the smallest peaks.

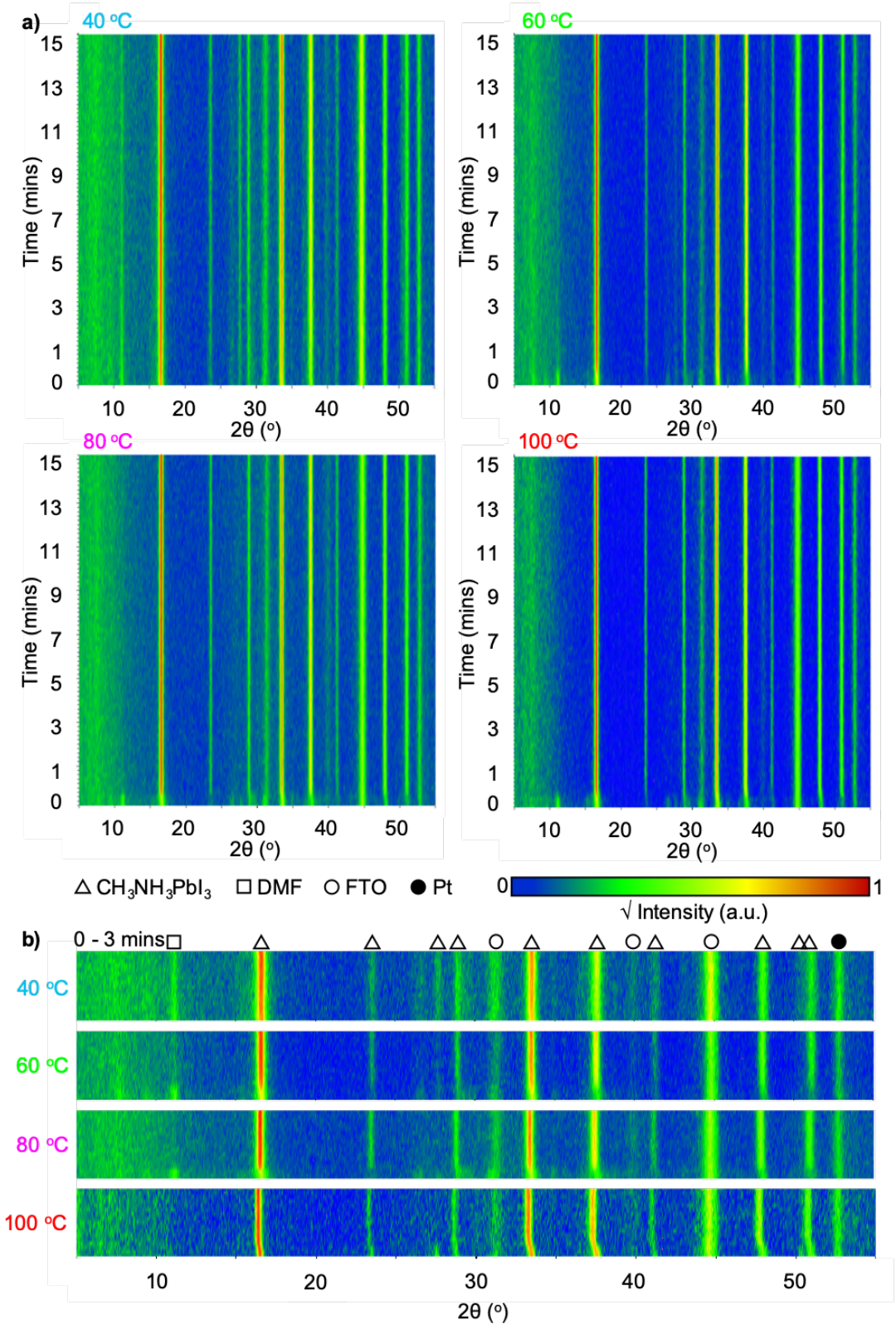

Figure 4.2. (a) X-ray diffraction pattern evolution over time of freshly spin-coated perovskite films, undergoing a crystallisation at 40, 60, 80 and 100 °C. (b) Magnified images of the initial 3 min of the experiment with identified peaks originating from perovskite, N,N-dimethylformamide (DMF) - solvent, FTO-coated glass and the platinum stage. Measurement interval and duration 10.8 s.

The samples were heated and measured for 15 min, which exceeds the standard annealing time of 10 min for this type of perovskite, [198] in order to examine if any structural changes occur when the initial 10 min timeframe is exceeded. However, as seen in the figure, the most prominent changes occur during the first 3 minutes of the experiment.

The diffraction pattern acquired at 40 °C visibly differs from the others, showing additional peaks $2\theta \approx 28°$ and $2\theta \approx 51°$ throughout the entire experiment, which are not visible at higher temperatures. This is attributed to 40 °C being below the tetragonal to cubic phase transition temperature of $MAPbI_3$, which takes place above ~53 °C. [261] Furthermore, the peak $2\theta \approx 11°$ that disappears very fast for higher temperatures remains for the duration of the whole measurement at 40 °C. The origin of this peak will be discussed later in this Chapter.

The first 3 minutes of the measurements were magnified in **Figure 4.2b** to further reveal other differences. With the increase in temperature, the main perovskite peaks $2\theta \approx 16.5°$, $2\theta \approx 33°$ and $2\theta \approx 37°$ become much sharper. Furthermore, the patterns show a shift in the peaks towards lower angles with the increase of the temperature. This is particularly visible in **Figure 4.3**, where the diffraction patterns before (t = 0 min) and after (t = 15 min) the *in situ* measurements are compared to the diffraction pattern of the sample cooled down to the room temperature (t = 17 min). The increase in magnitude of the shift accompanied by the increase of the temperature suggests that the peak shift is related to the change of the perovskite lattice parameters caused by a thermal expansion. The process is reversed as the sample cools down to the room temperature.

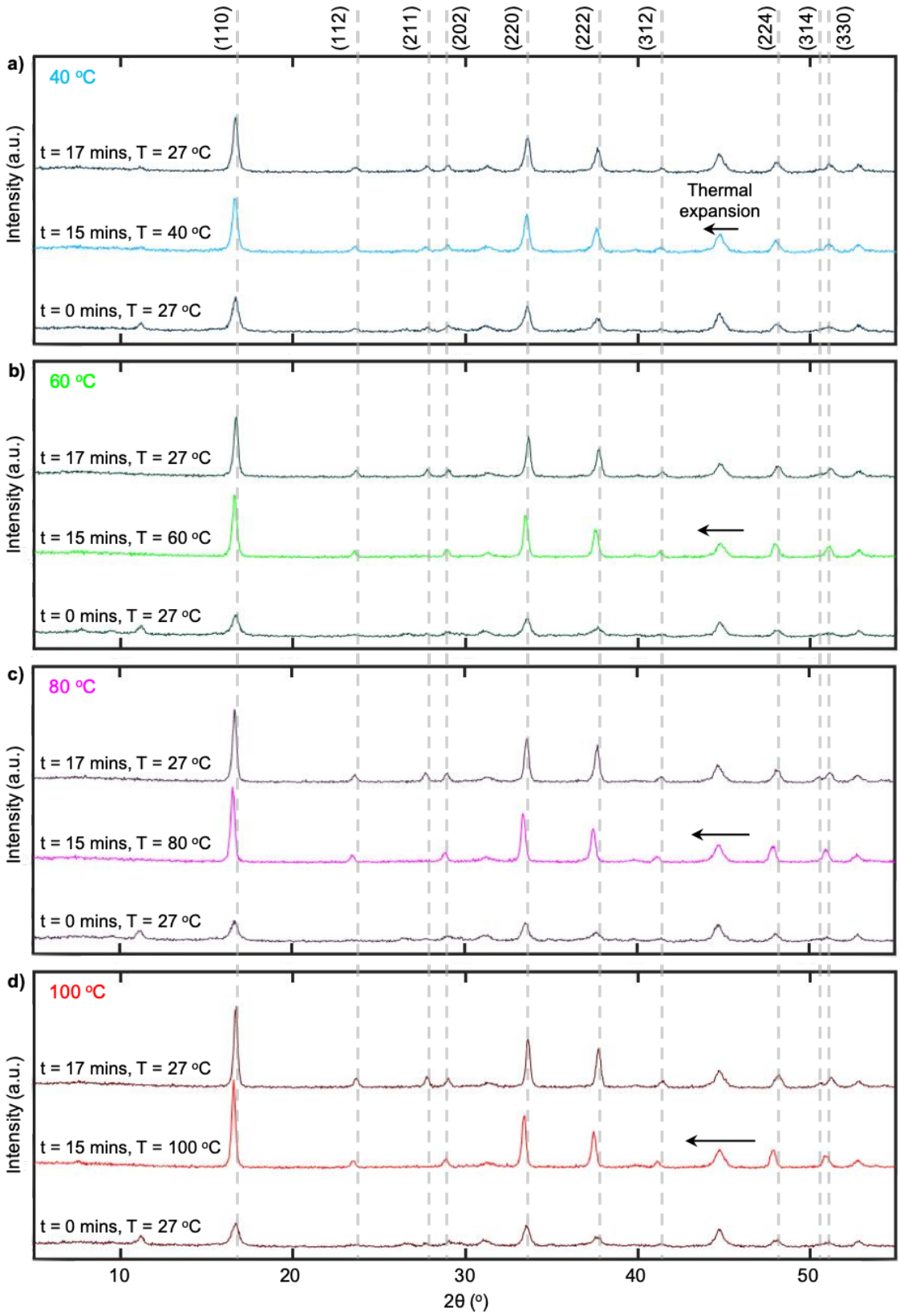

Figure 4.3. XRD diffraction patterns measured before (t = 0 min) and after (t = 15 min) the *in situ* measurements and after cooling to room temperature (t = 17 min). Measurement duration 30 s. Sample crystalized at (a) 40 °C, (b) 60 °C, (c) 80 °C and (d) 100 °C. Identified crystallographic planes of tetragonal lattice of methylammonium lead iodide perovskite.

Figure 4.3 shows the identified crystallographic planes of the tetragonal lattice of methylammonium lead iodide perovskite. As seen in the figure, even at the time of the first measurements (t = 0 min), the main perovskite peaks $2\theta \approx 16.5°$, $2\theta \approx 33°$ and $2\theta \approx 37°$ are visible and become much more prominent over time with the exposure to heat. This indicates that small perovskite crystals are already present in the as-spun coated film. This in in agreement with the SEM analysis of the freshly spun-coated perovskite films performed by Huang *et al*. [198] Furthermore, the peaks $2\theta \approx 28°$ and $2\theta \approx 51°$, which vanished during the *in situ* measurements at 60, 80 and 100 °C, reappeared once the samples were cooled down to the room temperature. This confirms its origin being related to the phase transition of the perovskite lattice.

Interestingly, even a long heating duration of 15 min at the temperature of 40 °C did not cause the peak $2\theta \approx 11°$ to disappear, although its intensity decreases slowly over time. This peak vanished quickly for the samples crystalized at higher temperatures and did not reappear when the crystalized samples were cooled down to room temperature. This may suggest that its origin is related to a complex containing DMF and PbI_2, as published elsewhere, [262], [263] hence, the peak disappears when the solvent is fully evaporated. This was confirmed through the measurement of reference samples. As seen on **Figure 4.4**, the diffraction patterns of pre-annealed samples did not show any peak at $2\theta \approx 11°$ neither before nor after the *in situ* XRD measurement.

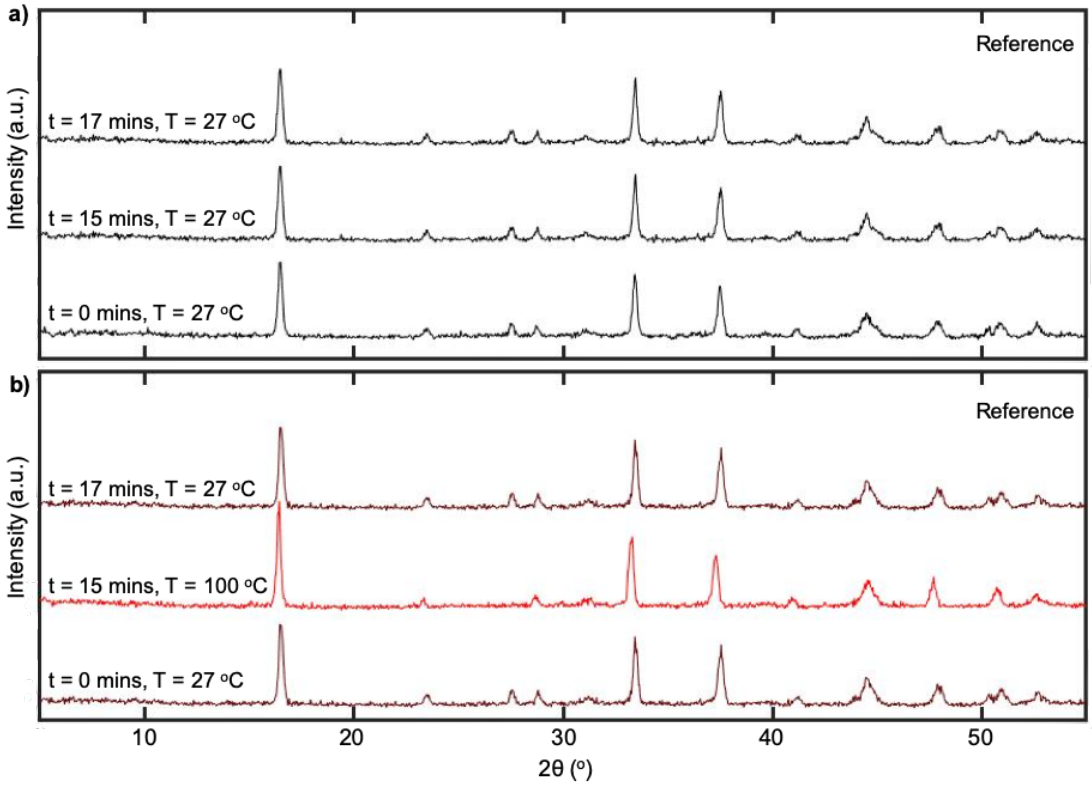

Figure 4.4. XRD diffraction patterns of reference samples kept in the XRD chamber and measured at (a) room temperature and (b) at 100 °C. Scans taken after 0, 15 and 17 min. Measurement duration 30 s.

The *in situ* XRD measurements allows for estimation of the crystal size of the perovskite layer during annealing. **Figure 4.5a** shows the *in situ* changes of the full width at half maximum (FWHM) of the $2\theta \approx 16°$ perovskite peak. In order to extract this data, the peak was fitted to a Gauss profile using MATLAB software. As seen on the graph, all curves follow a similar trend: the width of the peak decreases rapidly during the first few minutes of annealing and then stabilises at the end of the measurement. Additionally, the time needed to reach a plateau decreases with an increase in the annealing temperature. Furthermore, the higher the annealing temperature, the narrower the final XRD peak of the film, indicating a better crystallinity of grains with less defects and/or a larger perovskite crystal size. Using this data, following the equation developed by P. Scherrer, [264] one can calculate an average crystal size (τ) of the perovskite film:

$$\tau = \frac{K\lambda}{\beta \cos\Theta}$$

Where:
K – Crystallite shape factor. Commonly assumed to be 0.9 for random, unpredictable crystals shape [265], [266]
λ – X-ray wavelength (0.17902 nm for CoKα)
β – FWHM
Θ – Bragg angle (0.145 rad for this peak)

The Scherrer equation is a common tool used to estimate the average crystal size of polycrystalline films. The model is the most accurate for crystals with sizes up to 600 nm (for low Bragg angles) with the limit commonly accepted to be 1 μm for higher Bragg angles. [267] The obtained values are way below the limits of this method. The average crystal size over time of the films annealed at 40, 60, 80 and 100 °C was plotted on **Figure 4.5b**.

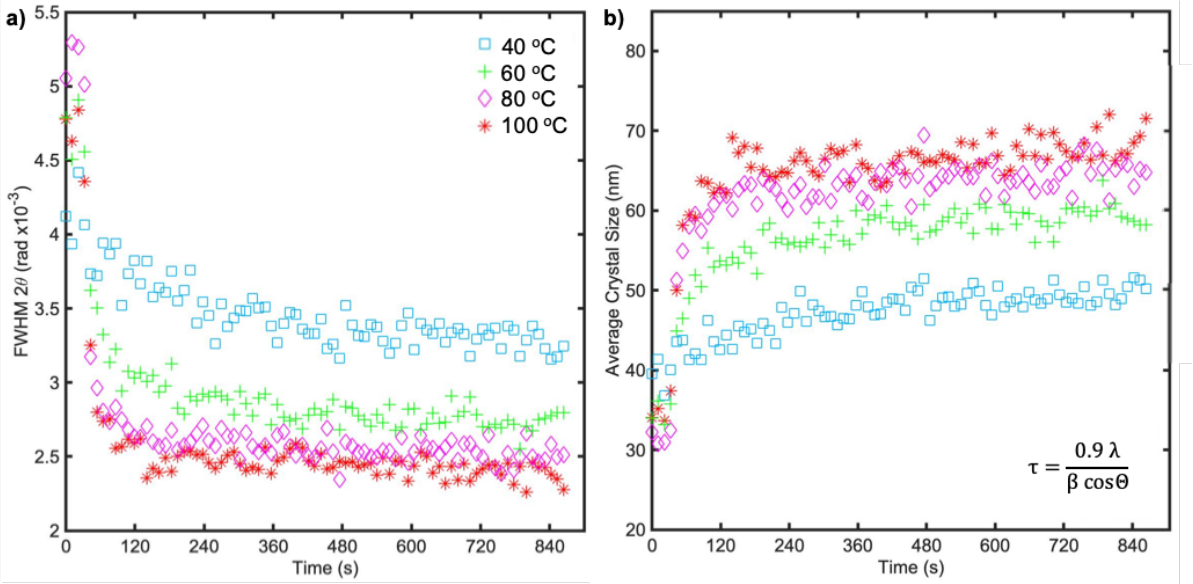

Figure 4.5. (a) Full width at half maximum as a function of annealing time of ~16.5° peak at different temperatures. (b) Average crystal size over time at different temperatures, calculated using the Scherrer formula.

According to the Scherrer model, the average crystal sizes of the perovskite films annealed at 40, 60, 80 and 100 °C for 15 min are roughly 50, 60, 65 and 70 nm, respectively. As expected, the final average crystal size is greater for higher annealing temperature. Interestingly, the graph shows that even really short exposure to a higher temperature results in crystal size that cannot be achieved at 40 °C after a 15 min of heating.

The Scherrer formula is based on many assumptions, such as an infinitely monochromatic X-ray beam, perfect symmetry of the peak and the crystallite shape factor value of 0.9. [264] Furthermore, the FWHM was read from a Gauss function fitting of the peak, which may slightly differ from its real value. Therefore, the presented average crystal size values should be considered to be approximations.

The final grain size of the perovskite film annealed at 40, 60, 80 and 100 °C for 15 min was observed via SEM imaging. In preparation for this experiment, perovskite films were spun-coated on three different types of substrates: a flat stack of TiO_2, Al_2O_3, Al, Ni, NiO_x layers deposited on an FTO-coated glass ("*NiO_x*"), a layer of TiO_2, deposited on an FTO-coated glass ("*TiO_2*") and a quasi-interdigitated back-contact electrode resting on FTO-coated glass ("*QIBC*"), which in fact consists in 50% of *NiO_x* and in 50% of *TiO_2* substrates, in terms of the surface area. The samples were annealed for 15 min. The samples marked as "*NiO_x"* are prepared in exactly the same process as the samples used during the XRD measurement.

As seen in **Figure 4.6** and **Figure 4.7** (with higher magnification), the grain size follows the same trend as the one achieved via the Scherrer equation – the higher the annealing temperature, the bigger the average crystal size. This trend is visible on all three types of substrates. Interestingly, the crystals grown on the *TiO_2* substrate appear bigger than crystals grown on the other two substrates at the same annealing temperature, with the smallest crystals being formed on top of the *QIBC* substrate.

The influence of substrate topography on the perovskite crystal size was already observed by Lin *et al.* [190] During this study, the biggest crystals were obtained on a glass slide, smaller crystals obtained on unpatterned glass/gold substrate and the smallest crystals were obtained on top of gold back-contact electrodes. In the same publication Lin *et al*. observed an improvement in the performance of BC PSCs correlated to the increase in perovskite crystal size. This is caused by the reduced density of GBs, known to cause a charge recombination, thus decreasing the charge-carrier diffusion lengths and consequently the number of collected charges. [268]–[271]

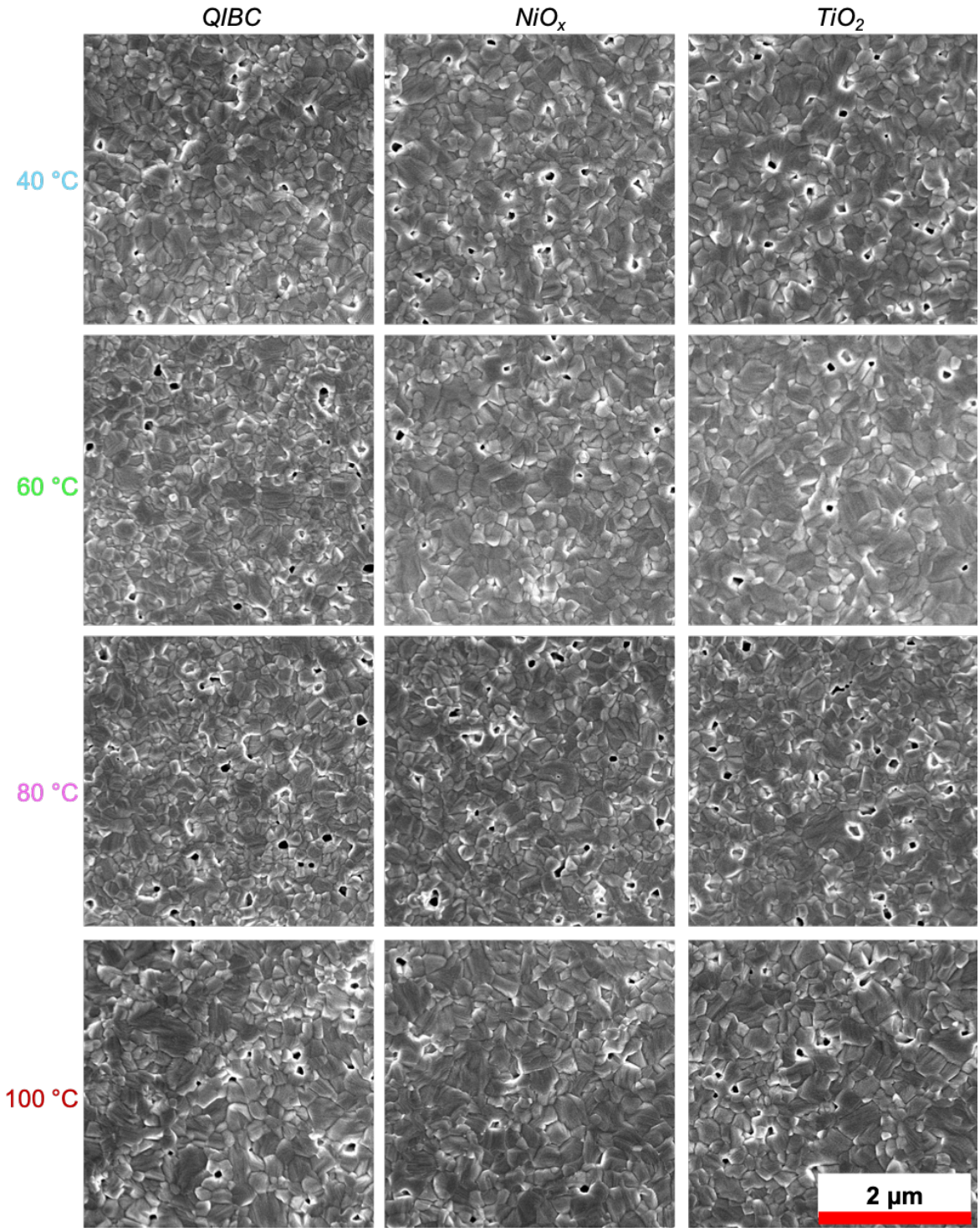

Figure 4.6. Scanning electron microscope images of perovskite films deposited on FTO-coated glass covered with: a quasi-interdigitated back-contact electrode ("*QIBC*"), a flat stack of TiO_2, Al_2O_3, Al, Ni, NiO_x layers ("*NiO_x*") and a layer of TiO_2 ("*TiO_2*"). The samples were annealed at 40, 60, 80 or 100 °C.

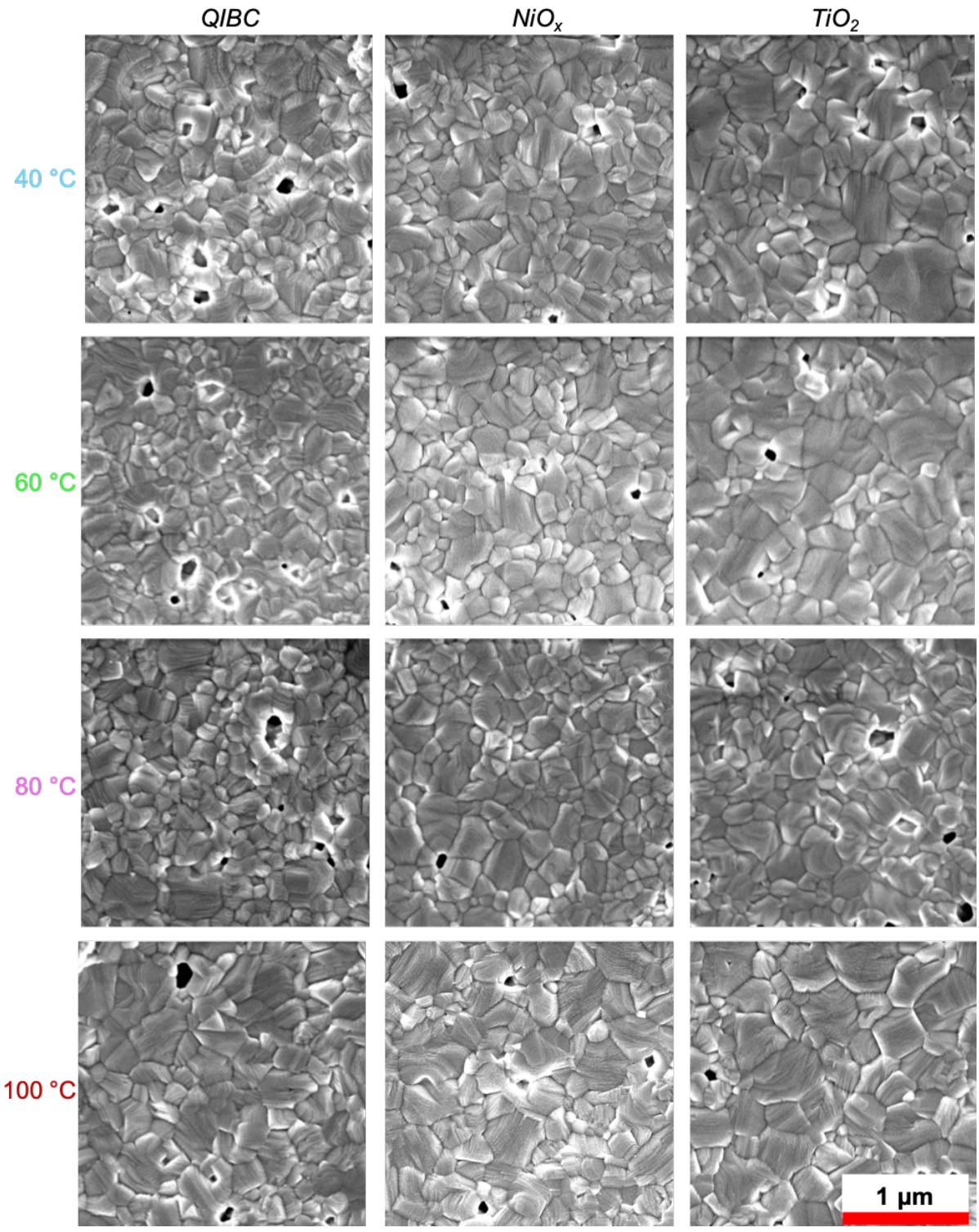

Figure 4.7. Scanning electron microscope images of perovskite films deposited on FTO-coated glass covered with: a quasi-interdigitated back-contact electrode ("*QIBC*"), a flat stack of TiO_2, Al_2O_3, Al, Ni, NiO_x layers ("*NiO_x*") and a layer of TiO_2 ("*TiO_2*"), taken with a higher magnification. The samples were annealed at 40, 60, 80 or 100 °C.

The difference in the morphology of the top surfaces of the *TiO_2* and *NiO_x* substrates is clearly visible in a low magnification SEM image of the QIBC electrode, taken in the secondary electron mode (**Figure 4.8a**). As seen on the figure, the *NiO_x* area appears "brighter" in the

image, hence is much rougher compared to the TiO_2 area. Interestingly, the grain size of the film deposited on this sample appears homogenous over the TiO_2 and NiO_x areas. This is in compliance with results obtained by Lin *et al*. [190]

The average grain size of each film was calculated again using a conventional intercept technique described in the experimental section of this Chapter and used elsewhere. [272], [273] The number of interceptions was obtained from a larger area of the SEM images presented at **Figure 4.6**, in order to achieve a minimum requirement of 50 interceptions per line. The results are presented on **Figure 4.8b**.

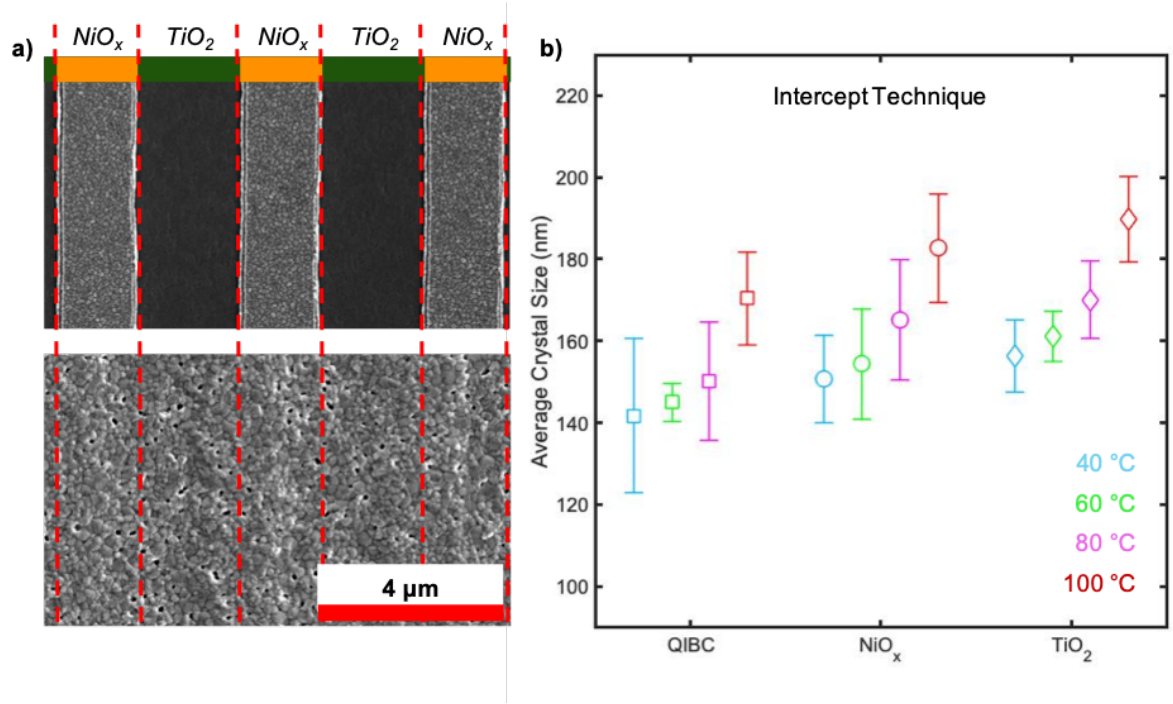

Figure 4.8. (a) SEM image of the QIBC electrode before the perovskite deposition with marked TiO_2 and NiO_x areas. Perovskite film deposited on top of the QIBC electrode. (b) Average crystal size of perovskite film deposited on *QIBC*, TiO_2 and NiO_x substrates and annealed at 40, 60, 80 and 100 °C.

As seen in **Figure 4.8b**, the average grain size of the perovskite film deposited on the NiO_x substrate and annealed at 40, 60, 80 and 100 °C is roughly 150, 155, 165 and 180 nm respectively, with crystal sizes of 50, 60, 65 and 70 nm in plane (110), obtained through Scherrer equation.

The average grain size of the film deposited on QIBC electrodes and annealed at 100 °C (standard deposition procedure) is ~170 nm, which is more than 5 times smaller than a half of the distance between the QIBC electrodes (1000 nm). This implies that the charges created on top of the anode need to be transferred over multiple GBs to reach the cathode (and vice

versa). This increases the probability of charge recombination and is a well-known efficiency limiting factor of BC PSCs. [194], [195]

4.2.3 The evolution of the electronic properties of QIBC PSCs

The evolution of the electronic properties of the perovskite material was examined though *in situ* open circuit voltage, *in situ* short circuit current and *in situ* J-V measurements. During those experiments, samples were annealed at various temperatures and simultaneously measured under illumination by a white LED.

It was discovered that the most significant changes to the electronic parameters are taking place during the first minutes of the annealing. **Figure 4.9a** presents a waterfall diagram of the evolution of open circuit voltage (in arbitrary units) at different temperatures from the moment of the first contact of the sample with the hotplate surface (t = 0 s). In all cases, the initial value of the open circuit voltage is not equal to zero. This was already observed in a similar experiment by Alsari *et al.* [187] and proves a well-defined band gap of the perovskite material is present at the early stages of its formation. Next, the open circuit voltage undergoes a sharp increase. It can be observed that the time needed for the voltage response becomes shorter with an increase in the annealing temperature. This was expected, as the perovskite crystal size increased dramatically in the first few minutes at a greater rate with higher temperatures. Interestingly, almost immediately after the sharp peak, the open circuit voltage decays. For the samples crystallising at a temperature of 60 °C and above, the graphs show a second local extreme followed by another rise. The time difference between those two extremes is inversely proportional to the annealing temperature (**Figure 4.9b**).

Similarly, the short circuit current is showing a delayed response to the annealing, with the decrease of the annealing temperature (**Figure 4.9c**). The short circuit current starts increasing at a similar time as the open circuit voltage, however, unlike the voltage, the initial values of the current are equal to zero. Shortly after the initial increase, the current reaches a temporary plateau, followed by another increase. **Figure 4.9d** shows that the temporary plateau of the short circuit current takes place at a similar time as the second local extreme visible on the open circuit voltage curve.

A visual camera recording of the annealing process of the solar cell shows that the delay in response of the electronics of the solar cell is caused by the solvent evaporation (**Figure 4.9e**) and formation of the perovskite film. A photocurrent is measured when the sample starts turning black (~10 s for 100 °C annealing). At this stage, the absorption increases and the absorbed photons can be converted into current. Visually, the sample reaches a final darkness shortly after (~12 s for 100 °C annealing), however, the continuously rising photocurrent

suggest that the solvent is still present in the crystallising material. This is confirmed by XRD peaks attributed to a PbI_2• DMF complex in the *in situ* XRD measurements, which was observed for ~25 s of annealing at 100 °C, ~35 s of annealing at 80 °C and ~45 s of annealing at 60 °C.

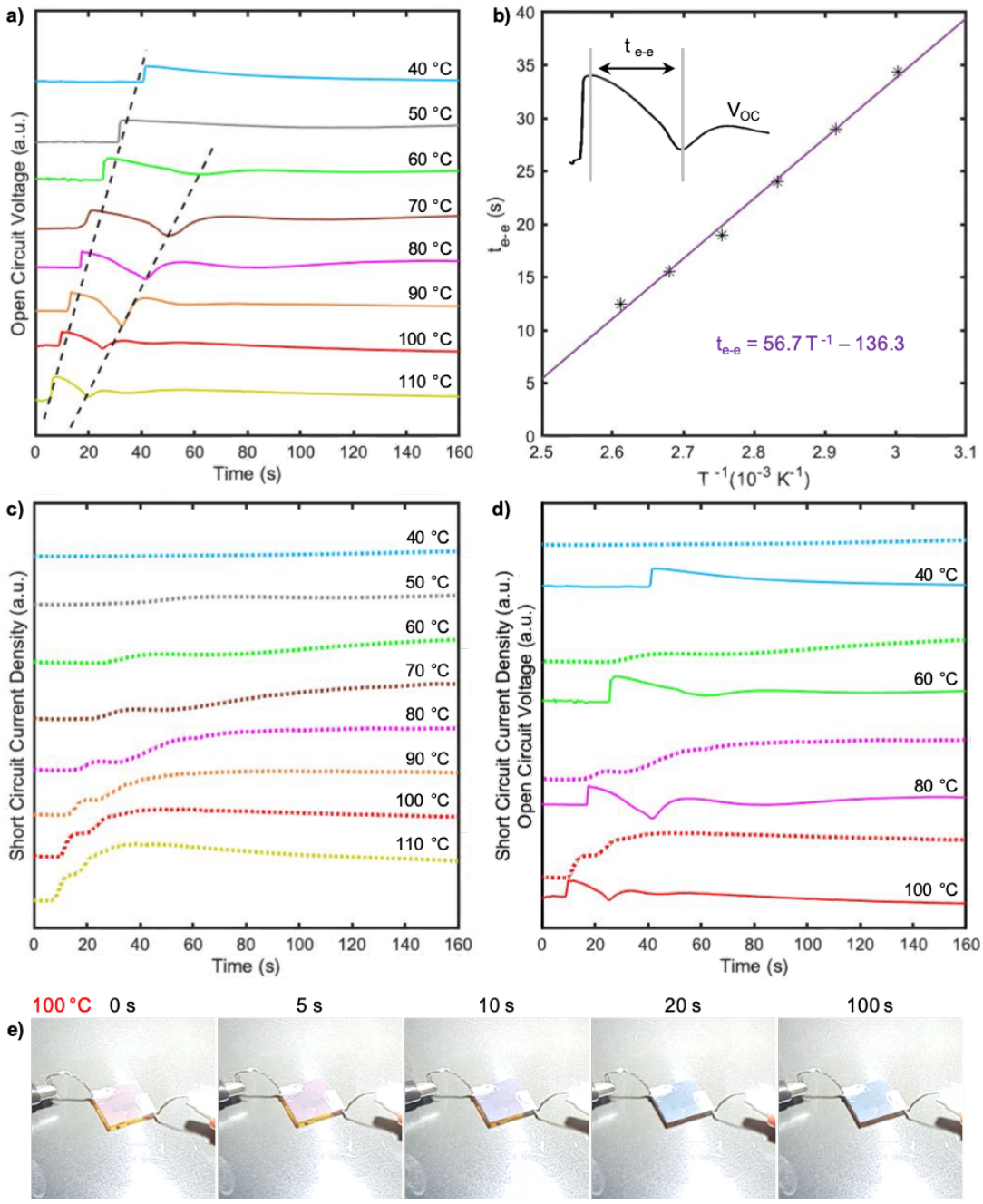

Figure 4.9. (a) *In situ* tracking of an open circuit voltage of solar cells annealed at different temperatures. (b) Time difference between two local extremes present in the open circuit voltage evolution as a function of the inverse of the annealing temperature, showing a lineal trend. (c) *In situ* tracking of a short circuit current of solar cells annealed at different temperatures. (d) *In situ* open circuit voltage (dotted line) and *in situ* short circuit current (solid line) measurements presented on one graph for samples annealed at 40, 60, 80 and 100 °C. (e) Visual camera images of a sample annealed at 100 °C during the film formation process.

The presence of open circuit voltage at t = 0 suggest that the perovskite nanocrystals (visible by XRD) are in contact with the charge selective layers. The crystals are photosensitive, thus can provide holes and electrons to the electrodes, inducing a voltage. However, the lack of current suggests that charges are not extracted by the electrodes at this stage.

The energy provided by the hotplate induces the evaporation of the solvent and the growth of perovskite grains. The initial increase in the open circuit voltage and short circuit current of the solar cell can be explained by the percolation threshold for bulk conductance, showing a long-range conductivity between the perovskite grains forming in the precursor. At that stage, perovskite grains are surrounded by the dielectric solution, which passivates the trap states at the GBs, causing a peak in the open circuit voltage, but most likely, impedance any current. [187], [274]

Next, the growth process of the grains leads to local collisions and crystal defects, which act as hot spots for charge recombination. This causes a decrease in the open circuit voltage and the temporary plateau of the photocurrent. As expected, this process takes place more rapidly with the increasing annealing temperature. Finally, as the grains start aligning, both the current and voltage continue to rise. The short circuit current reaches a maximum when the perovskite phase is fully formed. As shown by the Scherrer analysis (**Figure 4.5**), at this point of time the grain size is approaching its maximum value. This point also corresponds with the time when the open circuit voltage begins to stabilise.

Subsequently, both voltage and current decrease again. This can be clearly observed in **Figure 4.10a**, showing the long-time evolution of the open circuit voltage and the short circuit current of a sample during its annealing at 100 °C. The values are presented in absolute units. The origin of this decrease can be explained by the temperature effects on the charge transport in the perovskite material. In order to confirm this, a reference sample (pre-annealed at 100 °C for 10 min - as per a standard method of deposition) was measured at room temperature and at 100 °C under illumination by the same light source. As seen in **Figure 4.10b** (in black), the short circuit current and the open circuit voltage of the reference sample measured at room temperature does not decay over time. Hence, the changes are not related to light soaking effects or sample degradation. However, once the same sample is placed on a hotplate set to 100 °C **Figure 4.10b** (in red), both voltage and current begin to decrease and stabilise at a lower value to the one measured at room temperature.

Due to the rapid changes in both the short circuit current and open circuit voltage, the *in situ* J-V measurements of the samples were rather challenging. The scan speed was a

limitation of these experiments. The rate at which voltage is swapped during the J-V measurements is a known factor influencing the efficiency of perovskite solar cells. [275]

The *in situ* J-V measurements of a sample during annealing allowed for calculations of a fill factor and determination of efficiency of the samples in reverse and forward directions. **Figure 4.10c** and **Figure 4.10d** show the evolution of those parameters for the sample annealed at 100 °C. Both parameters show a very similar trend – they peak at the beginning of the annealing and begin to decay.

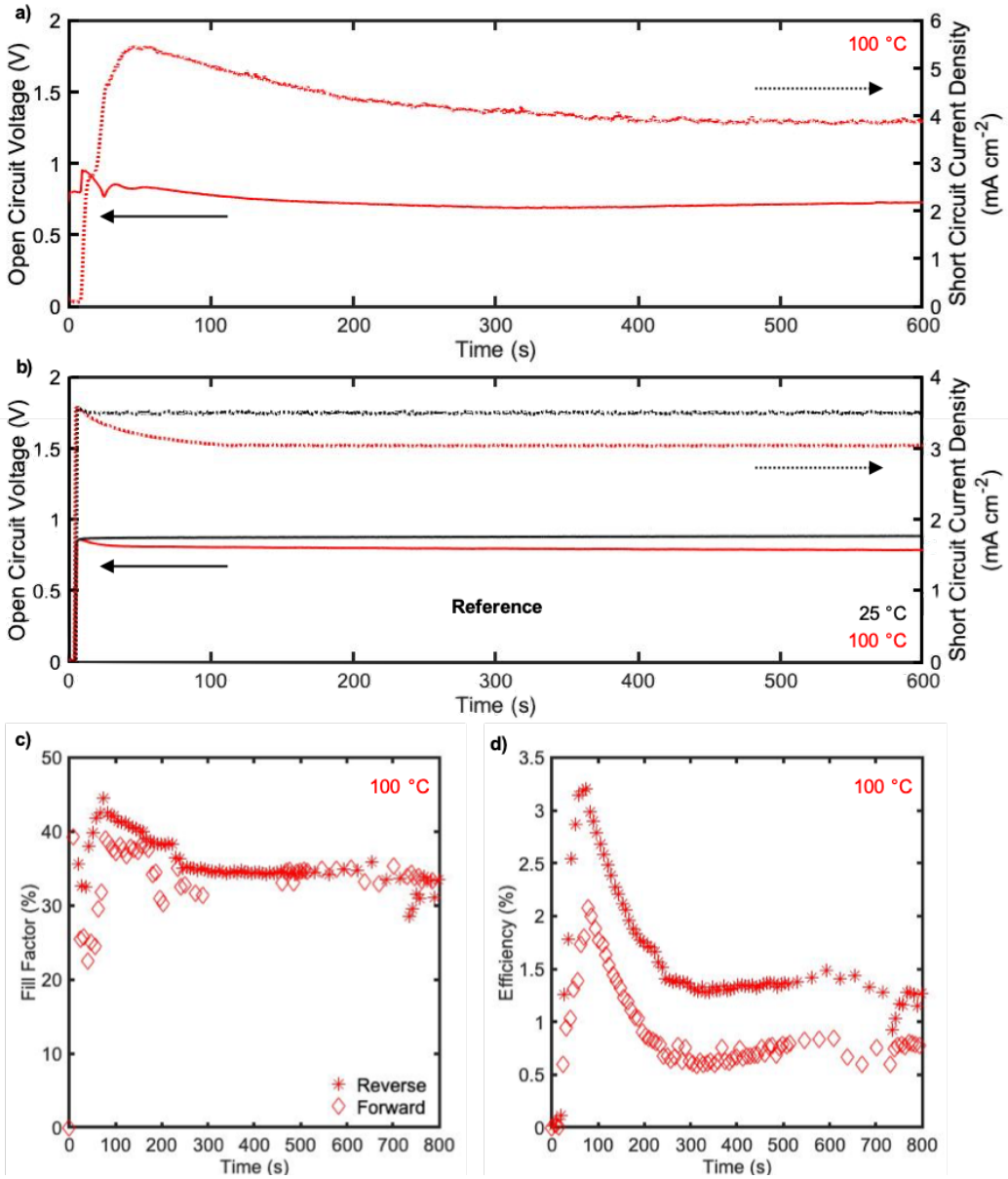

Figure 4.10. (a) The evolution of the open circuit voltage and the short circuit current of a sample annealed at 100 °C measured *in situ* during crystallisation. (b) The evolution of the open circuit voltage and the short circuit current of pre-annealed reference samples. Black – sample measured at room temperature. Red – sample measured at 100 °C. *In situ* measurement of (c) the fill factor and (d) the efficiency of a sample during annealing at 100 °C.

4.2.4 The *in situ* photoluminescence measurements of QIBC PSCs

The evolution of the optoelectronic properties of the QIBC PSCs during annealing was examined through *in situ* photoluminescence measurements. During this experiment the samples were illuminated with a green LED. **Figure 4.11** shows the changes in the photoluminescence intensity of the solar cells annealed at 40, 60, 80 and 100 °C.

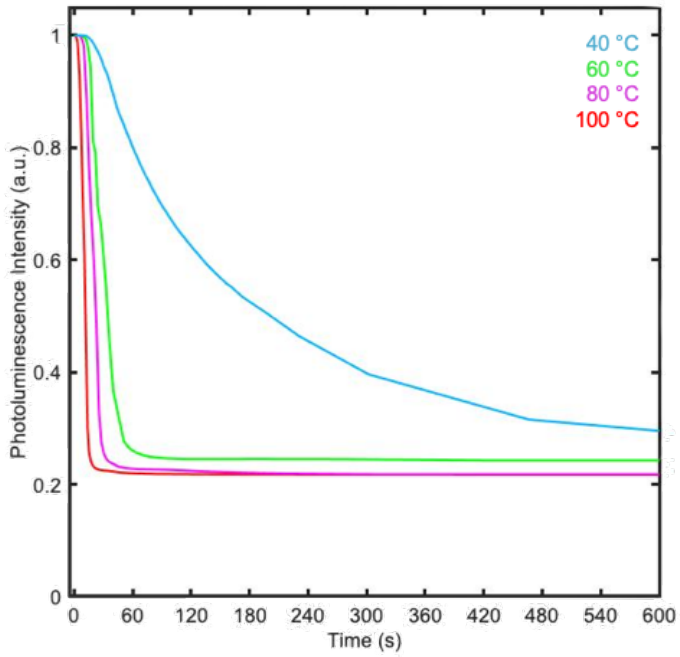

Figure 4.11. The evolution of the photoluminescence signal coming from the perovskite layer resting on QIBC, calculated as an average over the area of the electrode. Samples annealed at 40, 60, 80 and 100 °C

The photoluminescence signal is strongest at the beginning of annealing (t = 0). At this stage, the QIBC electrodes are covered with a precursor solution containing perovskite nanocrystals. The perovskite crystals are photoactive; however, the charge transport is negligible. Hence, all absorbed photons undergo radiative recombination, sending a strong photoluminescence signal.

With the formation of the perovskite film, the photoluminescence intensity decreases significantly. This decrease is faster for higher annealing temperatures. At this stage, the perovskite crystals and grains are forming. The short circuit current tracking shows the appearance of charge transport. The photogenerated electrons are extracted from the perovskite material and the radiative recombination decreases. The differences in the final value of the PL signal may be related to the grain size of the perovskite material crystallising at different temperatures, as described by XRD analysis. Smaller perovskite grains obtained at lower

temperatures cause an increase in the number of the trap states at the GBs and internal crystal imperfections, which facilitate the charge recombination.

Interestingly, the *in situ* photoluminescence curves do not follow the same trends as the corresponding open circuit voltage. This suggests that the second local extreme on the open circuit graph is caused by non-radiative charge recombinations, rather than the radiative ones.

4.2.5 Summary of the results for 100 °C sample. Comparison of the solar simulator measurements of a sample annealed at 100 °C for 1 and 10 minutes.

The *in situ* electronic and optoelectronic measurements, together with the Scherrer analysis of a sample annealed at 100 °C, are presented on **Figure 4.12a-d**. The process of perovskite film formation on top of QIBC electrodes can be divided into five separate stages (S1-S5). **Table 4.1.** provides a summary of all processes, previously described in this Chapter, taking place at each stage of the annealing process.

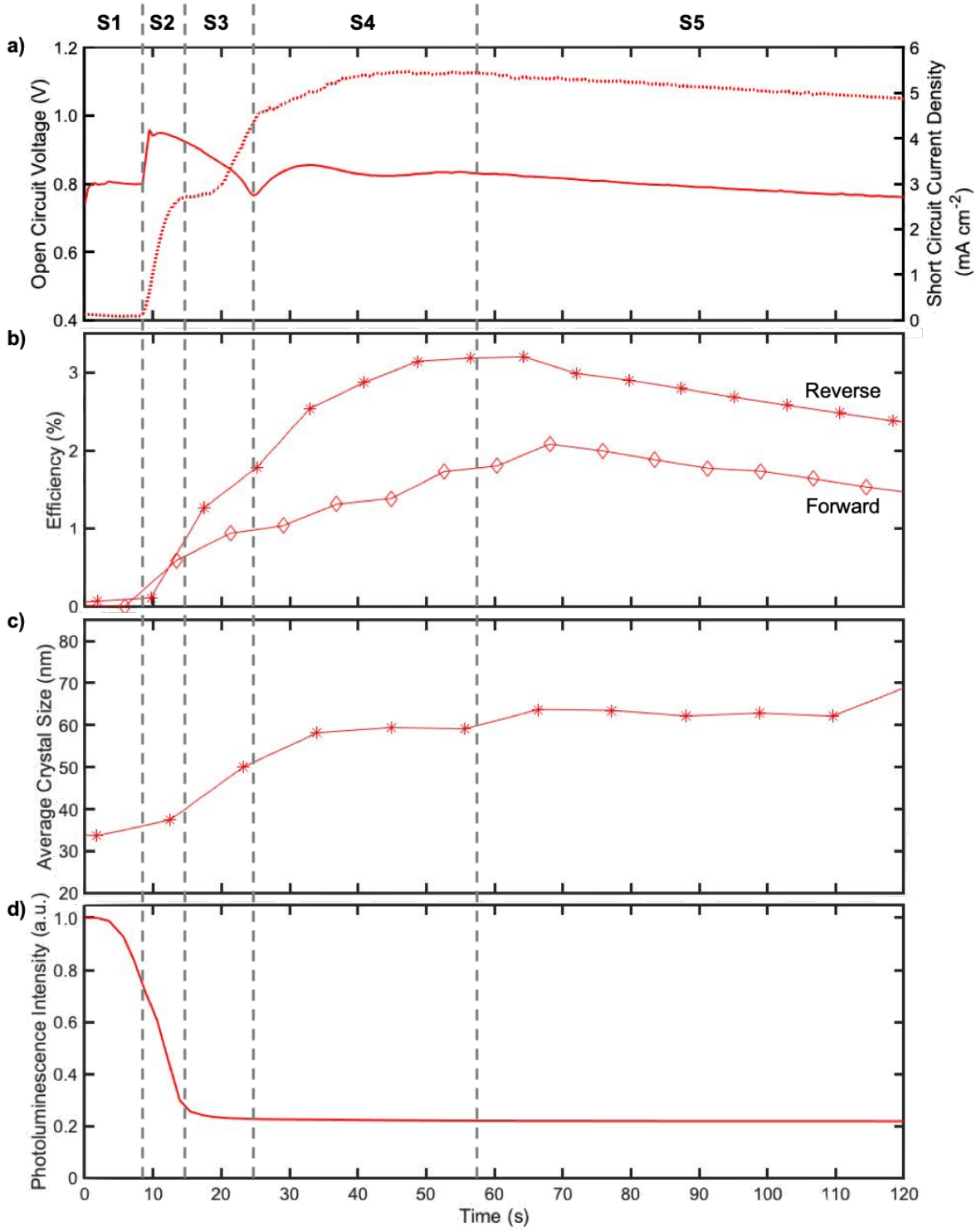

Figure 4.12. (a) *In situ* measurements of a sample annealed at 100 °C: open circuit voltage and short circuit tracking. (b) The evolution of the device efficiency in reverse and forward directions. (c) Average crystal size calculated via Scherrer method. (d) photoluminescence intensity tracking. S1-S5 represent different stages of the perovskite film formation. All graphs have the same time scale.

Table 4.1. The summary of processes taking place at different stages of perovskite film formation.

	S1	S2	S3	S4	S5
V_{OC}	$V_{OC} \neq 0$ Perovskite crystals present. Well-defined band gap of the perovskite	$V_{OC} \uparrow\uparrow$ Increasing rapidly as the crystals grow. Self passivation on grain boundaries	$V_{OC} \downarrow$ Decrease in open circuit voltage caused by local collisions of perovskite grains. Crystal defects act as hot spots for non-radiative charge recombination	V_{OC} stabilising Open circuit voltage is stabilising on a value lower than its maximum value	$V_{OC} \downarrow$ Decrease in open circuit voltage caused by thermal effects
J_{SC}	$J_{SC} = 0$ No charge transport	$J_{SC} = \uparrow\uparrow$ Increasing rapidly as the crystals grow. Solvent evaporation. Charge transport between the electrodes	J_{SC} temporary plateau Photocurrent reaching temporary plateau - local collisions and crystal defects act as hot spots for non-radiative charge recombination	$J_{SC} = \uparrow$ and *S*tabilising Short circuit current is reaching its maximum value	$J_{SC} = \downarrow$ Decrease in short circuit current caused by thermal effects
η	$\eta = 0$ Lack of photocurrent, hence, the efficiency is equal to zero	$\eta = \uparrow\uparrow$ Changes in efficiency are dominated by changes in photocurrent	$\eta = \uparrow\uparrow$ Changes in efficiency are dominated by changes in photocurrent	$\eta = \uparrow$ and stabilising Changes in efficiency are dominated by changes in photocurrent	$\eta = \downarrow$ Decrease in efficiency caused by thermal effects
XRD	$\tau \neq 0$ Small perovskite crystals present at t = 0	$\tau = \uparrow\uparrow$ Perovskite crystals rapidly growing	$\tau = \uparrow\uparrow$ Perovskite crystals rapidly growing	$\tau = \uparrow$ Crystal growth slowing down and stabilising	τ plateau Crystal size reaching plateau
PL	PL = max High photoluminescence intensity. No charge transport causing high radiative recombination	PL $\downarrow\downarrow$ Photoluminescence intensity is decreasing as the charges start getting extracted	PL $\downarrow$ and stabilising Photoluminescence intensity is still slightly decreasing and then decreasing as the charges start getting extracted	PL plateau No visible changes to PL intensity	PL plateau No visible changes to PL intensity

The *in situ* J-V measurements suggest that the efficiency of the device peaks around 1 min of annealing at 100 °C. This contradicts the generally accepted annealing time of 10 min for this type of perovskite. However, the decrease in the device efficiency measured during *in*

situ experiment can be caused by the temperature effects, observed at short circuit current and open circuit voltage measurements. Solar simulator measurements were performed in order to validate this hypothesis. In preparation for this experiment, a set of 10 samples was annealed at 100 °C for 1 min and another set of 10 samples was annealed for 10 min. Samples were then cooled down to room temperature and measured under a solar simulator.

As can be seen on **Figure 4.13**, the difference between the average parameters obtained through those two experiments are within the range of statistical error. The open circuit voltage of the samples annealed for 1 min is slightly higher in both reverse and forward directions. However, the short circuit currents are higher for the samples annealed for 10 min. The efficiencies measured in the reverse and forward directions, as well as the stabilised efficiency, are also slightly higher for the samples annealed for 10 min. The fill factor in reverse direction decreased, and increased in the forward direction with the longer annealing time.

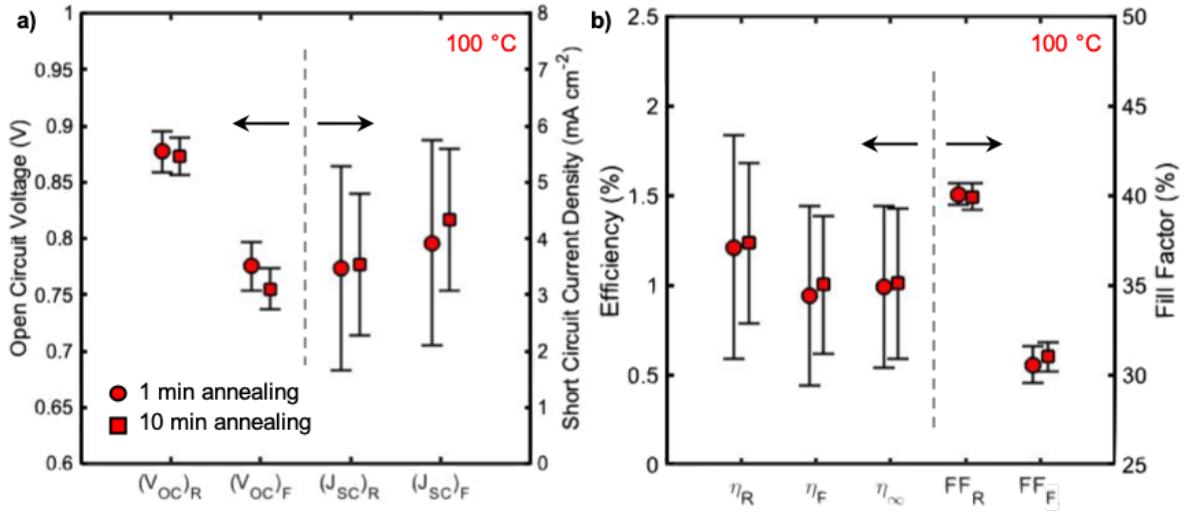

Figure 4.13. Comparison of the batch statistics of samples annealed for 1 minute and for 10 minutes at 100 °C, obtained via sun simulator measurements. (a) Open circuit voltage and short circuit current measured in reverse and forward directions. (b) Photon conversion efficiency measured in reverse and forward directions as well as stabilised efficiency. Fill factor of the J-V curves, obtained in reverse and forward directions.

4.3 Chapter conclusion

In this Chapter, the evolution of the structural, optoelectronic and photovoltaic properties of $MAPbI_3$ perovskite during film formation on QIBC electrodes has been studied through *in situ* measurements. It was discovered that the biggest changes to the aforementioned parameters are taking place during the first few minutes of annealing. Those changes occur faster with the increase in the annealing temperature.

The *in situ* measurements allowed for dividing the annealing process into five Stages. The processes dominating Stages 1-3 were directly correlated to the crystal growth and formation of the perovskite grains. Stage 4 of the annealing occurred when the perovskite crystals achieved the final size. At that time, the QIBC PSCs exhibited a peak of the performance. Stage 5 showed a decrease in the electronic properties of QIBC PSCs. It was discovered that thermal effects were the main factor influencing the device performance during this stage.

The Scherrer analysis of the XRD patterns reveals that the increase of the annealing temperature allows for growing bigger perovskite crystals. Similarly, the SEM images show an increase in the size of the perovskite grains caused by an increase in the annealing temperature. The PL intensity is slightly higher for the samples annealed at lower temperatures. This may be explained by an increase in radiative recombinations at GBs – known hot-spots for charge recombination. The grain boundary density increases with the decrease in the size of the grains, causing an increase in the number of trap states and the probability of charge recombination.

The solar simulator measurements suggest that annealing for 1 and 10 min at 100 °C leads to solar cells of similar efficiency. This result may significantly speed-up the production process of perovskite solar cells at a large scale, and reduce the energy consumed during annealing. However, the large error bars, especially visible on short circuit currents and the efficiencies on **Figure 4.13**, demonstrate the need for improvement in QIBC PSCs technology. Furthermore, the obtained efficiencies cannot compete with the current champion planar solar cell converting 25.2% of incident light into electricity. [84] QIBC PSC technology is a long way from commercialisation. Therefore, the next Chapters of this Thesis will be focused on different methods of improving the efficiency of QIBC PSCs.

Meanwhile, QIBC electrodes remain a useful tool to study the evolution of the properties of the perovskite material. The characterisation methods used in this Chapter can be transferable to different photoactive materials and adopted as a standard technique for the rapid optimization of growth conditions of a photoactive layer.

4.4 Methods and materials

The quasi-interdigitated back-contact electrodes were fabricated via a photolithography method, following the steps described in Chapter 3 of this Thesis. The insulator Al_2O_3 (150 nm) and metals Al (30 nm) and Ni (50 nm) layers were evaporated using an AXXIS e-beam evaporator supplied by Kurt J. Lesker. A photo active material (methylammonium lead iodide, $MAPbI_3$) was deposited according to the gas assisted method, described in the aforementioned

Chapter. The *in situ* measurements presented in this Chapter were performed during the last step of the perovskite deposition – the annealing.

During all of the measurements, apart from the XRD, the samples were annealed on a Heidolph hotplate MR Hei-Connect. The processes were directly following the perovskite deposition and take place in the same nitrogen glovebox. Thermal images of a top surface of the FTO-coated glass were taken every 0.6 s, with an FLIR camera X6540SC and analysed using commercially available software ResearchIR. The measurement was performed in an ambient atmosphere. Samples were not covered with a photoactive layer. X-ray diffraction analysis (XRD) was carried out with Inel XRG-3000 Diffractometer equipped with Co Kα radiation (1.79 Å) in 2θ range from 0 to 117°. Due to the location of the equipment, the first XRD pattern of each sample was measured approximately 10 min after the perovskite deposition. This allowed the time for transportation of the sample to a different laboratory. The samples were carried in a nitrogen filled, sealed box (in order to minimize ambient air exposure) and subsequently transferred to the XRD chamber. The samples were placed on a platinum heating element, warmed at a rate of 110 °C/min to the desired temperature during the first few scans of the measurement. The *in situ* diffraction patterns were collected every 10.8 s for 15 min. Additionally, three 30 s long scans were taken for each sample before (room temperature) and after the *in situ* measurements (hotplate temperature), as well as once the sample was cooled to room temperature. All measurements were carried under a constant nitrogen flow of 10 L/min. Due to the large spot size of the XRD measurements (exceeding the size of a solar cell), the experiment was carried out on FTO-coated glass, covered with unpatterned layers of TiO_2, Al_2O_3, Al, Ni, NiO_x prepared according to a standard evaporation/oxidising procedure described in Chapter 3 of this Thesis. The reference samples were additionally annealed at 100°C for 10 min prior to the XRD measurement.

The photoluminescence images of solar cells were collected using a Nikon Digital Camera D610, equipped with an AF-S MICRO NIKKOR 105 mm 1:2:8GED lens and Kenko MC UV 62 mm digital filter. During this measurement the samples were kept at short circuit current condition. The solar cells were illuminated with green (530 nm) LUXEON Rebel LEDs, controlled by the DC power supply MAISHENG MS305D (**Figure 4.14**). The light intensity was adjusted to 1000 W m^{-2} AM 1.5G and monitored using a secondary reference photodiode

(Hamamatsu S1133, with KG-5 filter, 2.8 × 2.4 mm of photosensitive area), calibrated by a certified reference cell (ISE CalLab PV Cells, certified by Fraunchofer ISE).

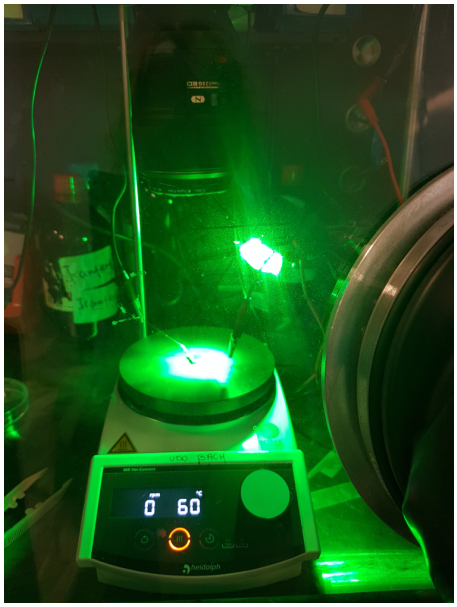

Figure 4.14. Experimental setup for PL measurements. The solar cell is kept at short circuit current condition, simultaneously recorded by the Zahner potentiostat. The sample is illuminated by a green LED while resting on the hotplate. The photoluminescence measurement is taken by a digital camera. The measurements take place directly after spin-coating the photo active layer, inside of a nitrogen filled glovebox, during the film formation.

The *in situ* $J_{SC,}$ V_{OC} and J-V measurements were recorded on a Zahner Electrochemical Workstation ZENNIUM and Thales Z3 software. During those measurements, solar cells were illuminated with a White (5650K) Rebel LED controlled by a MAISHENG MS305D DC power supply. The light intensity was calibrated and monitored using aforementioned reference sample.

The average grain size of the perovskite film was calculated from the SEM images via an intercept technique. This method requires calculating the number of intersections (n_i) between an imaginary straight line with known length (l_i), drawn on top of a SEM image and the GBs of the material (**Figure 4.15**).

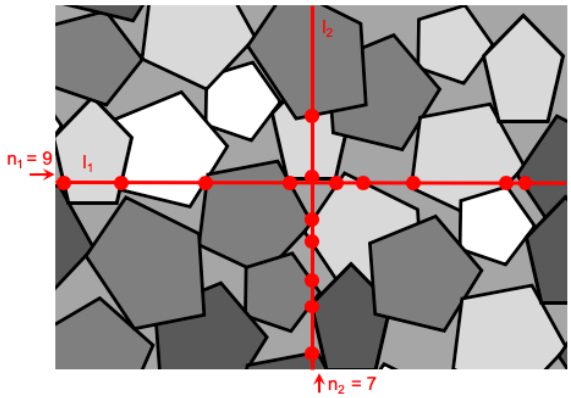

Figure 4.15. Graphic support explaining the method for intercept technique of calculating the average grain size of a material.

The average grain size (d) is then calculated via equation:

$$d = \frac{\sum_{i=1}^{x} \frac{l_i}{n_i}}{x}$$

where x represents a number of the imaginary lines. The measurement was performed using 20 imaginary lines per each SEM image, pointing in random directions to reduce the statistical error. Furthermore, the number of interceptions was calculated from a large area SEM images, in order to achieve a minimum requirement of 50 interceptions per line.

5. *In situ* measurements of back-contact perovskite solar cells during post treatment experiments

5.1 Chapter introduction

As described in Chapter 2 of this Thesis, the passivation of perovskite solar cells is currently an area of intense research in the field. Trap states present at the GBs of the perovskite material and at the interfaces between functional layers foster charge recombination, thus significantly reducing the photovoltaic performance of the solar cells. Scientists employ different strategies to passivate those interfaces, including varying the molar ratio of constituents in the perovskite precursor solution, [215]–[222] adding addition additives, [224], [225] or depositing additional passivating layers at the interfaces. [204], [205], [226], [206]–[212], [223] Another approach commonly used in the field is recrystallisation of the perovskite layer in order to improve the film quality and reduce the number of GBs and thus, the number of defects. [227]–[230] As of today, all those studies were performed on perovskite thin films and planar perovskite devices.

One of the biggest advantages of the BC architecture of PSC is the uncapped perovskite top layer. This structure allows for *in situ* measurements of the photovoltaic performance of the device during post treatment experiments. Choosing the right conditions for passivation of a perovskite layer in the planar structure requires the manufacture of hundreds of devices in order to capture a large batch of statistics. In contrast, the *in situ* measurements of BC PSCs allow for the quick assessment of the right amount of the reacting agent for a given set of conditions for passivation. The results of such experiment can be used to boost the efficiency of BC PSCs, or adapted to the planar structure.

This Chapter presents three examples of *in situ* post treatment experiments on QIBC $MAPbI_3$-based PSCs. A gas exposure pilot plant was created for the purpose of these experiments. The schematic piping and instrumentation diagram is shown in Section 5.4 of this Chapter **(Figure 5.13)** and is referred to on multiple occasions in the results section. In brief, during the experiment, a QIBC PSC sample is placed inside of an exposure chamber filled with nitrogen gas. The chamber is fitted with a quartz window and sealed electronic feedthroughs, enabling photovoltaic measurements of the solar cell during the post treatment processes. Additionally, the chamber is made of a metal with a wall thickness of 2 mm. On few occasions, the chamber was placed on a hot plate to increase the temperature of the sample. This temperature was monitored by a thermocouple.

The experimental setup is fitted with two interconnected gas supply pipes. Nitrogen, an inert gas, is used to carry the vapour of the reacting agent. The setup allows for the regulation of the ratio of the reacting vapour to N_2, thus varying the concentration of the reacting agent

vapour into the inlet of the chamber. This is done in order to slow down the rate of reaction between the perovskite film and the reacting gas and increase control over the experiment. The reactants used in this study were 4-tert-butylpyridine (TBP), 2-amyl pyridine (2AP) and N,N-dimethylformamide (DMF).

5.2 Results and discussion

5.2.1 Passivation of perovskite layer with 4-tert-butylpyridine

Multiple pyridine derivatives were previously reported to have a passivating effect on the perovskite material. [232], [233] Among all of them, TBP is the most commonly used in the PSC field. This is caused by the fact that TBP is usually employed as an additive to Spiro-OMeTAD, a widely used HSL. TBP is known to increase the polarity of Spiro-OMeTAD and improve the contact at the perovskite/HSL interface, leading to higher V_{OC} and PCE of PSCs. [276] Additionally, Habisreutinger *et al.* demonstrated that TBP can serve as a p-dopant for the perovskite layer through a direct chemical interaction between perovskite material. [277]

In order to examine the impact of TBP vapour on a perovskite film, steady-state short circuit current tracking was performed on QIBC PSCs during the gas exposure. Throughout the first experiment, TBP was kept at 130 °C and the total nitrogen stream was run through the evaporation reservoir (F1 = 0 L/min, F2 = 5 L/min, T = 130 °C, V = 1 mL, **Figure 5.13**), the sample was kept at room temperature. The approximate evaporation rate (ER) of TBP was calculated to be 53.5 μL/min.

Such rapid vapour exposure caused a temporary increase in the short circuit current of the device (>36% increase in its initial value) (**Figure 5.1a**), which can be attributed to the perovskite surface passivation and defect reduction. However, upon the constant vapour exposure, the photocurrent began to fall and reached zero after ~27 min. Visual camera images of a different sample undergoing the same vapour treatment were recorded at the beginning of the experiment, and after 450 and 2000 s of TBP vapour exposure (**Figure 5.1b**). Those images show that the complete loss of photocurrent is caused by bleaching of the perovskite material. The mechanism of perovskite corrosion upon exposure to TBP was previously studied. [276]

In order to examine if the corrosion process is reversible, the chamber was placed on another hotplate set to 133 °C. The sample was annealed for 10 min under a constant stream of pure nitrogen (F1 = 5 L/min) and the temperature of the sample (130 °C) was monitored with a thermocouple. Upon such treatment, the sample slowly recovered its colour and was then cooled back to the room temperature. However, the steady-state short circuit current tracking performed after such treatment showed negligible values (**Figure 5.1a,** inset).

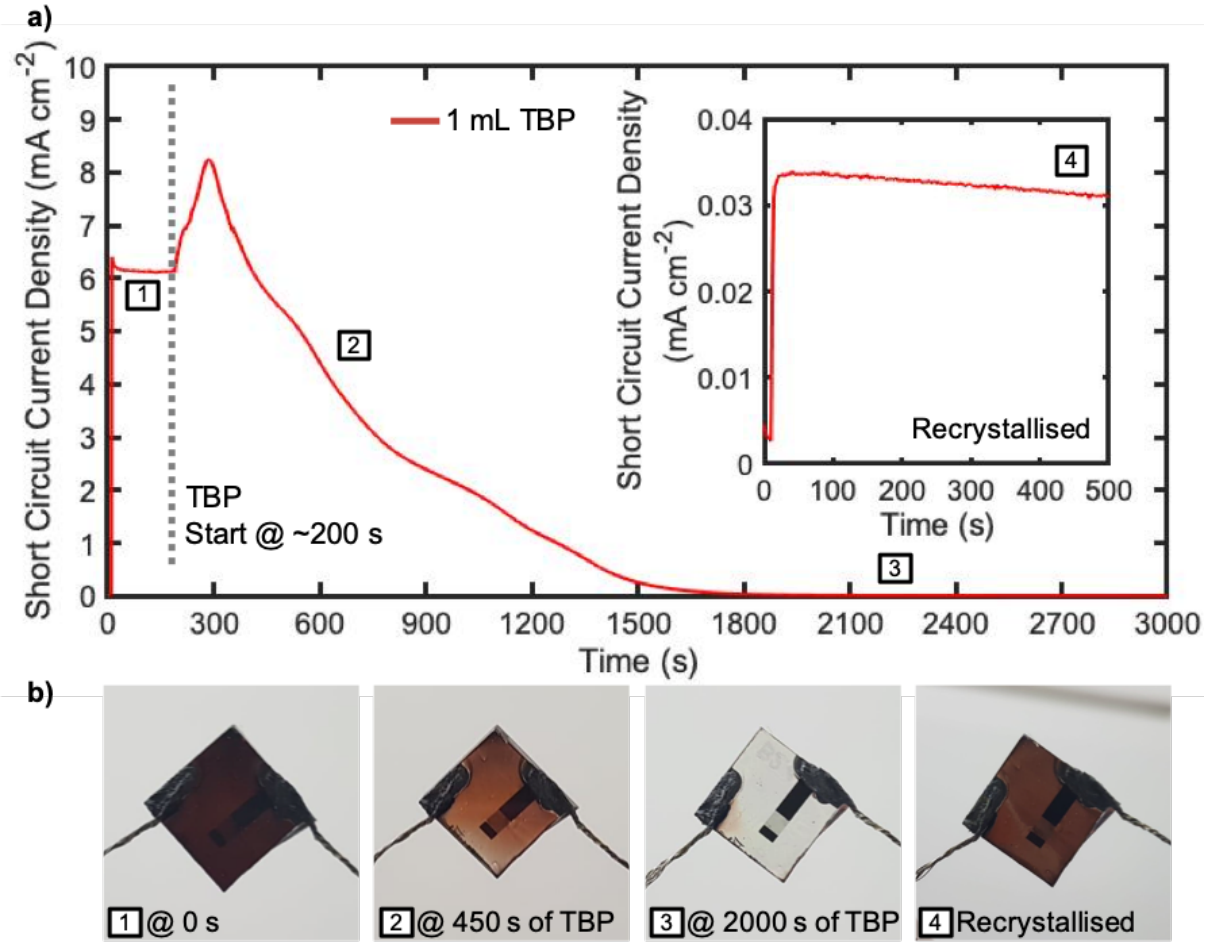

Figure 5.1. (a) *In situ*-measured steady-state short circuit current density of a QIBC PSC during a rapid exposure to TBP. Inset shows results of measurements of the same sample after recrystallisation. (b) Visual camera images of a different sample before and after 450 and 2000 s of TBP vapour exposure at the same conditions, as well as after a recrystallisation.

Despite being rather unsuccessful, this experiment gave a strong indication that reducing the initial volume of TBP and diluting the TBP vapour concentration with nitrogen would slow down the reaction.

The second experiment was performed at F1 = 4 L/min, F2 = 1 L/min, T = 130 °C, V = 150 µL (**Figure 5.13**). The approximate ER of TBP was calculated as 11.8 µL/min, meaning the full volume of TBP was evaporated after ~12.8 min of the gas exposure. **Figure 5.2a** (in green) shows an evolution of the photogenerated short circuit current of the device. The graph was shifted down by 2 mA cm^{-2} to improve the clarity of the figure. This strategy was used on multiple occasions in this Chapter.

The photogenerated short circuit current of this sample rose much slower than in the previous experiment and after approximately 8 min reached a temporary plateau. Next, the ongoing exposure to the TBP vapour initiated the process of perovskite corrosion (as indicated by the decrease of photogenerated current), which continued even after the TBP was fully

evaporated. This may have been caused by residual TBP vapour in the pipes and the chamber. The final short circuit current stabilised at ~85% of its initial value.

This experiment was repeated with a fresh sample. However, the flow of TBP/N_2 gas mixture was cut off at approximately the same time as the previous sample reached a plateau. From that moment, the chamber was purged with pure nitrogen (F1 = 5 L/min, F2 = 0 L/min). **Figure 5.2a** (in blue) shows that initially the short circuit current was following the same trend as in the previous experiment. However, after the TBP/N_2 gas was cut off, the current slightly decreased and eventually stabilised at a value 12% of its initial one. Assuming the same ER, the evaporated volume of TBP at that moment was approximately 100 μL.

Next, both experiments were repeated, however, this time, the program was tracking the open circuit voltage of the solar cells (**Figure 5.2b**). The results show that open circuit voltages followed similar trends. For the sample exposed to 150 μL: an initial increase, followed by a decrease caused by an overexposure and eventually, a stabilisation at a value ~5% lower that the initial V_{OC}. For the sample exposed to 100 μL: an initial increase, followed by stabilisation at a value ~4% higher that the initial V_{OC}. Those results were also confirmed by J-V characteristics of the same solar cells before and after the exposure to 150 μL (**Figure 5.2c**) and 100 μL (**Figure 5.2d**) of TBP. Upon exposure to 150 μL of TBP, the efficiency of QIBC PSC decreased by ~31% in reverse and by ~26% in forward directions. This change was accompanied by a decrease in fill factor of the J-V characteristic by ~14% and ~7% in reverse and forward directions, respectively. On the other hand, the exposure to 100 μL of TBP brought a significant increase in device's efficiencies (~34% in reverse, ~46% in forward directions) as well as in the fill factors (~10% in reverse, ~6% in forward directions).

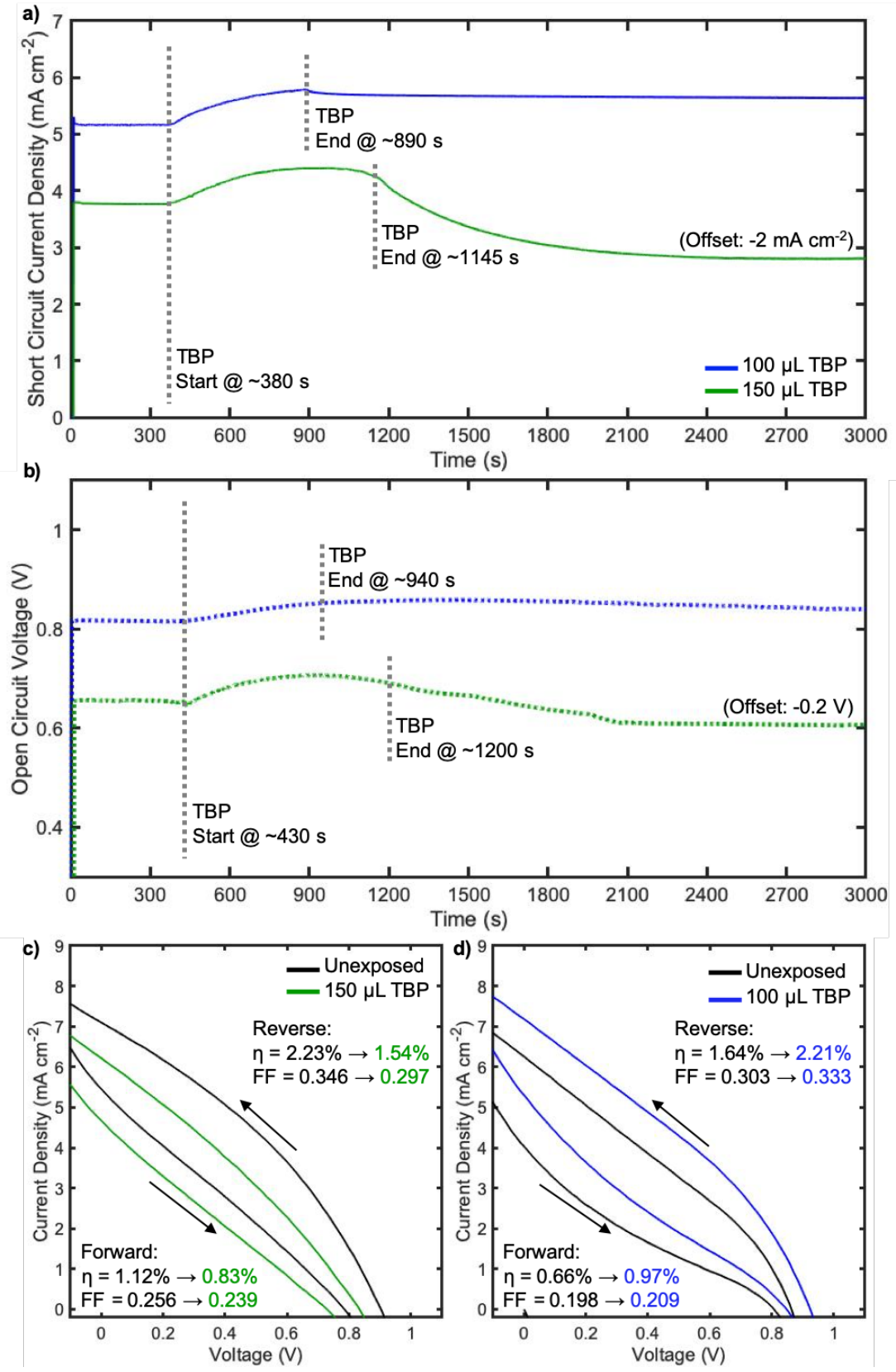

Figure 5.2. (a) *In situ*-measured steady-state short circuit current density of QIBC PSCs during an exposure to 150 µL and 100 µL TBP. (b) *In situ*-measured open circuit voltage of QIBC PSCs during an exposure to 150 µL and 100 µL TBP. J-V characteristics of QIBC PSCs before and after the exposure to (c) 150 µL and (d) 100 µL.

A photoluminescence (PL) study was performed in order to validate the passivation effect of TBP on the perovskite layer. During this experiment, the sample was illuminated by a green LED. The PL measurement was taken by a visual camera equipped with an IR filter. Due to the small size of the QIBC sample (0.04 cm^2), and the insufficient resolution of the PL camera, this experiment was performed on a planar perovskite film, deposited on glass/FTO/TiO_2 substrate (area: 1.5 cm^2). The PL intensity was extracted from the images and calculated as an average pixel intensity over an area defined in the centre of the sample (0.5 cm^2).

Figure 5.3 shows the evolution of the PL intensity of the samples during the exposure to 150 and 100 µL of TBP. The introduction of the reactant to the chamber caused a gradual increase in the PL intensity for both samples, confirming the passivation effect of TBP on the surface trap states of the perovskite. The corrosion process of the sample exposed to 150 µL caused a significant and rapid decrease of PL. The final PL intensity of this sample eventually stabilised at a value ~10% lower than the initial signal. In contrast, the PL signal of the sample exposed to 100 µL stabilised at a value ~13% percent higher than the initial one and stayed fairly constant throughout the rest of the experiment.

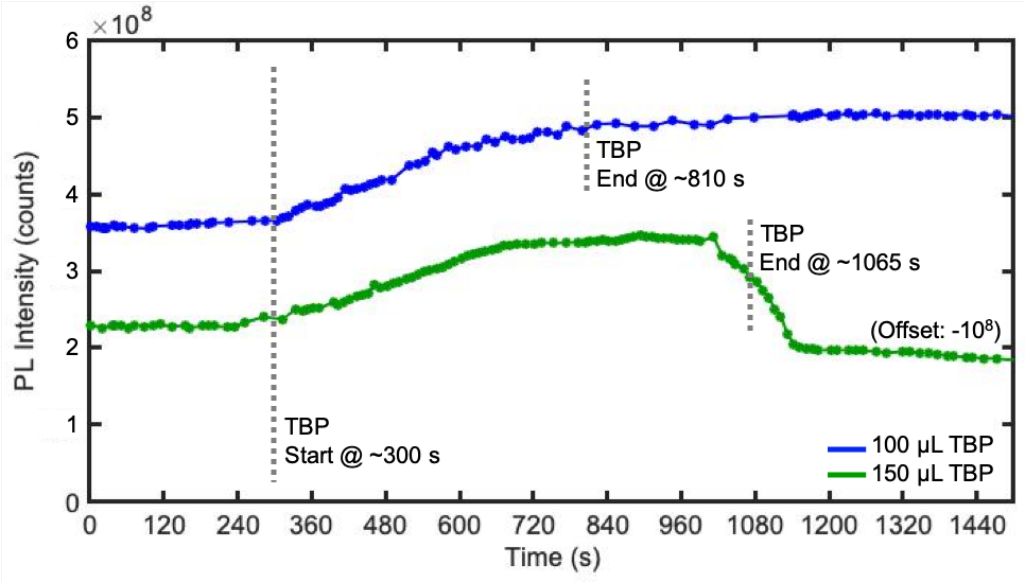

Figure 5.3. The evolution of photoluminescence intensity of planar Glass/FTO/TiO_2/$MAPbI_3$ samples during TBP vapour exposure.

Suns-V_{OC} is a common method used in the field of solar cells that allows for the assessment of their quality and the dominant recombinations taking place in the device. During such experiments, a V_{OC} of a solar cell is measured at different sun intensities. This experiment

was performed on a QIBC PSC before and after an exposure to 100 μL of TBP. Using a diode equation of a non-ideal solar cell, one can calculate an ideality factor (*n*) of a solar cell:

$$I = I_s(e^{eV/nkT} - 1)$$

Where:
I - photocurrent
I_s - dark saturation current
V - voltage applied across the solar cell
e - electron charge
k - Boltzmann's constant
T - absolute temperature (K)
n - ideality factor

At V_{OC} condition $V=V_{OC}$, $I=0$

$$I = I_s e^{eV_{OC}/nkT} - I_s$$

$$\frac{I}{I_s} = e^{eV_{OC}/nkT}$$

$$\ln\left(\frac{I}{I_s}\right) = \frac{eV_{OC}}{nkT}$$

$$n = \frac{eV_{OC}}{kT \ln\left(\frac{I}{I_s}\right)} \approx \frac{eV_{OC}}{kT \ln(I)}$$

Hence, the ideality factor can be read as a slope of the linear fit presented at **Figure 5.4**. An ideal single junction p-n diode would have an ideality factor equal to 1. As a general rule, higher values of the ideality factor can be interpreted as a decrease in the quality of the solar cell. A theoretical study performed by Tress *et al.* [278] on planar perovskite devices suggests that for PSCs with *n* of values between 1 and 2, the charge recombinations taking place in the bulk of the material and are mainly radiative (band-to-band), whereas, for $n \geq 2$ the non-radiative Shockley-Read-Hall (trap-assisted) recombinations at depletion region are dominant.

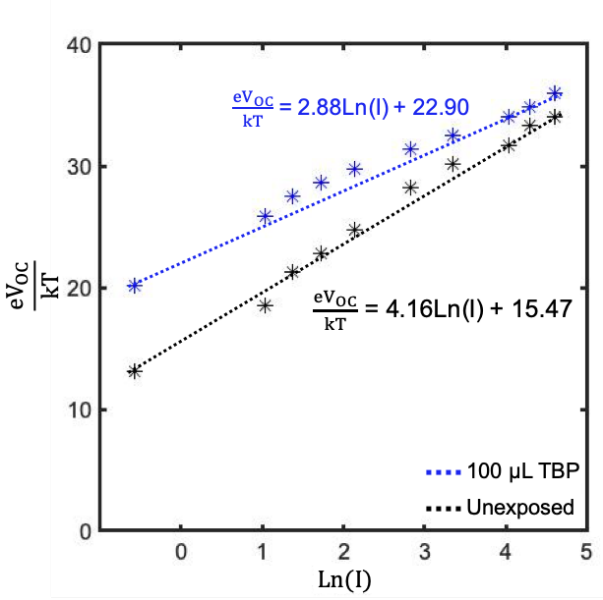

Figure 5.4. Results of the suns-V_{OC} experiment on QIBC PSC before and after an exposure to 100 µL of TBP.

The initial ideality factor of the QIBC PSC was very high (n = 4.16), suggesting the dominance of non-radiative recombination. The experiment shows that upon exposure to 100 µL of TBP, the ideality factor decreases significantly (n = 2.88). However, according to Tress's study, the non-radiative recombinations are still dominant. Those recombinations may come from the non-passivated interfaces in the QIBC device between the functional layers and at perovskite GBs. During the TBP vapour exposure, only the top surface of the perovskite material undergoes the passivation.

An SEM investigation of the QIBC PSCs was performed in order to examine if the morphology of the perovskite material is impacted by the TBP vapour treatment (**Figure 5.5**). The images show that the exposure of the perovskite to 100 µL of TBP does not induce any noticeable changes at the surface. However, perovskite GBs become blurry for samples exposed to 150 µL of TBP, and small features become clearly visible at the perovskite surface. Those features are still present after the recrystallization of the sample. Additionally, multiple cracks can be observed at the GBs of the recrystallised perovskite. Those cracks are likely to impede the electrical connection between the grains, which could explain the negligible photocurrent measured for this sample.

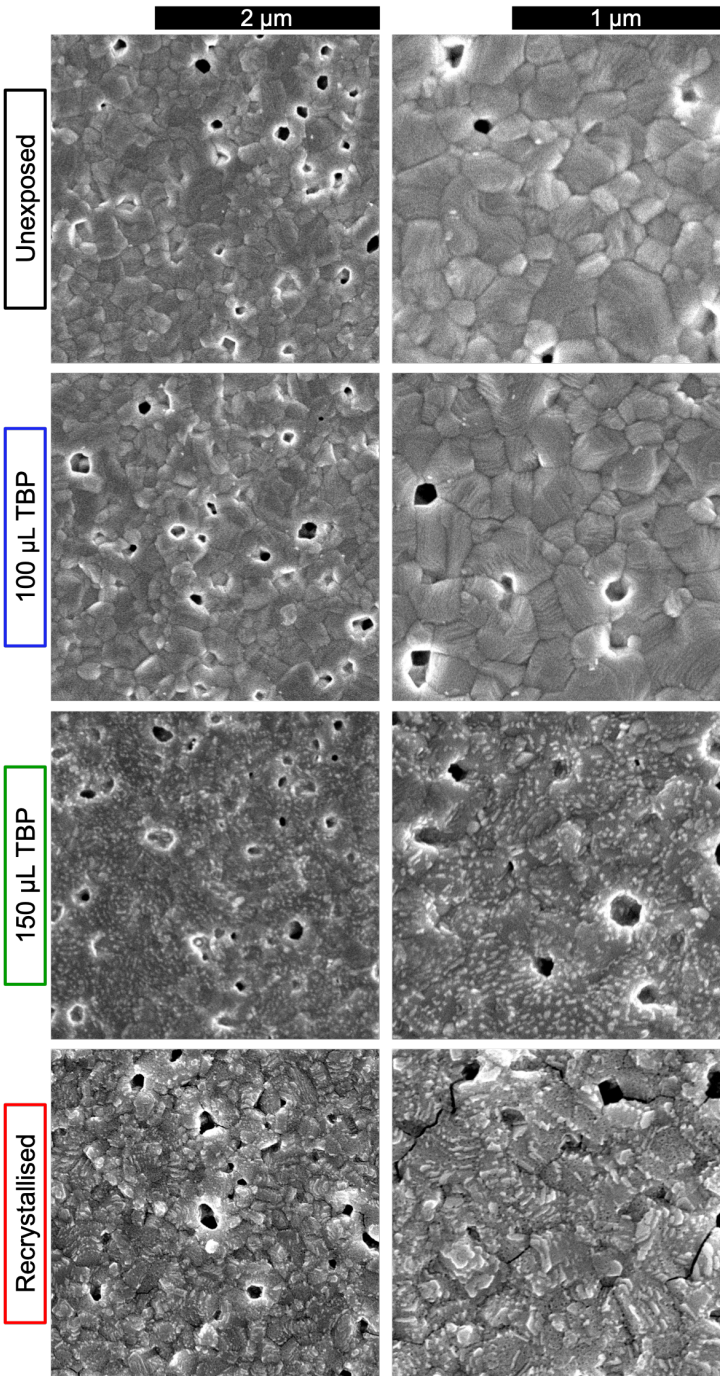

Figure 5.5. SEM images of QIBC PSCs before and after the exposure to 100 µL, 150 µL and 1 mL of TBP (last sample was annealed at 130 °C for 10 min to recrystalise perovskite material pror to SEM imaging).

As a next step, the samples were measured with a UV-vis spectrometer (**Figure 5.6**). Similarly to PL, QIBC electrodes were too small to obtain the spectra with sufficient accuracy, hence, this experiment was performed on planar perovskite films, deposited on Glass/FTO. The rapid exposure to TBP, followed by the recrystalisation brought an increase in the transmission of the sample, also visible at the visual image of recrystalised QIBC PSC in

Figure 5.1b. The decrease in the absorption was another factor contributing to the loss of photogenerated current of the recrystallised sample. It is worth noting that experiments with longer annealing times (30 min) were also performed in the course of collecting data for this Chapter to examine if the pervoskite film was fully recrystalised. However, after longer annealing, the measured photocurrents only decreased.

The absorption, transmission and reflection spectra of the 150 µL and 100 µL TBP-exposed samples differ only slightly from each other and from the unexposed sample. The differences are negligable (< 2%) and lie in the experimental error of the equipment or in the mounting of the samples. They may be also caused by a slight difference in the film thicknesses.

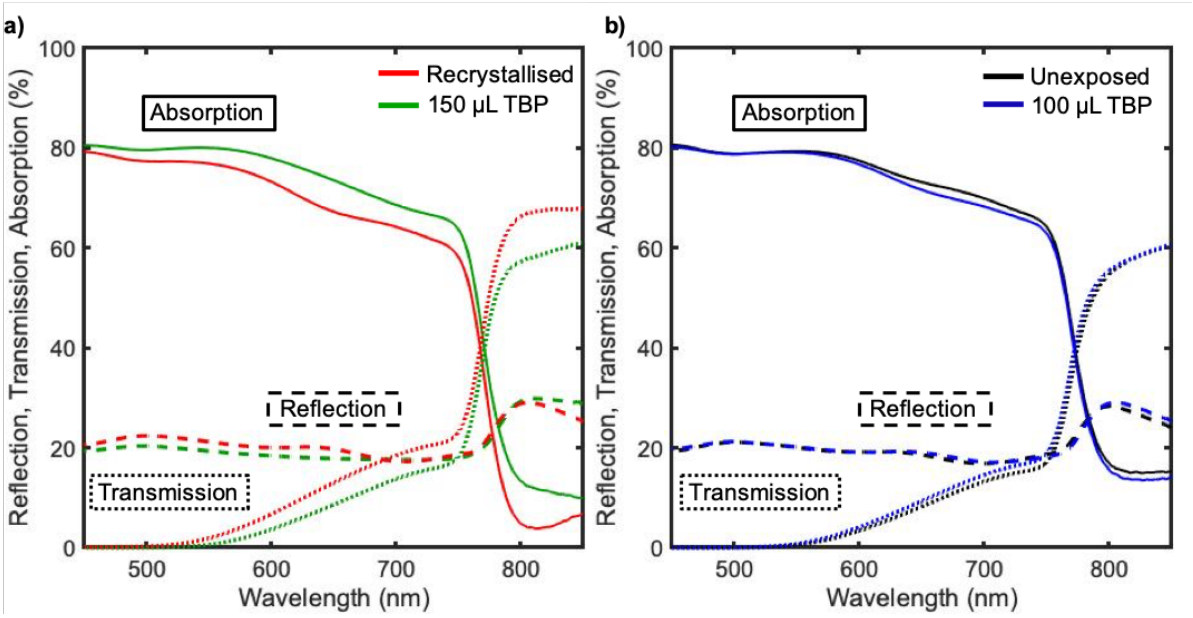

Figure 5.6. UV-vis transmission, reflection and absorption spectra of perovskite films deposited on Glass/FTO. Films exposed to (a) 1 mL of TBP, 150 µL of TBP, (b) 100 µL of TBP and unexposed sample.

Next, an XRD measurement was performed on an unexposed QIBC PSC, as well as on samples exposed to 100 µL, 150 µL and 1 mL of TBP (recrystalised). The diffraction patterns of the samples show no noticeable difference upon exposure to 100 µL of TBP in comparison to the unexposed sample. However, the pattern collected for the sample exposed to 150 µL of TBP shows an additional peak at $2\theta \approx 8°$. This peak was also observed by Yue *et al.* upon exposure to TBP and was attributed to the formation of a complex between PbI_2 and TBP at the perovskite surface, thus, the corrosion of a perovskite material. [233] This peak became even more prominent for the sample exposed to 1 mL of TBP. Additionally, the recrystalised

sample showed a small peak at 2θ ≈ 11°, which is usually attributed to PbI_2 and caused by the chemical decomposition of the perovskite material.

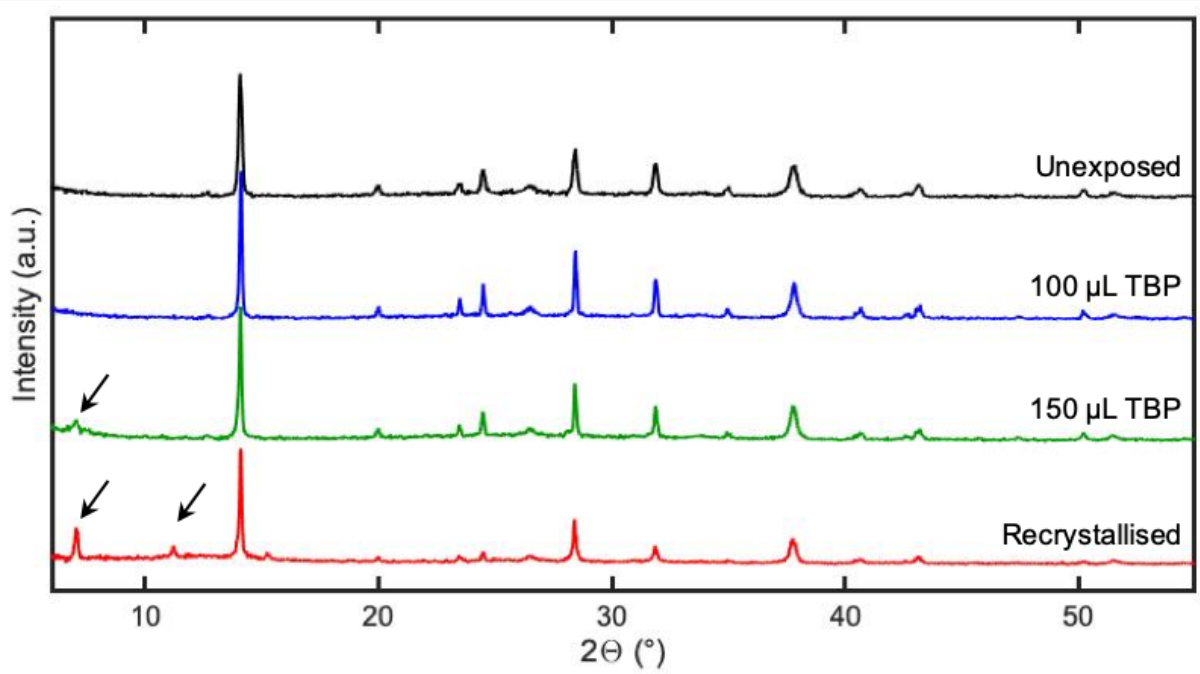

Figure 5.7. XRD diffraction patters of the unexposed sample, as well as samples exposed to 100 µL, 150 µL and 1 ml of TBP (recrystalised). Arrows at 2θ ≈ 8° indicate the corrosion of perovskite. Arrow at 2θ ≈ 11° show a rise of PbI_2 peak.

5.2.2 Passivation of perovskite layer with 2-amyl pyridine

The next post treatment experiment was performed with 2AP, previously used as a passivator in planar PSCs. As in the experiments with TBP, a QIBC PSC was first rapidly exposed to 1 mL of 2AP (F1 = 0 L/min, F2 = 5 L/min, T = 80 °C, V = 1 mL, **Figure 5.13**) and a steady-state short circuit current measurement was performed (**Figure 5.8a**). A rapid rise of the photocurrent was observed when the 2AP vapour was introduced to the chamber. This increase can be attributed to the passivation of the trap states at the surface of perovskite. However, this time, a prolonged exposure to the passivator did not bring any further changes and the photocurrent remained constant until the end of the experiment. After the treatment, the short circuit current of the QIBC PSC stabilised at a value 19% higher than the initial one. The approximate evaporation rate of 2AP in this experiment was calculated to be 23.9 µL/min, meaning that the total introduced volume of 2AP evaporated after roughly 42 min of the experiment.

Over the course of the data collection, it was discovered that complete passivation can be achieved by exposing the sample to a volume of 2AP as low as 30 µL. This process was

slowed down by diluting the vapour with nitrogen (F1 = 4 L/min, F2 = 1 L/min, T = 80 °C, V = 30 μL, **Figure 5.13**), and the approximate evaporation rate of 2AP in this experiment was calculated as 5.6 μL/min. The steady-state short circuit current and open circuit tracking measurement results of such an experiment are presented at **Figure 5.8b**. The results show that upon the passivation, the photogenerated current increased by ~21% (slightly higher than in the previous experiment). However, because of the gas dilution with nitrogen, the passivation took place much slower, thus, the gradient of the current density slope is less steep. Additionally, the open circuit voltage increased by 16% versus the initial value, which confirms the passivation of the trap states at the surface of perovskite.

J-V characteristics (**Figure 5.8c**), measured before and after the exposure to 30 μL of 2AP show a significant enhancement in PCE of the device (23% in the reverse and 11% in the forward direction). Both the short circuit current and the open circuit voltage increased after the treatment. Interestingly, a slight drop in FF of the device was observed after this exposure (1% in the reverse and 9% in the forward directions). An origin of this FF decrease should be a subject to further investigation in the future work.

The suns-V_{OC} measurement reaffirms the passivating effect of 2AP on QIBC PSC. Upon the exposure to 30 μL of 2AP, the ideality factor of the solar cell decreased from 3.48 to 2.58 (**Figure 5.8d**). According to Tress's study, discussed in the previous paragraph, the non-radiative recombinations are still dominating in the device, however, its number significantly reduced.

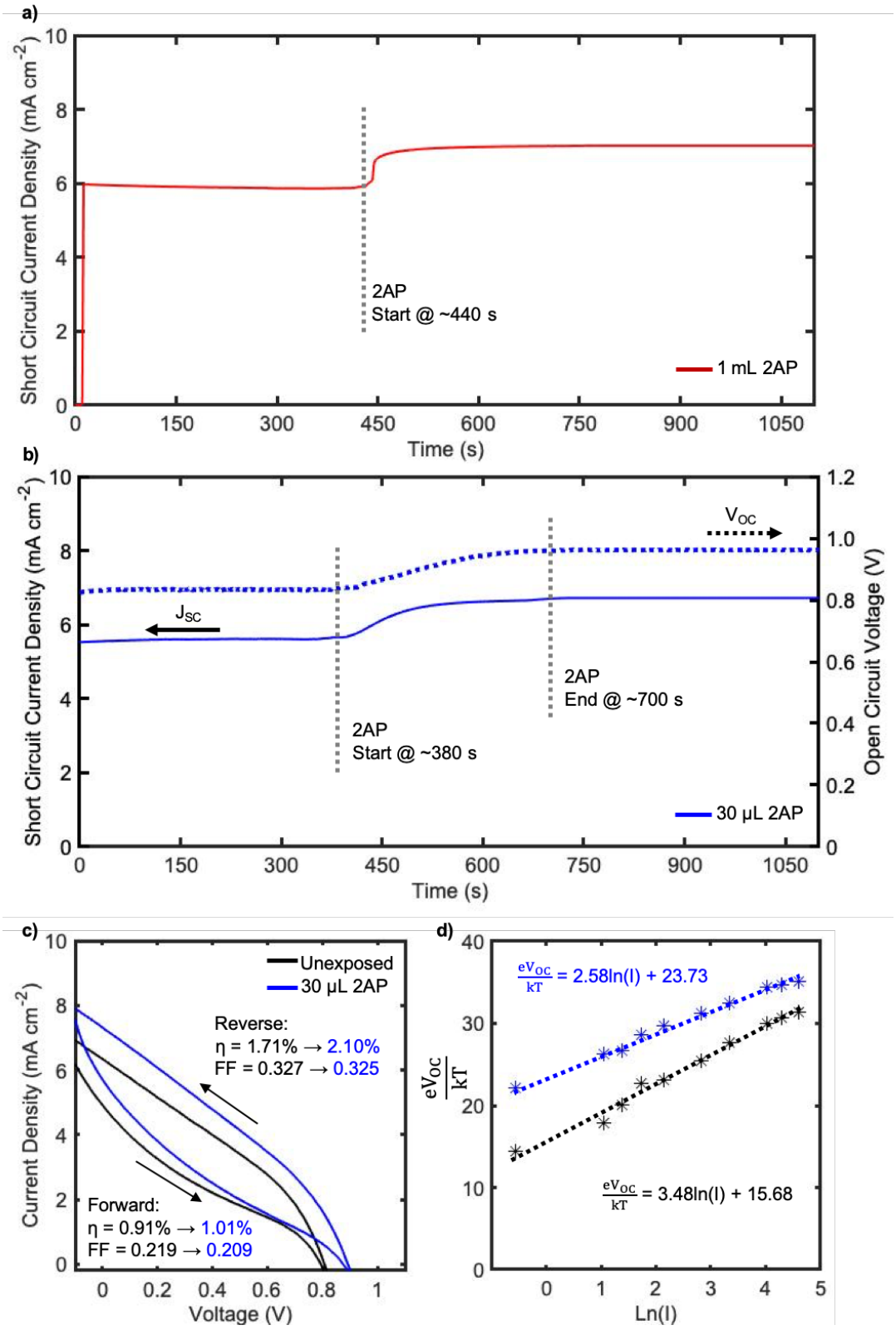

Figure 5.8. (a) *In situ*-measured steady-state short circuit current density of QIBC PSCs during an exposure to 1 mL of 2AP. (b) *In situ*-measured short circuit current density and open circuit voltage of QIBC PSCs during an exposure to 30 µL of 2AP. (c) J-V characteristics of QIBC PSCs before and after the exposure to 30 µL of 2AP. (d) Results of the suns-V_{OC} experiment on QIBC PSC before and after an exposure to 30 µL of 2AP.

Next, the photoluminescence mapping measurement was performed following the methods used in the TBP study (**Figure 5.9a**). During this experiment, a $MAPbI_3$ film was deposited on a planar Glass/FTO/TiO_2 substrate and exposed to 30 μL of 2AP. As a result of the vapour treatment, the photoluminescence intensity increased by ~24% versus its initial value. This further confirms the reduction in a number of trap states present at the surface of the perovskite material. The XRD examination of an unexposed and 2AP-passivated QIBC PSCs did not show any differences in the diffraction patterns (**Figure 5.9b**). This is in line with study performed by Yue *et al.* [233] on perovskite passivation with different pyridine derivatives. Similarly, no significant difference in reflection, transmission and absorption between the samples was observed in an UV-vis measurement (**Figure 5.9c**). The SEM examination shows that 2AP does not induce any morphological changes at the top surface of perovskite (**Figure 5.9d**).

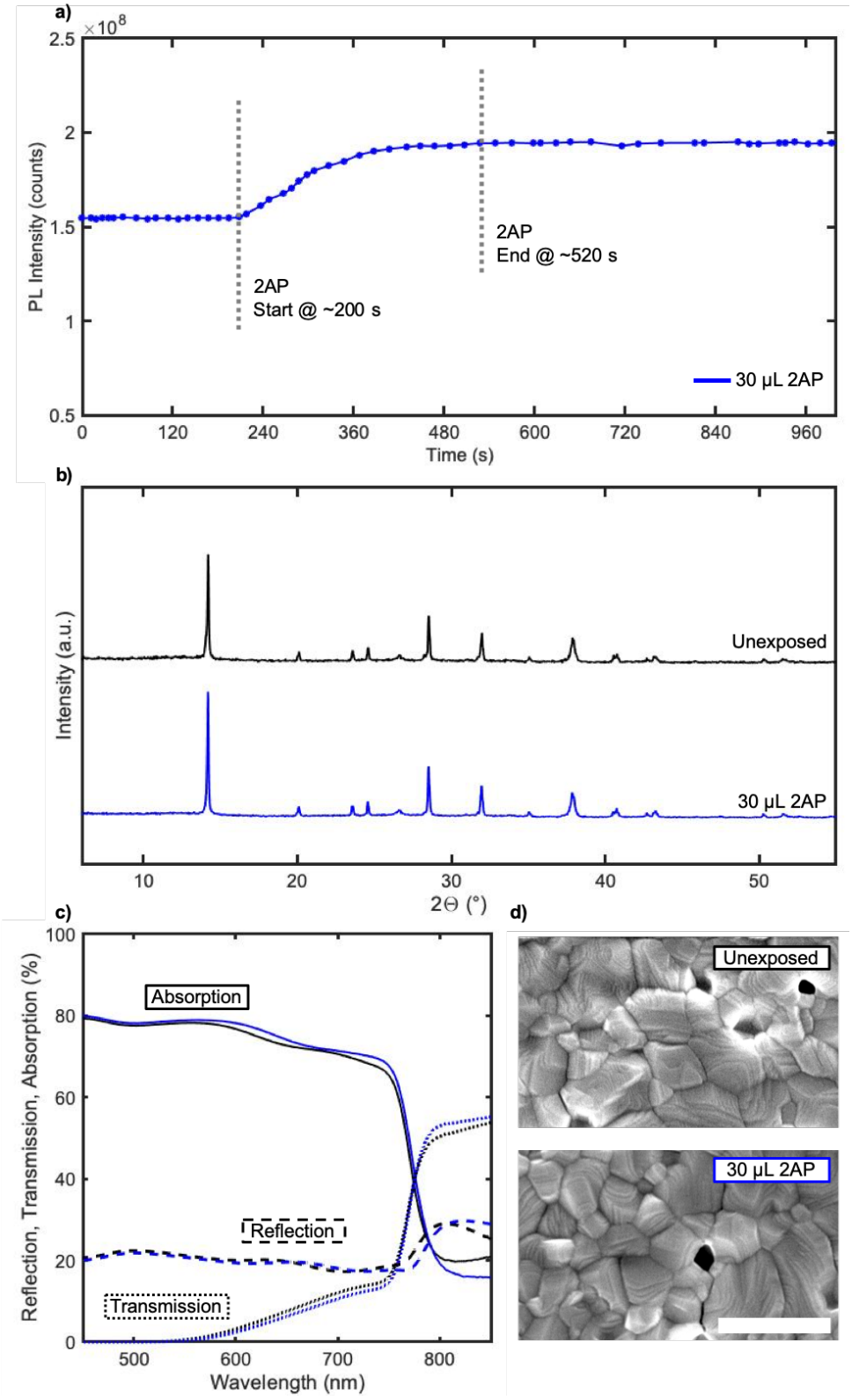

Figure 5.9. (a) The evolution of photoluminescence intensity of planar Glass/FTO/TiO_2/$MAPbI_3$ samples during 2AP vapour exposure. (b) XRD diffraction patterns of the unexposed sample, as well as samples exposed to 30 µL of 2AP. (c) Comparison of UV-vis transmission, reflection and absorption spectra of perovskite between unexposed sample and sample exposed to 30 µL of 2AP. Films deposited on Glass/FTO. (d) SEM images of QIBC PSC before and after the exposure to 30 µL of 2AP. Scale bar 500 nm.

5.2.3 N,N-dimethylformamide treatment

Results presented by Zhu *et al.* [230] were the inspiration for the last vapour exposure experiment presented in this Chapter. In his study, Zhu deposited $MAPbI_3$ films via spin-coating on top of Glass/FTO/TiO_2(mesoporous) substrates, in order to manufacture planar perovskite solar cells. However, after the deposition and annealing of the perovskite layer, he exposed it to multiple cycles of DMF vapour fumigation and re-annealing, before completing the devices with a layer of spiro-MeOTAD and a silver cathode. So-prepared solar cells showed a significant increase in their PCE. His vapour fumigation process was performed by introducing 0.5 mL of DMF dropped onto a filter paper, which was then placed directly next to the sample. Both the paper and the sample rested on a hotplate set to 90 °C and were subsequently covered with a petri dish to obtain a DMF-vapor atmosphere.

During the experiments performed for this Chapter, the QIBC PSCs were placed inside of the exposure chamber, resting on the hotplate set to 94 °C. The temperature at the surface of the sample (90 °C) was monitored with a thermocouple. The rapid exposure to the DMF vapour was achieved by heating the solvent to 125 °C prior to the exposure, and directing the total stream of nitrogen through the evaporation reservoir (F1 = 0 L/min, F2 = 5 L/min, T = 125 °C, V = 1 mL, **Figure 5.13**). After 5 s of such vapour treatment, the chamber was flushed with a nitrogen stream (F1 = 5 L/min, F2 = 0 L/min, **Figure 5.13**). The annealing process of the perovskite film at 90 °C and constant nitrogen flow was continued for an additional 10 min.

A steady-state short circuit current measurement was performed during the DMF vapour exposure. Surprisingly, QIBC PSCs treated this way did not show any significant improvement in generated photocurrent (**Figure 5.10,** in red). The photocurrent initially decreased, presumably due to dissolution of the perovskite layer. Upon annealing, the final short circuit current stabilised at a value similar to the initial one. This finding contradicts the results obtained by Zhu. However, one must know that the one-step method of perovskite deposition used in Zhu's study resulted in a dendritic film that poorly covered the substrate. The improvement gained by DMF-vapour fumigation was mainly caused by the recrystallisation of the perovskite into a densely-grained, uniform layer. In the study presented in this Chapter, the perovskite was deposited via a gas-assisted method, resulting in a densely -grained coverage of the QIBC electrodes with perovskite. This may be the reason why no significant improvement in photogenerated current was observed in this experiment.

In contrast, fascinating results were observed when aged QIBC PSCs were exposed to the same DMF vapour treatment. In preparation for this study, all solar cells were stored for 2 weeks in a dark dry box. Upon the exposure, a photogenerated current showed a similar trend as in the case of the non-aged ("fresh") samples – an initial decrease, followed by the

recrystallisation and a rise of the photocurrent. However, this time, the final short circuit current stabilised at a value 32.9% higher than the initial one. (**Figure 5.10**, in blue).

Similar trends in short circuit currents were observed at J-V characteristics of the fresh and aged QIBC PSCs (**Figure 5.10c-d)**. Upon the exposure, a J-V characteristic of the fresh samples remained nearly the same and the differences in PCE and FF were negligible. However, the aged samples measured before and after the exposure to DMF vapour showed a significant enhancement in PCE of the device (24% in the reverse and 38% in the forward direction). The open circuit voltage of the devices remained constant. Interestingly, the increase in PCE was accompanied with a slight (7%) drop of FF in the reverse direction and 6% increase in the forward direction. An origin of the changes in the FF should be a subject of further investigation in future work.

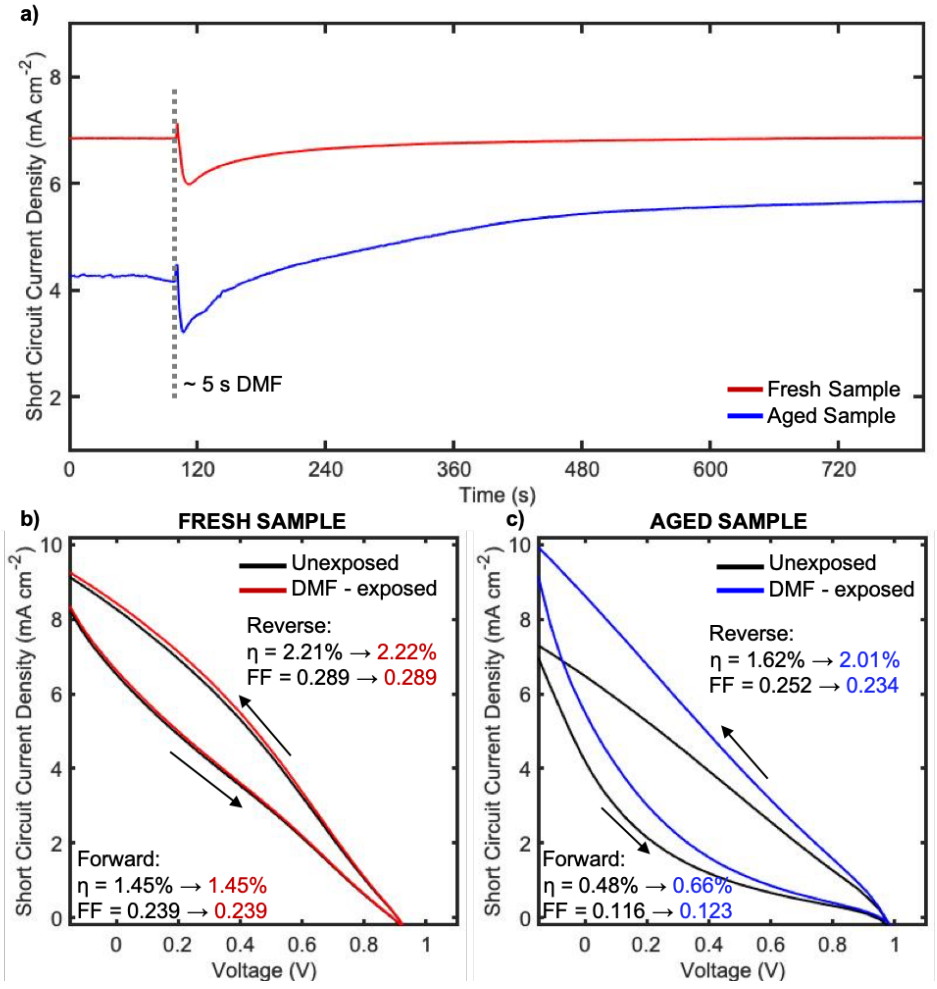

Figure 5.10. (a) *In situ*-measured steady-state short circuit current density of a fresh and aged QIBC PSCs during a rapid exposure to 1 mL of DMF. J-V characteristics of a (b) fresh and (c) an aged QIBC PSCs before and after the exposure to 30 μL of 2AP.

In order to investigate the origin of such significant changes in the performance of the aged samples upon the exposure to DMF vapour, and lack of changes in the performance of the fresh samples, a morphological study of the QIBC PSCs was performed. **Figure 5.11a** shows SEM images of a fresh sample before and after the DMF treatment. As previously mentioned, a perovskite layer deposited on top of the QIBC electrodes via a gas-assisted method is non-dendric, but, rather homogenous, with numerous pin holes. The DMF exposure did not bring any significant changes to the morphology of this layer.

The SEM analysis revealed the influence of aging on the QIBC PSCs. It was discovered that storing the devices for a prolonged time, even in a dry environment, brings tremendous changes to the morphology of the perovskite layer. **Figure 5.11b** shows multiple cracks at the top surface of the aged QIBC PSC, which align with the position of the QIBC electrodes. Over time, the perovskite layer seems to decompose faster at the edges of the cathode, and the samples appear rougher. The cracks are likely to impede the electrical connection between the grains of perovskite, thus, lowering the photocurrent generated by the device, as observed at **Figure 5.10**. Upon the exposure to DMF, the top surface of the aged sample smoothens and the number of cracks decreases. SEM images show that DMF treatment induces a self-repair recrystallization of the perovskite layer, a process previously described by Zhu *et al*.

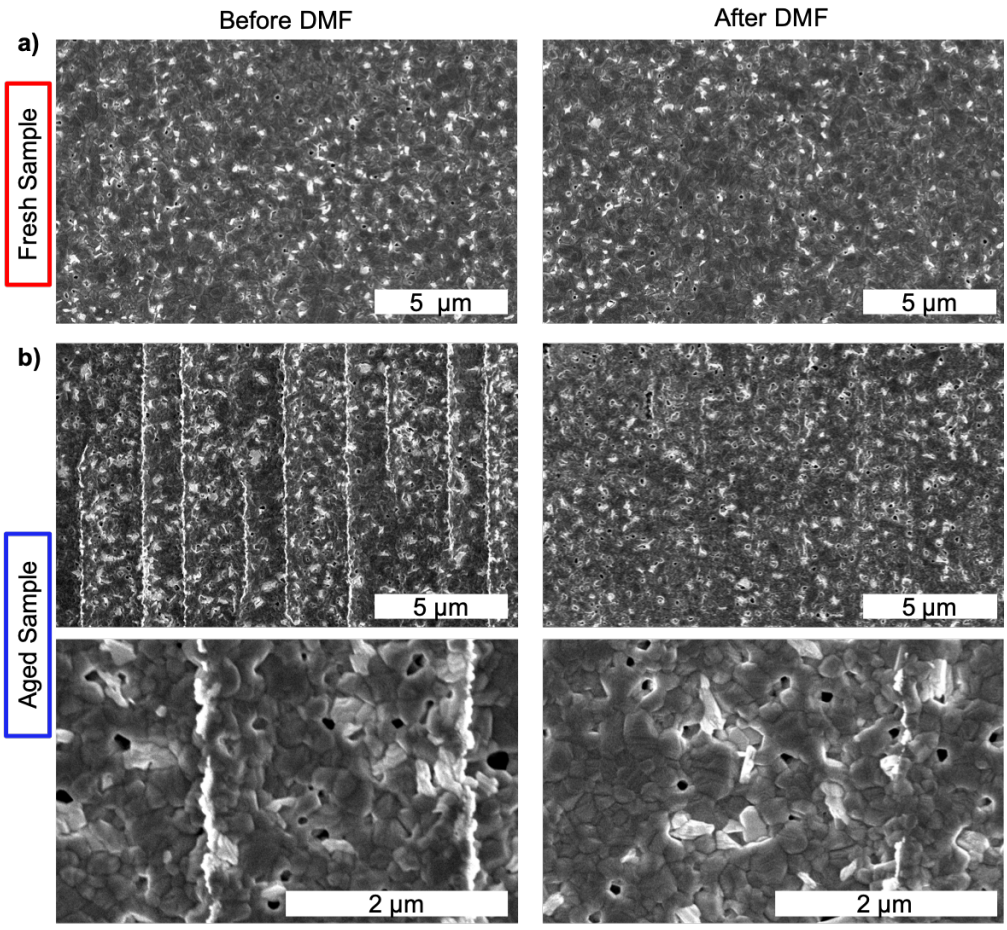

Figure 5.11. (a) SEM images of fresh QIBC PSC before and after the exposure to DMF. (b) SEM images of an aged QIBC PSC before and after the exposure to DMF at lower and higher magnifications.

The top surface of an aged QIBC PSC was examined with an atomic force microscope (AFM) before and after the DMF treatment (**Figure 5.12a**). Results of this experiment are in the good agreement with the SEM analysis. The AFM profiles extracted from the image of an untreated sample shows that over time, the perovskite layer undergoes decomposition and shrinks, giving rise to significant discontinuty of the top surface. The difference in the height of the perovskite resting on the cathode and on the anode reaches 100 nm. Upon DMF exposure, the surface of the QIBC PSC flattens and the edges become less sharp.

As a next step, a UV-vis spectroscopy was performed on an aged perovskite layer deposited on a Glass/FTO substrate (**Figure 5.12b**). Due to the small size of the solar cells, this experiment could not be performed on the QIBC substrate with sufficient accuracy. Thus, the results do not fully reflect the changes taking place in the real device. A slight decrease in the transmission of the layer was observed in the wavelength range 600 – 850 nm after the DMF treatment and, as a result, an increase in the absorption. However, this change is relatively

minor and does not explain the large gain in photocurrent observed for the aged QIBC PSC exposed to DMF. The reflection from the surface of the sample remained fairly constant across whole measured spectrum (400 – 850 nm).

XRD analysis on aged QIBC PSCs was performed in order to investigate if the DMF treatment brings any changes to the crystal structure of the perovskite (**Figure 5.12c**). The results show a strong peak at $2\theta \approx 11°$ for both the untreated and the DMF-treated solar cells. As mentioned before, this peak is usually attributed to PbI_2 and is caused by the chemical decomposition of the perovskite material. The results also show that upon exposure to DMF, the dominant peaks of $MAPbI_3$ ($2\theta \approx 14°$ and $2\theta \approx 28.5°$) become more prominent, indicating an improved crystallinity of the film. This is in agreement with the results reported by Zhu *et al.*

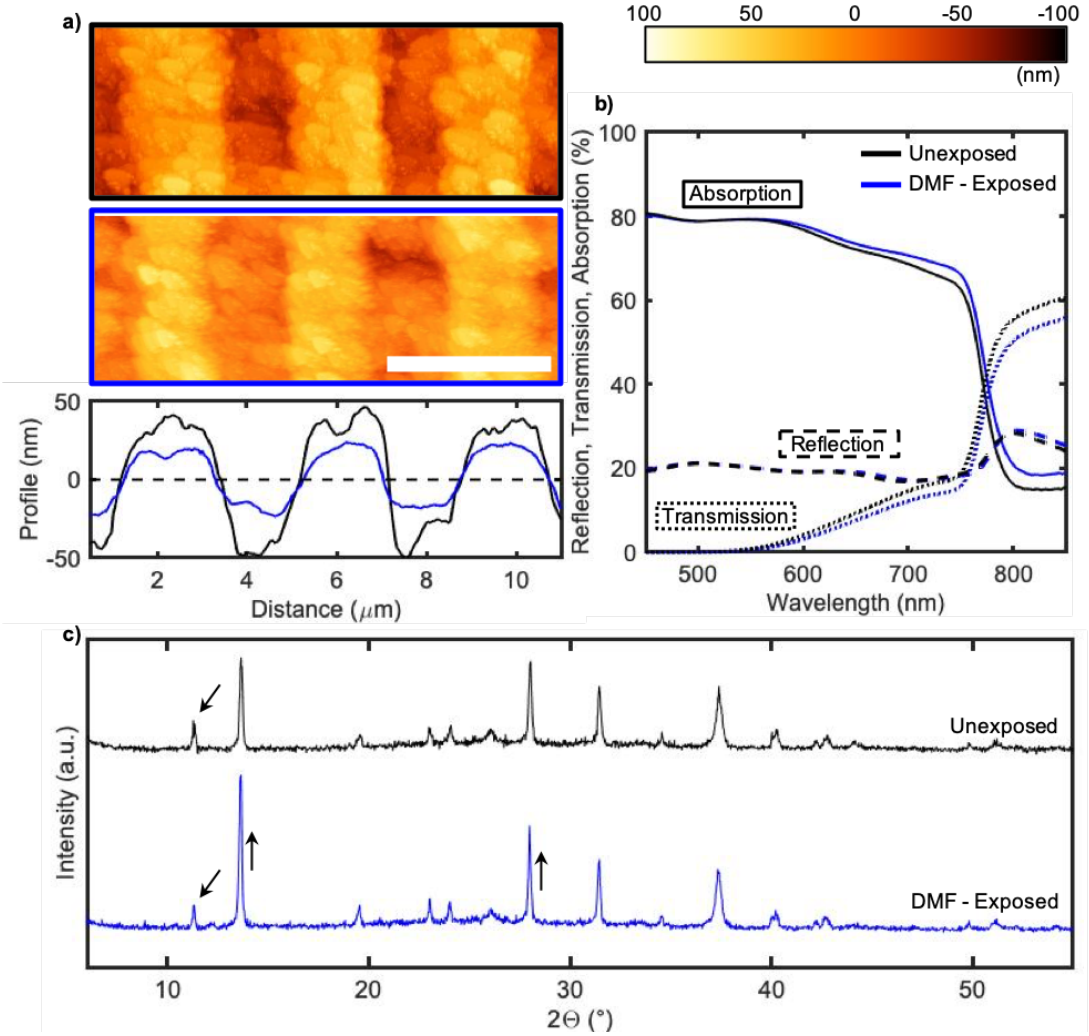

Figure 5.12. (a) AFM mapping results of an aged QIBC PSC before and after the DMF exposure, with the corresponding profiles, extracted from the images. Scale bar: 4 μm (b) Comparison of UV-vis transmission, reflection and absorption spectra of an aged perovskite before and after the exposure to DMF. Films deposited on Glass/FTO. (c) XRD diffraction patters of an aged QIBC PSC before and after the exposure to DMF.

5.3 Chapter conclusion

In this Chapter, three different post-treatments were performed on QIBC PSCs. The photovoltaic properties of the solar cells were measured *in situ*, using a pilot plant built for the purpose of this Thesis. Those experiments were complemented by various other measurement techniques, in order to find an explanation of the processes taking place on and inside of the perovskite film.

The first two chemicals used in this Chapter (TBP and 2AP) show a passivation effect on the surface trap states of the perovskite layer. Results of the TBP treatment indicate that choosing the right volume of the passivator is crucial if one aims to passivate the surface, rather than corrode the material. Slowing down the process of the exposure allows for an improvement in control over the experiment. On the other hand, a prolonged exposure to 2AP does not damage the perovskite layer. A smaller volume of the passivator can be used to passivate the surface trap states in order to reduce the consumption of the chemical and thus, the cost of the process. Additionally, in this set of experiments, the passivation was slowed down by diluting the stream of the vapour with nitrogen. However, the obtained results did not differ significantly in comparison to the rapid exposure.

The morphological study performed on aged QIBC PSCs show that the perovskite layer resting on QIBC electrodes undergoes massive changes over time, even if the sample is stored in a dry environment. The aged samples can be recrystalised with a short and rapid exposure to the DMF vapour in order to smoothen the top surface. This treatment reduces the number of cracks present at the surface, increases the photogenerated current and improves the PCE of the device. This study also suggests the need for encapsulating the top surface of BC PSCs – a topic explored in greater detail in Chapter 6 of this Thesis.

The post-treatment experiments performed on QIBC PSCs and presented in this Chapter can be applied to perovskite thin films used in planar perovskite devices. They have the potential to significantly speed up the optimization of post-treatment processes and assist in the improvement of PCE of the most efficient perovskite solar cells.

5.4 Methods and materials

As in the previous Chapter of this Thesis, QIBC electrodes were fabricated via a photolithography method, described in Chapter 3. An AXXIS e-beam evaporator supplied by Kurt J. Lesker was used to evaporate the following materials: Al_2O_3 (thickness: 150 nm), Al (thickness: 30 nm) and Ni (thickness: 50 nm). The electrodes were oxidised for 15 min at 300

°C to obrain a layer of NiO_x HSL. $MAPbI_3$ was deposited according to the gas-assisted method described in Chapter 3. The post-treatment experiments were performed in a pilot plant, built according to the process diagram presented on **Figure 5.13**.

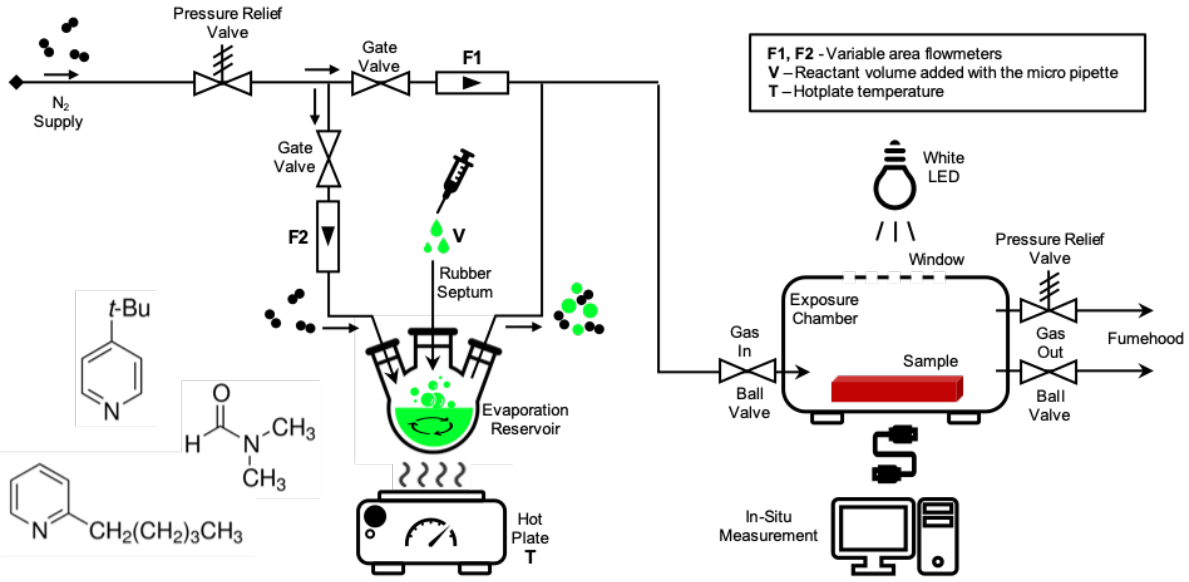

Figure 5.13. Piping and instrumentation diagram of the pilot plant used in the post treatment experiments presented in this Chapter.

X-ray diffraction (XRD) analysis was carried out in air with a Bruker D2 Phaser Diffractometer equipped with Cu Kα radiation and Scintillation counter 1-dimensional LYNXEYE detector in the 2θ range from 5 to 60°. AFM measurements were performed in air using a Dimension Icon (Veeco) system equipped with chromium-platinum coated conductive probes (ElectriMulti75-G, BudgetSensors). PL images were collected using a setup described in Chapter 4 in this Thesis (Section 4.4). This measurement was performed on a planar perovskite film, deposited on glass/FTO/TiO_2 substrate (area: 1.5 cm^2). The *in situ* $J_{sc,}$ Voc and J-V measurements were recorded on a Zahner Electrochemical Workstation ZENNIUM and Thales Z3 software. During those measurements, solar cells were illuminated with a White (5650K) Rebel LED controlled by a MAISHENG MS305D DC power supply. The light intensity was adjusted to 1000 W m^{-2} AM 1.5G and monitored using a secondary reference photodiode (Hamamatsu S1133, with KG-5 filter, 2.8 × 2.4 mm of photosensitive area), calibrated by a certified reference cell (ISE CalLab PV Cells, certified by Fraunchofer ISE). Surface SEM images were obtained using a Nova NanoSEM 450 Scanning Electron Microscope operated at 3 kV and spot size 2.0. UV-Vis spectra of the films were measured

using a Perkin Elmer Lambda 1050 spectrometer fitted with an integrating sphere attachment in an ambient atmosphere.

6. A solution processed antireflective coating for back-contact perovskite solar cells

6.1 Chapter introduction

The QIBC architecture of PSCs allows for the direct illumination of the perovskite photo-absorber layer, thus eliminating the transmission losses caused by the glass substrate and one of the charge selective layers in the planar structure (**Figure 6.1a-b**). Numerical simulations performed by Ma *et al.* [189] show that BC PSCs can theoretically obtain PCEs higher than the planar devices. However, to date all reported BC PSCs show significantly lower photogenerated currents and fill factors (and thus efficiencies) than their conventional planar counterparts. One potential source of the current loss is the reflection of light by the perovskite layer that occurs due to a high refractive index mismatch between perovskite and air.

The minimization of light reflectance in order to enhance the photovoltaic performance of BC solar cells has already been explored for decades. For instance, the light reflection from the top surface of monocrystalline silicon solar cells is reduced by texturing it with a pyramid-shaped pattern, usually through anisotropic etching in alkaline solutions. [279] This process is less effective for multicrystalline silicon solar cells, due to the random orientation of the crystals. Therefore, for these devices, the texturing of the top surface is usually achieved through reactive ion etching [280] or acidic etching. [281]

Another approach to increase light absorption, typically used in conjunction with surface texturing in inorganic solar cells, is the application of an antireflective coating (ARC). This addresses the mismatch of refractive indices at the photoaborber/air interface, thus decreasing the reflection at the surface of the solar cell. A commonly used ARC in silicon solar cells is SiN_4, obtained through low-pressure high-temperature chemical vapor deposition. Additionally, the silicon nitride film rests on SiO_2 (passivation layer), obtained through a thermal oxidation of the top surface of a silicon SC.

Due to the sensitivity of the photoabsorber material, the texturing techniques typically employed in minimizing reflective losses in conventional inorganic solar cells cannot be directly transferred to hybrid organic-inorganic BC PSCs, leaving the application of an ARC as the only facile route to minimize reflection losses. However, this still presents a challenge; the ARC and the solvents used in its deposition must be chemically compatible with the underlying perovskite layer.

One candidate is poly(methyl methacrylate) (PMMA), with a refractive index of ~1.5, [282] which lies between the refractive indices of air and $MAPbI_3$ [283] in the visible wavelength spectrum (**Figure 6.1c-d**).

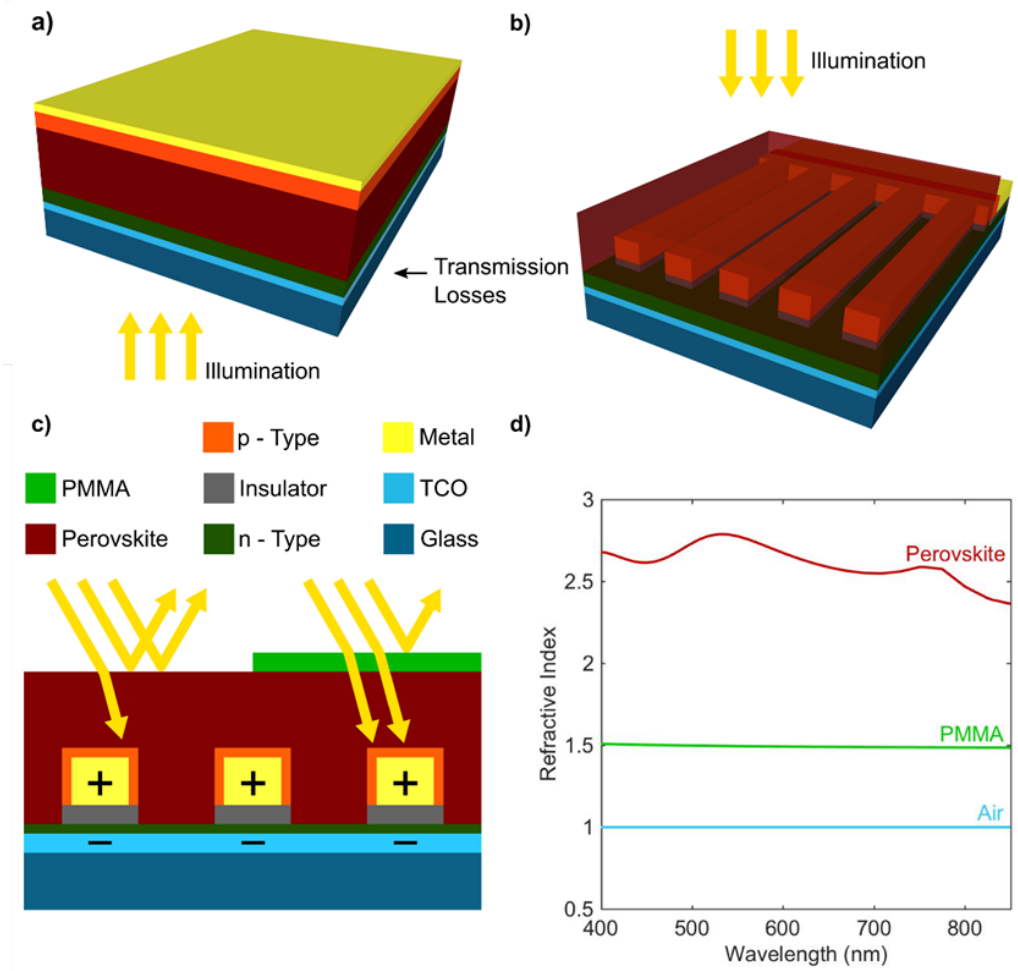

Figure 6.1. Schematic cross-section diagrams of (a) a planar and (b) a QIBC PSC. TCO – transparent conductive oxide. (c) Reduced reflection from a top layer of perovskite solar cell after the deposition of the PMMA ARC. (d) Refractive index dependence on wavelength for air, PMMA [282] and $MAPbI_3$ [283].

One of the biggest advantages of using this polymer is the ease of its deposition. A layer of PMMA ARC can be deposited simply by spin-coating a dilute solution of PMMA in chlorobenzene onto a perovskite film. Secondly, the chemical compatibility of PMMA with perovskite has already been demonstrated and no adverse effects on the underlying perovskite layer were observed during its use as an encapsulant in energy-dispersive X-ray [284] and surface photovoltage spectroscopy measurements, [285] and in microwave photoconductivity imaging. Furthermore, in 2014 Habisreutinger *et al.* proposed a charge selective layer made of carbon nanotubes and PMMA that sealed the perovskite layer, thus retarding moisture-related degradation processes. [286], [287] The vulnerability of PSCs to moisture is caused by hygroscopicity of organic cations and remains one of the biggest challenges of perovskite technology. As an example, upon exposure to water, $MAPbI_3$ rapidly decomposes to MAI and

PbI_2. [288] PMMA, amongst many other polymers, is hydrophobic and it was proven to provide a protection of the perovskite layer from humidity. [289]

This Chapter presents theoretical and experimental investigations into the use of PMMA as an ARC for QIBC perovskite solar cell devices. Transfer matrix optical simulations are performed to predict the performance enhancement of the solar cells and determine the optimal thickness of the PMMA ARC. UV-Vis spectroscopic measurements are used to quantify the effect of the PMMA ARC over the different areas of the QIBC PSC. The device measurements confirm an increase in PCE with the use of the ARC. Furthermore, photoluminescence mapping experiments reveal a passivation effect of the top surface of QIBC PSC observed after the deposition of PMMA layer.

6.2 Results and discussion

As a first step, transfer matrix (TM) optical modelling was performed for a QIBC PSC. For the purpose of the calculations, the QIBC PSC was modelled to best reflect its real counterpart. The anode of the QIBC electrode was assumed to be a continuous layer of FTO on a glass substrate, coated with 50 nm TiO_2. The comb-shaped cathode consisted of a 50 nm-thick Al layer and 30 nm-thick Ni layer, coated with a 2 nm-thick NiO_x layer. The cathode and anode were separated by a 150 nm-thick Al_2O_3 insulating layer. The modelled QIBC PSC was completed by a layer of $MAPbI_3$ perovskite photo-absorber layer, covering both the anode and cathode in a conformal manner with thicknesses of 600 nm and 370 nm, respectively.

The TM modelling was performed for the device without and with a PMMA ARC over the perovskite photo-absorber. The calculations were undertaken in Matlab with bespoke software based on the formalism of Pettersson *et al*. [290] **Figure 6.2a** shows the calculated transmission and reflection spectra of the QIBC PSC based on literature refractive index values [282], [283], [291]–[295] without (red line) and with the PMMA ARC (green line). The absorption spectra of the perovskite photo-absorber layer in both cases were calculated from the transmission and reflection spectra, taking into account the effects of the internal back reflection from the underlying layers (**Figure 6.2b**). All presented graphs are a result of an average over both electrode regions.

Based on the calculated absorption spectra, the estimated the maximum achievable short-circuit photocurrent density (J_{SC}) under incident AM1.5G solar irradiation is 18.8 and 22.9 mA cm^{-2} for the device without and with a PMMA ARC, respectively. The >20% gain in photocurrent caused by the ARC results from a greater impedance matching to the absorbing perovskite layer and an increase in the photo-generation near the front of the device (**Figure**

6.2c). The TM optical modelling revealed that such a significant increase in photocurrent can be achieved with an optimum thickness of 85 nm for the PMMA ARC (**Figure 6.2d**).

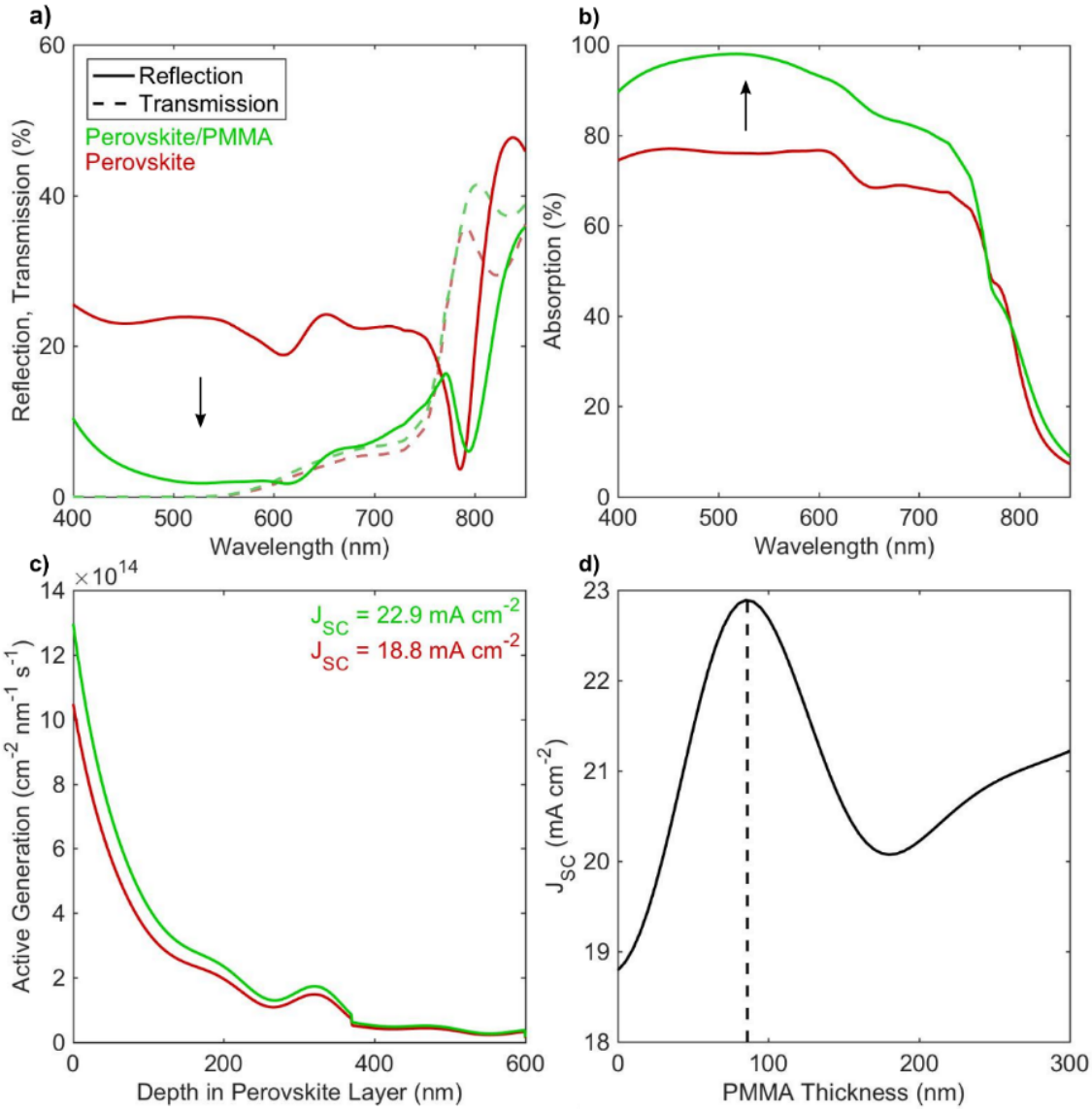

Figure 6.2. Transfer matrix optical simulation of a QIBC PSC with (green line) and without (red line) the 85 nm thick PMMA ARC. (a) Transmission and reflection spectra based on the refractive indices data acquired from the literature, calculated as a result of the weighted average over both contacts. (b) Calculated absorption spectra of the perovskite layer. (c) Simulated active charge carrier generation through the photoactive area of the device. (d) Calculated maximum J_{SC} value, assuming 100% charge carrier collection efficiency, as a function of PMMA thickness, with an optimum at 85 nm.

As a next step, a ~400 nm thick perovskite film was characterized through UV-Vis spectroscopy measurements, with and without the PMMA ARC. Due to the small active area (2 × 2 mm) of the photovoltaic devices prepared in this study, a direct optical characterization of QIBC PSC could not be achieved with satisfactory accuracy. Therefore, the experiments

were performed on glass substrates covered with FTO. The thickness of the PMMA ARC layer (~85 nm) was chosen according to the results of the TM modelling.

The application of the PMMA ARC resulted in a negligible change in transmission below the 750 nm wavelength. The presence of the PMMA layer caused a reduction in the average reflection from ~21.5 % to ~12.5 % over the visible part of the spectrum (400 – 750 nm), yielding a ~40 % relative decrease in reflection (**Figure 6.3a**). This is attributed to a reduction in both specular and diffuse reflection, (**Figure 6.3c-d**) which suggests a random orientation of the perovskite crystals on the film surface. The significant change in the optical properties of the sample resulted in ~11.5% relative increase in photo-absorption of the perovskite film, as calculated as an average over the visible component of the absorption spectra (**Figure 6.3b**). The difference between the anticipated gain (calculated through TM modelling) and the gain observed in the acquired absorption spectra can be caused by irregular coverage of the perovskite surface by the ARC due to surface roughness. However, the UV-Vis spectroscopy results clearly demonstrate that a beneficial increase in absorption can be achieved by coating PMMA onto a perovskite photo-absorber layer deposited onto a QIBC electrode.

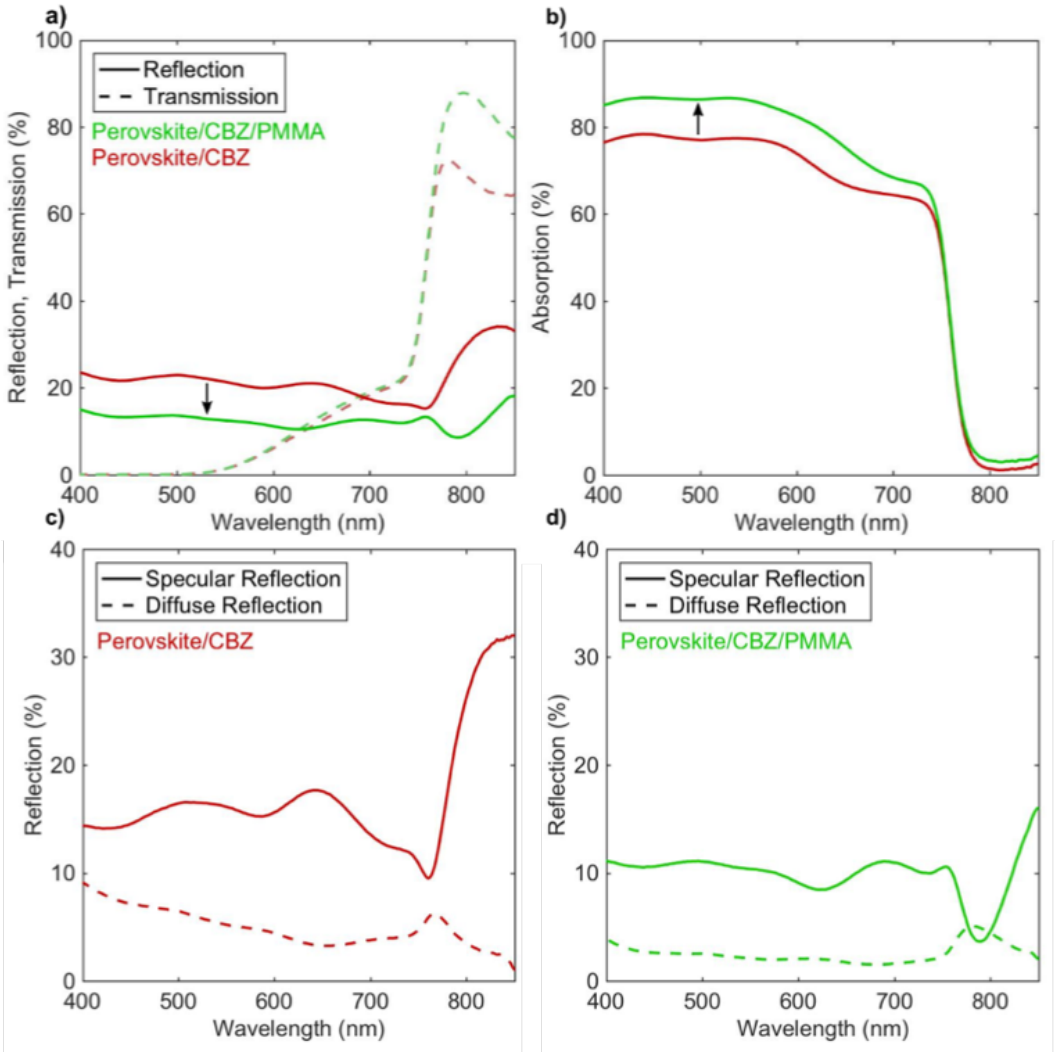

Figure 6.3. (a) Transmission and reflection spectra of the perovskite layers on an FTO-coated glass substrate. (b) Calculated absorption spectra of the perovskite layers. Specular and diffuse reflection UV-Vis measurements of perovskite layer (c) before and (d) after the deposition of PMMA ARC.

In order to validate the predictions of the TM modelling, QIBC PSCs were fabricated and measured under simulated solar irradiation, without and with a PMMA ARC. The SEM cross-section image of the device shows that the thickness of the PMMA ARC layer varies between 80 and 90 nm across the sample surface (**Figure 6.4a**). This is caused by the random crystal orientation of the perovskite layer deposited on top of the QIBC electrodes. Moreover, a top view SEM picture of the sample (prior to PMMA deposition) further reveals numerous imperfections in the perovskite film, referred to as 'pin holes' elsewhere (**Figure 6.4b**).

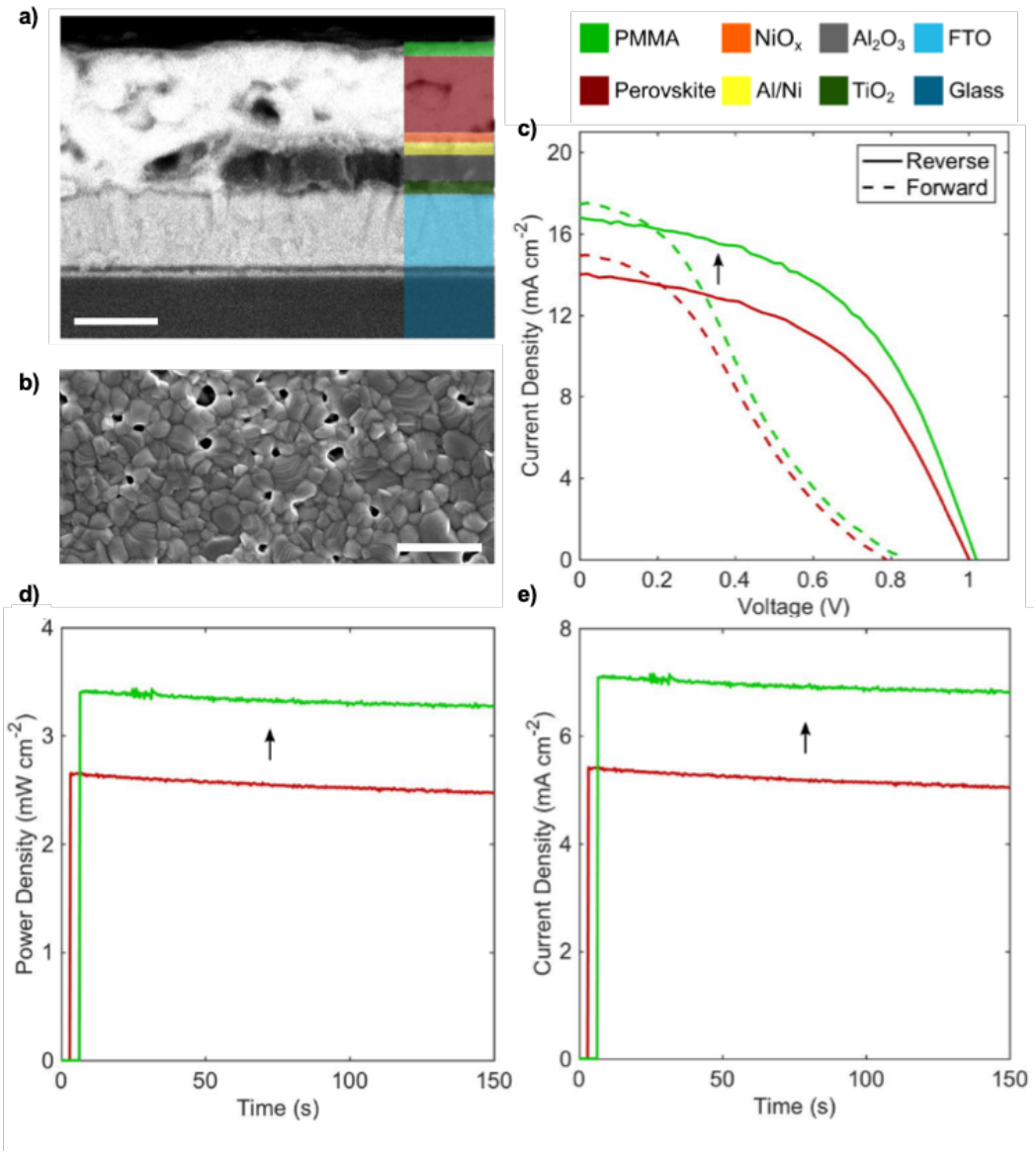

Figure 6.4. (a) Cross-section SEM image of the back-contact perovskite solar cells covered with PMMA layer, scale bar 400 nm. (b) High magnification SEM images of perovskite layer deposited on top of QIBC electrodes (without PMMA ARC), scale bar 400 nm. (c) Typical J-V characteristic of QIBC PSCs under AM1.5 (1000 W/m^2) simulated solar irradiation in reverse and forward scan directions before and after the deposition of the PMMA ARC. (d) Typical time evolution of stabilized maximum power output and (e) corresponding maximum power point photocurrent. Red line – samples without ARC, green line – samples covered with PMMA ARC.

In order to distinguish the photovoltaic performance improvements resulting from the antireflective PMMA layer from those resulting from solvent exposure at the perovskite/air interface, all solar cells were tested in the following sequence: (a) QIBC PSC as-fabricated, (b) the same device after pure chlorobenzene was spin-coated on the surface and (c) the same device after an additional spin-coating step with PMMA in chlorobenzene to apply the ARC. The results are presented in **Tables 6.1-6.4**.

Table 6.1. Performance of QIBC PSCs, without PMMA ARC.

Perovskite

	$(J_{SC})_{REV}$ mA cm^{-2}	$(J_{SC})_{FOR}$ mA cm^{-2}	$(V_{OC})_{REV}$ V	$(V_{OC})_{FOR}$ V	$(FF)_{REV}$ %	$(FF)_{FOR}$ %	$(\eta)_{REV}$ %	$(\eta)_{FOR}$ %
Cell 1	12.17	12.65	0.961	0.720	42.43	20.96	4.96	1.91
Cell 2	10.58	11.46	0.978	0.741	40.48	15.67	4.19	1.33
Cell 3	11.70	12.76	0.961	0.702	38.35	16.96	4.31	1.52
Cell 4	13.00	12.51	0.899	0.661	36.10	14.52	4.22	1.20
Cell 5	11.12	11.73	0.981	0.801	39.06	14.37	4.26	1.35
Cell 6	13.14	13.91	0.959	0.721	37.36	22.05	4.71	2.21
Cell 7	11.59	12.92	0.981	0.742	35.46	15.22	4.03	1.46
Cell 8	16.00	16.93	0.960	0.841	51.80	29.02	7.96	4.13
Cell 9	15.57	16.40	1.019	0.821	49.97	26.80	7.93	3.61
Cell 10	14.78	15.16	1.020	0.820	50.95	27.85	7.68	3.46
Cell 11	14.35	15.70	1.000	0.840	45.87	20.56	6.58	2.71
Cell 12	15.61	16.51	1.020	0.799	49.74	27.66	7.92	3.65
average	**13.30**	**14.05**	**0.999**	**0.808**	**43.13**	**20.97**	**5.73**	**2.38**

Table 6.2. Performance of the same QIBC PSCs, without PMMA ARC, after spin-coating of chlorobenzene on surface.

Perovskite/CBZ

	$(J_{SC})_{REV}$ mA cm^{-2}	$(J_{SC})_{FOR}$ mA cm^{-2}	$(V_{OC})_{REV}$ V	$(V_{OC})_{FOR}$ V	$(FF)_{REV}$ %	$(FF)_{FOR}$ %	$(\eta)_{REV}$ %	$(\eta)_{FOR}$ %
Cell 1	13.76	14.12	0.980	0.722	43.61	22.38	5.88	2.28
Cell 2	11.69	12.92	0.981	0.739	39.78	19.47	4.56	1.86
Cell 3	13.07	13.90	0.960	0.720	39.06	21.49	4.90	2.15
Cell 4	12.65	12.36	0.919	0.702	36.20	15.22	4.21	1.32
Cell 5	11.20	12.25	0.981	0.803	38.79	15.66	4.26	1.54
Cell 6	12.70	13.42	0.959	0.740	38.17	23.15	4.65	2.30
Cell 7	11.75	12.93	0.980	0.739	35.51	17.05	4.09	1.63
Cell 8	15.76	15.97	0.980	0.800	56.65	39.23	8.75	5.01
Cell 9	15.10	15.50	1.010	0.801	54.11	36.18	8.25	4.49
Cell 10	13.94	14.10	1.011	0.800	53.65	37.68	7.56	4.25
Cell 11	13.96	14.91	1.010	0.800	48.25	29.92	6.80	3.57
Cell 12	15.08	15.81	1.010	0.800	51.04	33.74	7.77	4.27
average	**13.39**	**14.02**	**1.000**	**0.795**	**44.57**	**25.93**	**5.97**	**2.89**

Table 6.3. Performance of the same QIBC PSCs, covered with PMMA ARC.

Perovskite/CBZ/PMMA

	$(J_{SC})_{REV}$ mA cm^{-2}	$(J_{SC})_{FOR}$ mA cm^{-2}	$(V_{OC})_{REV}$ V	$(V_{OC})_{FOR}$ V	$(FF)_{REV}$ %	$(FF)_{FOR}$ %	$(\eta)_{REV}$ %	$(\eta)_{FOR}$ %
Cell 1	16.13	15.98	0.980	0.759	45.74	27.79	7.23	3.37
Cell 2	14.84	15.05	1.000	0.760	44.12	24.56	6.55	2.81
Cell 3	15.50	15.74	0.959	0.740	41.83	25.49	6.22	2.97
Cell 4	14.87	13.64	0.840	0.659	36.50	18.37	4.56	1.65
Cell 5	15.18	15.57	0.980	0.799	41.59	22.10	6.19	2.75
Cell 6	16.07	15.60	1.000	0.781	41.49	28.25	6.67	3.44
Cell 7	14.66	14.98	0.980	0.779	35.92	23.38	5.16	2.73
Cell 8	18.32	18.56	1.040	0.880	55.05	34.77	10.49	5.68
Cell 9	17.65	18.19	1.040	0.840	54.88	33.71	10.07	5.15
Cell 10	16.91	17.62	1.040	0.880	54.34	32.51	9.56	5.04
Cell 11	16.79	17.45	1.021	0.840	49.83	28.53	8.54	4.18
Cell 12	17.58	18.26	1.020	0.880	50.96	28.70	9.14	4.61
average	**16.21**	**16.39**	**1.009**	**0.825**	**46.02**	**27.35**	**7.53**	**3.70**

Table 6.4. Stable power output of the devices during aforementioned three measurements

	$(\eta_\infty)_P$ %	$(\eta_\infty)_{CBZ}$ %	$(\eta_\infty)_{PMMA}$ %
Cell 1	2.08	2.09	2.60
Cell 2	1.64	1.75	2.26
Cell 3	1.80	1.91	2.46
Cell 4	1.81	1.80	2.16
Cell 5	1.76	1.69	2.46
Cell 6	1.97	1.96	2.74
Cell 7	1.50	1.49	2.35
Cell 8	3.56	3.49	4.41
Cell 9	3.21	3.32	4.16
Cell 10	3.30	3.15	4.22
Cell 11	2.37	2.51	3.30
Cell 12	3.34	3.43	3.74
average	**2.36**	**2.38**	**3.07**

The chlorobenzene treatment only brought about very minor changes in photovoltaic performance. Short circuit currents (J_{SC}) and open-circuit voltages (V_{OC}) recorded in forward and reverse bias scan directions varied by less than 2 % as a result of the treatment. All devices showed a strong hysteresis behaviour, with a scan-direction dependent efficiency variability of

more than a factor of 2. Therefore, the maximum power point tracking was used in order to determine stabilized power outputs as a more meaningful estimate for the energy conversion efficiency of these solar cells.

Coating of the perovskite top surface with a thin layer of PMMA resulted in a significant improvement in the photovoltaic performance **(Figure 6.4c-e, Figure 6.5)**. Short circuit currents measured in reverse scan mode improved by ~21.5% to an average of 16.21 mA cm^{-2}, while stabilized power conversion efficiencies improved by ~31% to an average of 3.07 %. The measured short circuit current is lower than the predicted ideal value due to the anticipated (but not modelled) recombination losses inside of the perovskite material and at the interfaces. The observed improvements in fill factors (< 6%) and open circuit voltages (4%) were only marginal. The relative changes of all PV parameters of samples perovskite/CBZ/PMMA versus perovskite/CBZ are summarised on **Figure 6.5**.

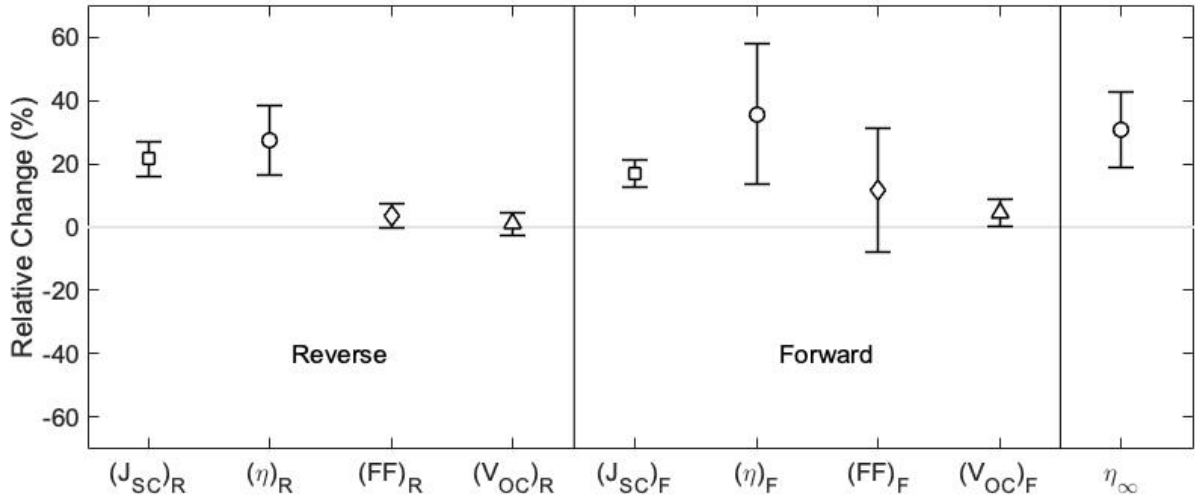

Figure 6.5. Relative percentage change of QIBC PSCs parameters after the deposition of PMMA ARC. The relative change is calculated as an average of the results obtained for all samples.

The best performing QIBC PSC with a PMMA ARC exhibited a J_{SC} of 18.6 mA cm^{-2} and a stabilized power output of 4.41 %, which is to date the highest reported efficiency for a QIBC PSC **(Figure 6.6)**.

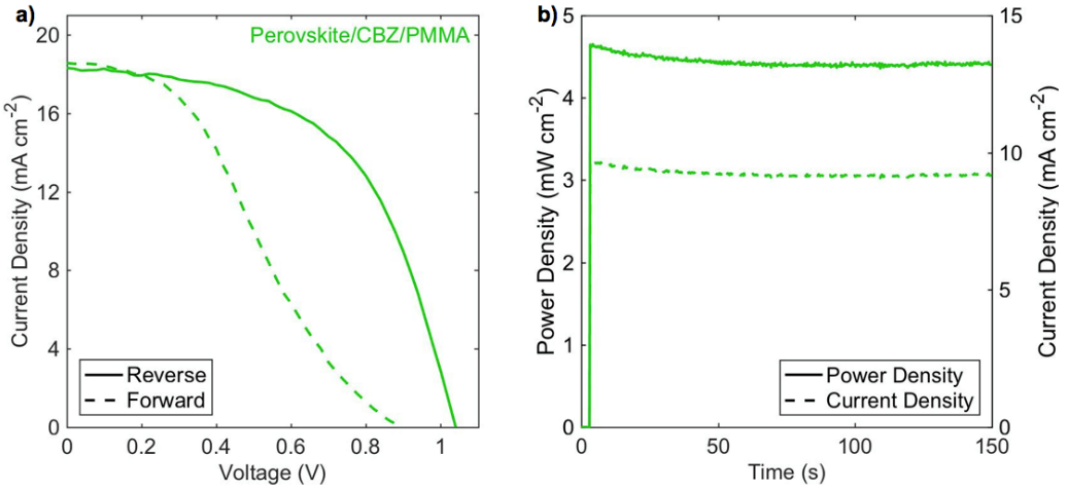

Figure 6.6. (a) Current voltage characteristic of the champion QIBC PSC. (b) Power density and corresponding current density tracking.

The relative increase in short circuit current being greater than the increase in light absorption would suggest that the application of the PMMA layer may also have a passivating effect on the surface of the perovskite layer, as previously reported. [205], [296]–[298] This was proven by space-resolved photoluminescence (PL) measurements on QIBC PSCs in air, before and after PMMA deposition (**Figure 6.7a-b**). The results of the measurements show that PL intensity for a perovskite film capped with a PMMA layer is significantly higher, compared to a PL intensity measured for the same perovskite film prior coating with the PMMA layer and after spin-coating pure CBZ. This is in agreement with other reports, indicating that the lone pair electrons on C=O in PMMA bonded with the uncoordinated halide ions of perovskite, reducing a number of surface trap states of perovskite material. [299] Combined with the J-V measurements for complete devices this result suggest that the PMMA layer indeed has a passivation effect on the surface of perovskite film.

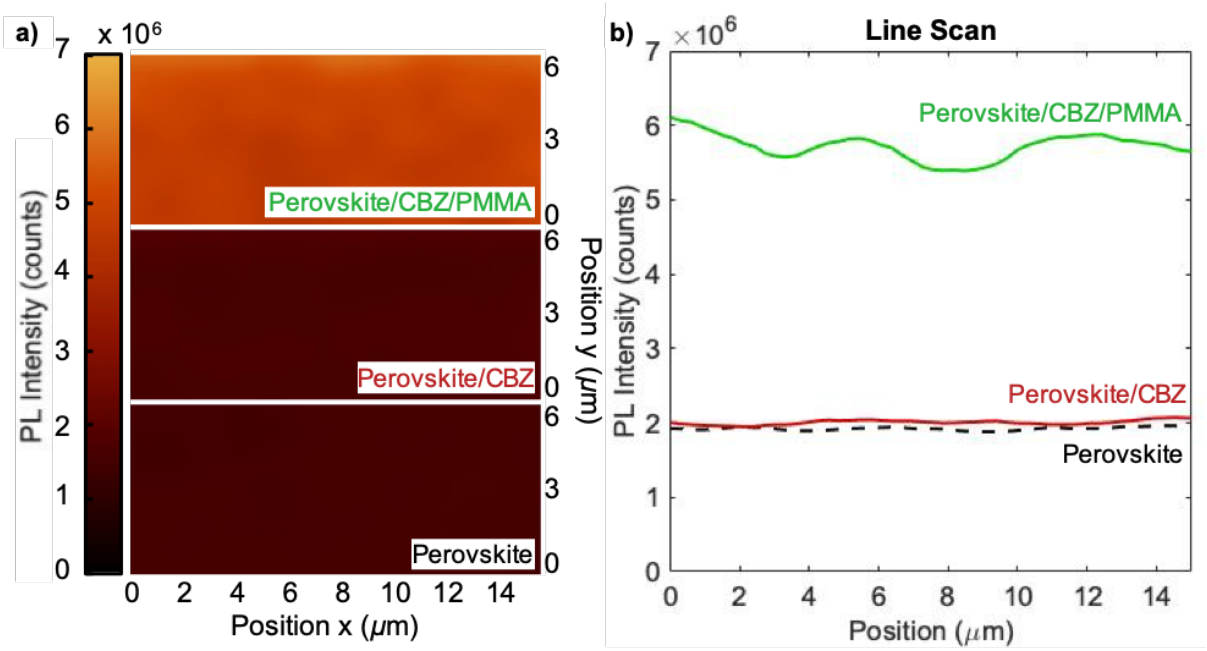

Figure 6.7. (a) Photoluminescence mapping of a perovskite film, perovskite film with spun-coated pure CBZ and after PMMA coating. Scanning dimension: 15 x 6 μm^2, excitation wavelength of the laser: 533 nm. (b) line scans extracted from the images.

6.3 Chapter conclusion

Employing a BC architecture is predicted to give perovskite solar cells with efficiencies that exceed those possible with a conventional sandwich structure. However, achieving these efficiencies requires minimization of the reflection at the photoabsorber/air interface. PMMA makes an effective ARC on QIBC perovskite solar cells due to its optical properties, chemical compatibility with the photoabsorber material, passivating properties, and its ease of deposition. With the optimal PMMA ARC thickness determined by transfer matrix modelling, QIBC PSCs demonstrated an increase in photocurrent, resulting in a ~30% average relative increase in the stabilized power output. This surface treatment yielded a champion solar cell with a stabilized power output of 4.41 %, the highest reported for a QIBC PSC.

6.4 Methods and materials

The QIBC electrodes were manufactured using methods described in Chapter 3 of this Thesis. A photo active material ($Cs_{0.05}FA_{0.79}MA_{0.16}PbI_{2.49}Br_{0.51}$) was deposited according to the antisolvent method, described in the aforementioned Chapter. Poly(methyl methacrylate) (PMMA) was dissolved in chlorobenzene (concentration 0.1 M) by stirring overnight at 70 °C. 70 μL of the PMMA solution was spin-coated at 1000 rpm for 45 s on top of the perovskite layer. All procedures were carried out in a N_2-filled glove box.

The J-V characteristics of the solar cells were measured under a nitrogen atmosphere with a computer-controlled Keithley 2400 Sourcemeter. The cells were illuminated with a 150 W Xenon lamp (Newport) coupled with an AM 1.5 G solar spectrum filter through a quartz window. The light intensity was adjusted and monitored using a secondary reference photodiode (Hamamatsu S1133, with KG-5 filter, 2.8 × 2.4 mm of photosensitive area), calibrated by a certified reference cell (PVMeasurements, certified by NREL) under 1000 W m^{-2} AM 1.5G illumination from an Oriel AAA solar simulator fitted with a 1000 W Xenon lamp. The samples were measured through a shading mask with a photo active area of 0.015 cm^2. The voltage was changed between −0.1 and 1.1 V with an interval of 0.02 V.

Cross section SEM images of the solar cells were obtained using a Zeiss Merlin Scanning Electron Microscope with 5kV beam energy. Surface SEM images were obtained using a Nova NanoSEM 450 Scanning Electron Microscope operated at 3 kV and spot size 2.0. UV-Vis spectra of the solar cells and the separate layers were measured using a Perkin Elmer Lambda 1050 spectrometer fitted with an integrating sphere attachment in an ambient atmosphere. Steady-state photoluminescence mapping (PL) was performed using WITec 300 R system with 533 nm laser excitation wavelength, with scan area: 15 x 6 μm^2.

7. Thesis conclusion

The discovery of a photovoltaic effect in perovskite materials is the greatest breakthrough in the field of solar cells this century. PSCs have come a long way in a relatively short period of time, with a new efficiency record being reported even few times a year. The performance of PSCs rapidly reached levels comparable with silicon solar cells and the research world is now addressing other factors that are preventing the perovskite technology from entering the market, e.g. scalability of the manufacturing process and stability. Further increases in device efficiencies and stability are reported by manipulating ratios of different cations and anions in perovskite materials, increasing the grain sizes, as well as through different strategies that improve the interface between functional layers.

Numerical simulations performed by Ma *et al.* [189] show that BC PSCs have the potential to exceed the performance of their planar counterparts. This is caused by beneficial light management in BC devices, i.e. the lack of shading and transmission losses, induced by layers resting on top of the photoactive material in conventional SCs. However, as of today, BC PSCs are not a matter of interest for the RE industry, due to their rather complicated manufacturing processes and relatively low efficiencies. Chapters 4 and 5 of this Thesis focus on other applications of BC PSCs, which can be beneficial in improving charge collection in all perovskite PV devices. A range of *in situ* measurements were performed utilising the novel QIBC architecture, allowing for rapid optimisation of process conditions.

Chapter 4 is an *in situ* investigation into the evolution of the structural, optoelectronic and photovoltaic properties of the perovskite during its formation on QIBC electrodes. Sun simulator experiments, complemented by PL and XRD analysis (all performed during the annealing of the photoactive layer), show that the biggest changes to the device performance and perovskite itself are taking place during the first few minutes of the annealing. It was discovered that those changes occur faster with an increase in the annealing temperature.

Chapter 5 presents post-treatment experiments on perovskite materials, a current “hot topic” in the perovskite scientific world. Utilising the QIBC architecture of PSCs and a pilot plant developed for the purpose of these experiments allowed for a higher level of control than ever reported in the perovskite field. The results show a passivating effect of 4-tert-butylpyridine and 2-amyl pyridine on the trap states present at the top surface of the perovskite layer. Choosing the right volume of TBP was critical to obtaining a passivating effect on the perovskite while simultaneously avoiding damage to the layer. The experiments with 2AP showed that exposing perovskite to a higher volume of the passivator does not harm the perovskite. However, the volume may be decreased in order to reduce the cost of the process.

Additionally, it was shown that N,N-dimethylformamide can recrystallise an aged perovskite resting on QIBC electrodes into a more homogenous layer, yielding an improvement in the device efficiency.

Throughout the process of collecting data for this Thesis, it was discovered that the perovskite resting on QIBC electrodes is undergoing significant morphological changes over time. This investigation reemphasised the need of capping the BC PSC with an encapsulating layer. One candidate, presented in Chapter 6 of this Thesis, is PMMA. This polymer was previously used by other researchers in the field as an encapsulant during various experiments on planar perovskite layers. The transfer matrix modelling revealed that PMMA has another beneficial effect on BC PSC, namely, it reduces the reflection from the top surface of perovskite, thus, it acts as an antireflective coating. The photocurrent generated by a QIBC PSC increased significantly when the QIBC PSC was covered by the PMMA ARC. This resulted in an improvement in the device efficiency. Furthermore, the PL mapping measurements showed that PMMA has a passivating effect on the trap states present at the top surface of the perovskite.

7.1 Future outlook

For the purpose of this Thesis, a few main improvements in the architecture of QIBC electrodes were incorporated, in comparison to the first devices reported by Jumabekov *et al.* Firstly, the replacement of the ZnO ESL layer with TiO_2 imparted a greater thermal stability onto the electrodes, which is particularly important during the oxidation of the nickel layer. Secondly, adding an additional bar at the top of the comb teeth brought an improvement in the durability of the electrodes, particularly important during the photoresist removal-sonication step. Thirdly, the Glass/FTO substrates used in the experiments had four separate FTO electrodes, which avoids any accidental interconnection between the devices and improving the accuracy of the solar simulator measurements. However, the QIBC PSCs still could benefit from further modifications. The morphology analysis performed by SEM on several occasions in this Thesis show that the layer of the perovskite deposited on top of the QIBC has multiple pinholes. Due to the novel architecture of QIBC electrodes, these pinholes did not impose a danger of short circuiting the anode and cathode, as it would happen in the conventional, planar device. Nevertheless, the pinholes give rise to a large number of unbounded perovskite ions, thus, increasing the amount of trap states, causing charge recombination. Further improvements in the efficiency of QIBC PSCs could come from improving the quality of the photoactive layer, possibly by utilising different methods of deposition. One potential technique could be

an evaporation of the perovskite layer, which usually results in more conformal coverage and larger perovskite grains.

Furthermore, simulations performed by Behrouznejad *et al.* [174] show that replacing Al/Ni comb-shaped electrode with a gold one would have a beneficial effect on the charge collection from the perovskite devices. This is caused by the superior conductivity of gold and the fact that its work function is in a better alignment with $MAPbI_3$. The reason for choosing the Al/Ni electrodes is the ease of thermal annealing, leading to the creation of a NiO_X HSL. Replacing it with gold would require the electrochemical deposition of a HSL or a modification of the gold work function at its surface, as reported by Lin *et al.* [185]

The increase in power conversion efficiency is naturally one of the main areas of interest of the BC PSCs field. Different strategies developed in this Thesis may serve as a guideline to achieve this goal. The *in situ* experiments in Chapter 4 were performed on $MAPbI_3$, the most widely studied of all PV perovskites. However, methods developed in this Chapter can be used to examine other PV materials. Performing such experiments should lead to a faster optimisation of the annealing parameters and minimising the time spent on developing new deposition methods of photoactive layers. Similarly, the pilot plant developed in Chapter 5 can be used for experiments with other types of PV perovskites, as well as other types of reagents.

The antireflective properties of PMMA presented in Chapter 6 are attributed to its refractive index, which lies between the refractive indices of air and perovskite. The polymer was chosen for the purpose of the experiments due to its chemical compatibility with the underlying perovskite layer and its ease of deposition. However, multiple polymers could potentially be applied as ARC on BC PSCs as a single layer, or even in conjunction with other polymers, creating a multilayer ARC of a gradually increasing refractive index.

The studies performed for the purpose of this Thesis have the potential to significantly contribute to the field of PSCs. By exploring the benefits of the BC architecture, one can perform experiments which are impossible with the planar devices. This Thesis serves as an evidence that QIBC electrodes are a useful tool on the path to commercialising perovskite solar cells.

8. References

[1] M. R. Allen, O. P. Dube, and W. Solecki, “2018: Framing and Context. In: Global Warming of 1.5°C. An IPCC Special Report on the impacts of global warming of 1.5°C above pre-industrial levels and related global greenhouse gas emission pathways, in the context of strengthening the global response t,” *InPress.*, pp. 49–91, 2019.

[2] E. Hawkins *et al.*, “Estimating changes in global temperature since the pre-industrial period,” *Bull. Am. Meteorol. Soc.*, vol. 98, no. September, pp. 1841–1856, 2017.

[3] J. Hansen, R. Ruedy, M. Sato, and K. Lo, “Global surface temperature change,” *Rev. Geophys.*, vol. 48, no. 4, pp. 1–29, 2010.

[4] R. S. Vose *et al.*, “Noaa’s merged land-ocean surface temperature analysis,” *Bull. Am. Meteorol. Soc.*, vol. 93, no. 11, pp. 1677–1685, 2012.

[5] C. P. Morice, J. J. Kennedy, N. A. Rayner, and P. D. Jones, “Quantifying uncertainties in global and regional temperature change using an ensemble of observational estimates: The HadCRUT4 data set,” *J. Geophys. Res. Atmos.*, vol. 117, no. 8, pp. 1–22, 2012.

[6] T. R. Karl *et al.*, “Possible artifacts of data biases in the recent global surface warming hiatus,” *Science (80-.).*, vol. 348, no. 6242, pp. 1469–1472, 2015.

[7] K. Cowtan and R. G. Way, “Coverage bias in the HadCRUT4 temperature series and its impact on recent temperature trends,” *Q. J. R. Meteorol. Soc.*, vol. 140, no. 683, pp. 1935–1944, 2014.

[8] IPCC, “AR5 - Working Group 3, Mitigation of Climate Change - Contribution of Working Group III,” Cambridge, United Kingdom and New York, NY, USA, 2014.

[9] M. Muntean *et al.*, “Fossil CO_2 emissions of all world countries - 2018 report,” *Eur 29433 En*, 2018.

[10] J. G. J. Olivier, K. M. Schure, and J. A. H. W. Peters, “Trends in Global CO_2 and Total Greenhouse Gas Emissions,” *PBL Netherlands Environ. Assess. Agency*, no. September 2017, 2017.

[11] G. Janssens-Maenhout *et al.*, “EDGAR v4.3.2 Global Atlas of the three major greenhouse gas emissions for the period 1970-2012,” *Earth Syst. Sci. Data*, vol. 11, no. 3, pp. 959–1002, 2019.

[12] R. A. Houghton and A. A. Nassikas, “Global and regional fluxes of carbon from land use and land cover change 1850–2015,” *Global Biogeochem. Cycles*, vol. 31, no. 3, pp. 456–472, 2017.

[13] R. Etkins and E. S. Epstein, “Rise of Global Mean Sea Level As an Indication of Climate Change.,” *Am. Assoc. Adv. Sci.*, vol. 215, no. 4530, pp. 343–359, 1982.

[14] M. Vermeer and S. Rahmstorf, “Global sea level linked to global temperature,” *Proc. Natl. Acad. Sci. U. S. A.*, vol. 106, no. 51, pp. 21527–21532, 2009.

[15] J. Hunter, I. Allison, and T. Jakszewicz, “Sea-Level Rise 2012,” *Antarctic Climate & Ecosystems Cooperative Research Centre*. Hobart, pp. 1–24, 2012.

[16] A. Cazenave and R. S. Nerem, “Present day sea level change: observations and causes,” *Rev. Geophys.*, vol. 42, pp. 1–20, 2004.

[17] H. B. Dieng, A. Cazenave, B. Meyssignac, and M. Ablain, “New estimate of the current rate of sea level rise from a sea level budget approach,” *Geophys. Res. Lett.*, vol. 44, no. 8, pp. 3744–3751, 2017.

[18] K. K. Rigaud *et al.*, “Groundswell - Preparing for internal climate migration,” *Washington, DC World Bank*, p. 256, 2018.

[19] IPCC, “WG2AR5 Chapt 19_Emergent Risks and Key Vulnerabilities,” *Cambridge Univ. Press*, pp. 1039–1099, 2014.

[20] J. C. Orr *et al.*, “Anthropogenic ocean acidification over the twenty-first century and its impact on calcifying organisms,” *Nature*, vol. 437, no. 7059, pp. 681–686, 2005.

[21] T. Jiang *et al.*, “Practical approach of a simulation system using different model basis,” *2017 IEEE PES Innov. Smart Grid Technol. Conf. Eur. ISGT-Europe 2017 - Proc.*, vol. 2018-Janua, pp. 1–6, 2018.

[22] O. Hoegh-Guldberg *et al.*, “Coral reefs under rapid climate change and ocean acidification.,” *Science*, vol. 318, no. 5857, pp. 1737–1742, Dec. 2007.

[23] O. Hoegh-Guldberg *et al.*, “Chapter 7. The oceans,” *Tetrahedron Org. Chem. Ser.*, vol. 21, no. C, pp. 35–60, 2002.

[24] L. V. Weatherdon, A. K. Magnan, A. D. Rogers, U. R. Sumaila, and W. W. L. L. Cheung, “Observed and Projected Impacts of Climate Change on Marine Fisheries, Aquaculture, Coastal Tourism, and Human Health: An Update,” *Front. Mar. Sci.*, vol. 3, no. 48, pp. 1–21, Apr. 2016.

[25] C. Parmesan, “Ecological and Evolutionary Responses to Recent Climate

Change," *Annu. Rev. Ecol. Evol. Syst.*, vol. 37, no. 1, pp. 637–669, Dec. 2006.

[26] A. E. Cahill *et al.*, "How does climate change cause extinction?," *Proc. R. Soc. B Biol. Sci.*, vol. 280, no. 1750, pp. 1–9, Nov. 2013.

[27] W. Thuiller, S. Lavorel, M. B. Araújo, M. T. Sykes, and I. C. Prentice, "Climate change threats to plant diversity in Europe," *Proc. Natl. Acad. Sci. U. S. A.*, vol. 102, no. 23, pp. 8245–8250, Jun. 2005.

[28] C. D. Thomas *et al.*, "Extinction risk from climate change," *Nature*, vol. 427, no. 6970, pp. 145–148, Jan. 2004.

[29] C. Parmesan and G. Yohe, "A globally coherent fingerprint of climate change impacts across natural systems," *Nature*, vol. 421, pp. 37–42, Jan. 2003.

[30] I. C. Chen, J. K. Hill, R. Ohlemüller, D. B. Roy, and C. D. Thomas, "Rapid range shifts of species associated with high levels of climate warming," *Science (80-.).*, vol. 333, no. 6045, pp. 1024–1026, Aug. 2011.

[31] K. D. Tape, D. D. Gustine, R. W. Ruess, L. G. Adams, and J. A. Clark, "Correction: Range expansion of moose in Arctic Alaska linked to warming and increased shrub habitat," *PLoS One*, vol. 11, no. 7, pp. 1–12, Apr. 2016.

[32] K. D. Tape, K. Christie, G. Carroll, and J. A. O'Donnell, "Novel wildlife in the Arctic: The influence of changing riparian ecosystems and shrub habitat expansion on snowshoe hares," *Glob. Chang. Biol.*, vol. 22, no. 1, pp. 208–219, Jan. 2016.

[33] G. T. Pecl *et al.*, "Biodiversity redistribution under climate change: Impacts on ecosystems and human well-being," *Science (80-.).*, vol. 355, no. 6332, pp. 1–9, Mar. 2017.

[34] A. S. Siraj, M. Santos-Vega, M. J. Bouma, D. Yadeta, D. Ruiz Carrascal, and M. Pascual, "Altitudinal changes in malaria incidence in highlands of Ethiopia and Colombia," *Science (80-.).*, vol. 343, no. 6175, pp. 1154–1158, Mar. 2014.

[35] B. H. Kaffenberger, D. Shetlar, S. A. Norton, and M. Rosenbach, "The effect of climate change on skin disease in North America," *J. Am. Acad. Dermatol.*, vol. 76, no. 1, pp. 140–147, Jan. 2017.

[36] N. Tokarevich, A. Tronin, B. Gnativ, B. Revich, O. Blinova, and B. Evengard, "Impact of air temperature variation on the ixodid ticks habitat and tick-borne encephalitis incidence in the Russian Arctic: The case of the Komi Republic," *Int. J. Circumpolar Health*, vol. 76, no. 1, pp. 1–13, Jan. 2017.

[37] M. Furberg, "Towards the Limits – Climate Change Aspects of Life and Health

in Northern Sweden: Studies of tularemia and regional experiences of changes in the environment," *Dep. Public Heal. Clin. Med. Epidemiol. Glob. Heal. Dep. Clin. Microbiol. Infect. Dis.*, p. 70, 2016.

[38] H. S. Baker *et al.*, "Higher CO_2 concentrations increase extreme event risk in a 1.5 °c world," *Nat. Clim. Chang.*, vol. 8, no. 7, pp. 604–608, Jul. 2018.

[39] F. E. Hoegh-Guldberg, O., D. Jacob, M. Taylor, M. Bindi, S. Brown, I. Camilloni, A. Diedhiou, R. Djalante, K.L. Ebi and and G. Z. J.Guiot, Y. Hijioka, S. Mehrotra, A. Payne, S.I. Seneviratne, A. Thomas, R. Warren, "Impacts of 1.5ºC Global Warming on Natural and Human Systems. In: Global Warming of 1.5°C. An IPCC Special Report on the impacts of global warming of 1.5°C above pre-industrial levels and related global greenhouse gas emission pathways, in the context of ," *Glob. Warm. 1.5°C. An IPCC Spec. Rep. impacts Glob. Warm. 1.5°C above pre-industrial levels Relat. Glob. Greenh. gas Emiss. pathways, Context Strength. Glob. response to Threat Clim. Chang.*, pp. 175–311, 2018.

[40] P. Forman, "The primacy of science in modernity, of technology in postmodernity, and of ideology in the history of technology," *Hist. Technol.*, vol. 23, no. 1–2, pp. 1–152, 2007.

[41] D. P. van Vuuren *et al.*, "The representative concentration pathways: An overview," *Clim. Change*, vol. 109, no. 1, pp. 5–31, Nov. 2011.

[42] R. Collins, M. *et al.*, "Long-term climate change: Projections, commitments and irreversibility," *Clim. Chang. 2013 Phys. Sci. Basis Work. Gr. I Contrib. to Fifth Assess. Rep. Intergov. Panel Clim. Chang.*, vol. 9781107057, pp. 1029–1136, 2013.

[43] O. Edenhofer *et al.*, "Technical Summary- IPCC," *Clim. Chang. 2014 Mitig. Clim. Chang. Contrib. Work. Gr. III to Fifth Assess. Rep. Intergov. Panel Clim. Chang.*, pp. 33–107, 2014.

[44] H. Ritchie and M. Roser, "CO_2 and other Greenhouse Gas Emissions. Published online at OurWorldInData.org," *OurWorldInData.org.*, 2019. [Online]. Available: https://ourworldindata.org/co2-and-other-greenhouse-gas-emissions. [Accessed: 11-Feb-2019].

[45] Energy Information Administration, "International Energy Statistics: Imports," 2013. [Online]. Available: http://www.eia.gov/cfapps/ipdbproject/iedindex3.cfm?tid=5&pid=57&aid=3&cid

=r6,&syid=2009&eyid=2013&unit=TBPD. [Accessed: 11-Feb-2019].

[46] B. Nykvist, F. Sprei, and M. Nilsson, “Assessing the progress toward lower priced long range battery electric vehicles,” *Energy Policy*, vol. 124, pp. 144–155, 2019.

[47] J. H. Williams *et al.*, “The technology path to deep greenhouse gas emissions cuts by 2050: The pivotal role of electricity,” *Science (80-.).*, vol. 335, no. 6064, pp. 53–59, Jan. 2012.

[48] K. P. Bhandari, J. M. Collier, R. J. Ellingson, and D. S. Apul, “Energy payback time (EPBT) and energy return on energy invested (EROI) of solar photovoltaic systems: A systematic review and meta-analysis,” *Renew. Sustain. Energy Rev.*, vol. 47, pp. 133–141, Jul. 2015.

[49] M. J. De Wild-Scholten, “Energy payback time and carbon footprint of commercial photovoltaic systems,” *Sol. Energy Mater. Sol. Cells*, vol. 119, pp. 296–305, Dec. 2013.

[50] M. Raugei, S. Bargigli, and S. Ulgiati, “Life cycle assessment and energy pay-back time of advanced photovoltaic modules: CdTe and CIS compared to poly-Si,” *Energy*, vol. 32, no. 8, pp. 1310–1318, Aug. 2007.

[51] V. M. Fthenakis and H. C. Kim, “Greenhouse-gas emissions from solar electric- and nuclear power: A life-cycle study,” *Energy Policy*, vol. 35, no. 4, pp. 2549–2557, Apr. 2007.

[52] N. Stylos and C. Koroneos, “Carbon footprint of polycrystalline photovoltaic systems,” *J. Clean. Prod.*, vol. 64, pp. 639–645, Feb. 2014.

[53] H. Hondo, “Life cycle GHG emission analysis of power generation systems: Japanese case,” *Energy*, vol. 30, no. 11-12 SPEC. ISS., pp. 2042–2056, Aug. 2005.

[54] S. W. White and G. L. Kulcinski, “Birth to death analysis of the energy payback ratio and CO_2 gas emission rates from coal, fission, wind, and DT-fusion electrical power plants,” *Fusion Eng. Des.*, vol. 48, no. 3, pp. 473–481, Sep. 2000.

[55] P. Viebahn *et al.*, “Comparison of carbon capture and storage with renewable energy technologies regarding structural, economic, and ecological aspects in Germany,” *Int. J. Greenh. Gas Control*, vol. 1, no. 1, pp. 121–133, Apr. 2007.

[56] N. A. Odeh and T. T. Cockerill, “Life cycle GHG assessment of fossil fuel power plants with carbon capture and storage,” *Energy Policy*, vol. 36, no. 1,

pp. 367–380, Jan. 2008.

[57] N. A. Odeh and T. T. Cockerill, “Life cycle analysis of UK coal fired power plants,” *Energy Convers. Manag.*, vol. 49, no. 2, pp. 212–220, Feb. 2008.

[58] R. Dones, T. Heck, M. F. Emmenegger, and N. Jungbluth, “Life cycle inventories for the nuclear and natural gas energy systems, and examples of uncertainty analysis,” *Int. J. Life Cycle Assess.*, vol. 10, no. 1, pp. 10–23, Jan. 2005.

[59] W. H. Schlesinger, “Are wood pellets a green fuel?,” *Science (80-.).*, vol. 359, no. 6382, pp. 1328–1329, Mar. 2018.

[60] J. G. Canadell and M. R. Raupach, “Managing forests for climate change mitigation,” *Science (80-.).*, vol. 320, no. 5882, pp. 1456–1457, 2008.

[61] W. H. Schlesinger and E. S. Bernhardt, *Biogeochemistry: An Analysis of Global Change, Third Edition*, 3rd ed. Academic Press, 2013.

[62] J. Kantenbacher, “Renewable Energy,” *Sustainable Communities Design Handbook*, 2010. [Online]. Available: https://ourworldindata.org/renewable-energy. [Accessed: 12-Feb-2019].

[63] H. A. Aulich and F. W. Schulze, “Crystalline silicon feedstock for solar cells,” *Prog. Photovoltaics Res. Appl.*, vol. 10, no. 2, pp. 141–147, Mar. 2002.

[64] UNFCCC, “Report of the Intergovernmental Negotiating Committee for a Framework Convention on Climate Change on the work of the second part of its fifth session, held at New York from 30 April to 9 May 1992. Addendum: A/AC.237/18 (Part II)/Add.1,” *FCCC/INFORMAL/84 GE.05-62220 (E) 200705*, 1992.

[65] UNFCCC, “United Nations Treaty Collection: Status of Paris Agreement.” [Online]. Available: https://treaties.un.org/Pages/ViewDetails.aspx?src=TREATY&mtdsg_no=XXVII-7-d&chapter=27&clang=_en#1.

[66] R. Webster, “Will the Paris climate deal be legally binding? ,” *Road to Paris*, 2015.

[67] M. A. Green, E. D. Dunlop, D. H. Levi, J. Hohl-Ebinger, M. Yoshita, and A. W. Y. Ho-Baillie, “Solar cell efficiency tables (version 54),” *Prog. Photovoltaics Res. Appl.*, vol. 27, no. 7, pp. 565–575, Jan. 2019.

[68] K. Yoshikawa *et al.*, “Silicon heterojunction solar cell with interdigitated back contacts for a photoconversion efficiency over 26%,” *Nat. Energy*, vol. 2, no. 5,

p. 17032, Mar. 2017.

[69] A. Slade and V. Garboushian, “27.6% efficient silicon concentrator cell for mass production,” *Tech. Dig. 15th Int. Photovolt. Sci. Eng. Conf. Shanghai*, vol. 701, 2005.

[70] W. Shockley and H. J. Queisser, “Detailed balance limit of efficiency of p-n junction solar cells,” *J. Appl. Phys.*, vol. 32, no. 3, pp. 510–519, Mar. 1961.

[71] S. Rühle, “Tabulated values of the Shockley-Queisser limit for single junction solar cells,” *Sol. Energy*, vol. 130, pp. 139–147, Jun. 2016.

[72] F. Dimroth *et al.*, “Four-junction wafer-bonded concentrator solar cells,” *IEEE J. Photovoltaics*, vol. 6, no. 1, pp. 343–349, Jan. 2016.

[73] A. De Vos, “Detailed balance limit of the efficiency of tandem solar cells,” *J. Phys. D. Appl. Phys.*, vol. 13, no. 5, pp. 839–846, 1980.

[74] B. J. Stanbery, “Copper indium selenides and related materials for photovoltaic devices,” *Crit. Rev. Solid State Mater. Sci.*, vol. 27, no. 2, pp. 73–117, Apr. 2002.

[75] J. S. Ward *et al.*, “A 21.5% efficient Cu(In,Ga)Se_2 thin-film concentrator solar cell,” *Prog. Photovoltaics Res. Appl.*, vol. 10, no. 1, pp. 41–46, Jan. 2002.

[76] J. L. Wu, Y. Hirai, T. Kato, H. Sugimoto, and V. Bermudez, “New world record efficiency up to 22.9% for Cu(In, Ga)(Se, $S)_2$ thin-film solar cells,” *7th World Conf. Photovolt. Energy Convers.*, pp. 10–15, 2018.

[77] N. G. Dhere, “Scale-up issues of CIGS thin film PV modules,” *Sol. Energy Mater. Sol. Cells*, vol. 95, no. 1, pp. 277–280, Jan. 2011.

[78] I. Repins, S. Glynn, J. Duenow, T. J. Coutts, W. K. Metzger, and M. A. Contreras, “Required material properties for high-efficiency CIGS modules,” *Soc. Photogr. Instrum. Eng. 2009 Sol. Energy + Technol. Conf.*, vol. 7409, no. July, p. 74090M, Aug. 2009.

[79] Y. Cao, Y. Liu, S. M. Zakeeruddin, A. Hagfeldt, and M. Grätzel, “Direct Contact of Selective Charge Extraction Layers Enables High-Efficiency Molecular Photovoltaics,” *Joule*, vol. 2, no. 6, pp. 1108–1117, Jun. 2018.

[80] A. Kojima, K. Teshima, Y. Shirai, and T. Miyasaka, “Organometal halide perovskites as visible-light sensitizers for photovoltaic cells,” *J. Am. Chem. Soc.*, vol. 131, no. 17, pp. 6050–6051, May 2009.

[81] J. P. Correa-Baena *et al.*, “The rapid evolution of highly efficient perovskite solar cells,” *Energy Environ. Sci.*, vol. 10, no. 3, pp. 710–727, 2017.

[82] R. Coontz, “Science’s Top 10 Breakthroughs of 2013,” *Science (New York, N.Y.)*, 2013. [Online]. Available: www.sciencedaily.com/releases/2013/12/131219142223.htm. [Accessed: 19-Feb-2019].

[83] “365 days: Nature’s 10,” *Nature*, vol. 504, no. 7480, pp. 357–365, Dec. 2013.

[84] NREL, “Solar cell research efficiency chart,” *Solar cell efficiency chart*, 2019. [Online]. Available: http://www.nrel.gov/ncpv/images/efficiency_chart.jpg. [Accessed: 18-Aug-2019].

[85] T. Sherahilo, “Oxford PV perovskite solar cell achieves 28% efficiency,” *Oxfort PV*, 2018. [Online]. Available: https://www.oxfordpv.com/news/oxford-pv-perovskite-solar-cell-achieves-28-efficiency. [Accessed: 19-Feb-2019].

[86] Microquanta, “17.9% Microquanta set new world record for perovskite solar mini-mudule,” 2018. [Online]. Available: http://www.microquanta.com/en/newsinfo/B204B496727A58F3/. [Accessed: 20-Feb-2019].

[87] F. De Angelis, “Celebrating 10 years of perovskite photovoltaics,” *ACS Energy Lett.*, vol. 4, no. 4, pp. 853–854, 2019.

[88] C. Li, X. Lu, W. Ding, L. Feng, Y. Gao, and Z. Guo, “Formability of ABX_3 (X = F, Cl, Br, I) halide perovskites,” *Acta Crystallogr. Sect. B Struct. Sci.*, vol. 64, no. 6, pp. 702–707, Dec. 2008.

[89] V. M. Goldschmidt, “Die Gesetze der Krystallochemie,” *Naturwissenschaften*, vol. 14, no. 21, pp. 477–485, 1926.

[90] C. Li, K. C. K. Soh, and P. Wu, “Formability of ABO_3 perovskites,” *J. Alloys Compd.*, vol. 372, no. 1–2, pp. 40–48, Jun. 2004.

[91] Q. Chen *et al.*, “Under the spotlight: The organic-inorganic hybrid halide perovskite for optoelectronic applications,” *Nano Today*, vol. 10, no. 3, pp. 355–396, Jun. 2015.

[92] M. A. Green, A. Ho-Baillie, and H. J. Snaith, “The emergence of perovskite solar cells,” *Nat. Photonics*, vol. 8, no. 7, pp. 506–514, Jul. 2014.

[93] Z. Li, M. Yang, J. S. Park, S. H. Wei, J. J. Berry, and K. Zhu, “Stabilizing Perovskite Structures by Tuning Tolerance Factor: Formation of Formamidinium and Cesium Lead Iodide Solid-State Alloys,” *Chem. Mater.*, vol. 28, no. 1, pp. 284–292, Jan. 2016.

[94] A. Poglitsch and D. Weber, “Dynamic disorder in

methylammoniumtrihalogenoplumbates (II) observed by millimeter-wave spectroscopy," *J. Chem. Phys.*, vol. 87, no. 11, pp. 6373–6378, 1987.

[95] M. D. Smirnova *et al.*, "Health effects of hot summer weather in patients with intermediate and high cardiovascular risk," *Cardiovasc. Ther. Prev. (Russian Fed.*, vol. 12, no. 4, pp. 56–61, 2013.

[96] W. Geng, L. Zhang, Y. N. Zhang, W. M. Lau, and L. M. Liu, "First-principles study of lead iodide perovskite tetragonal and orthorhombic phases for photovoltaics," *J. Phys. Chem. C*, vol. 118, no. 34, pp. 19565–19571, 2014.

[97] N. G. Park, "Perovskite solar cells: An emerging photovoltaic technology," *Mater. Today*, vol. 18, no. 2, pp. 65–72, Mar. 2015.

[98] G. E. Eperon, S. D. Stranks, C. Menelaou, M. B. Johnston, L. M. Herz, and H. J. Snaith, "Formamidinium lead trihalide: A broadly tunable perovskite for efficient planar heterojunction solar cells," *Energy Environ. Sci.*, vol. 7, no. 3, pp. 982–988, 2014.

[99] J. C. Slater, "Atomic radii in crystals," *J. Chem. Phys.*, vol. 41, no. 10, pp. 3199–3204, Nov. 1964.

[100] F. Hao, C. C. Stoumpos, D. H. Cao, R. P. H. Chang, and M. G. Kanatzidis, "Lead-free solid-state organic-inorganic halide perovskite solar cells," *Nat. Photonics*, vol. 8, no. 6, pp. 489–494, Jun. 2014.

[101] F. Hao, C. C. Stoumpos, R. P. H. Chang, and M. G. Kanatzidis, "Anomalous band gap behavior in mixed Sn and Pb perovskites enables broadening of absorption spectrum in solar cells," *J. Am. Chem. Soc.*, vol. 136, no. 22, pp. 8094–8099, Jun. 2014.

[102] K. T. Butler, J. M. Frost, and A. Walsh, "Band alignment of the hybrid halide perovskites $CH_3NH_3PbCl_3$, $CH_3NH_3PbBr_3$ and $CH_3NH_3PbI_3$," *Mater. Horizons*, vol. 2, no. 2, pp. 228–231, 2015.

[103] N. Pellet *et al.*, "Mixed-organic-cation perovskite photovoltaics for enhanced solar-light harvesting," *Angew. Chemie - Int. Ed.*, vol. 53, no. 12, pp. 3151–3157, Mar. 2014.

[104] A. R. B. M. Yusoff and M. K. Nazeeruddin, "Organohalide Lead Perovskites for Photovoltaic Applications," *J. Phys. Chem. Lett.*, vol. 7, no. 5, pp. 851–866, 2016.

[105] V. A. Online, P. Gao, and M. K. Nazeeruddin, "Environmental Science Organohalide lead perovskites for photovoltaic," *Energy Environ. Sci.*, vol. 1,

no. c, pp. 2448–2463, 2014.

[106] D. B. Mitzi, “Synthesis, structure, and properties of organic-inorganic perovskites and related materials,” in *Progress in Inorganic Chemistry*, vol. 48, 2007, pp. 1–121.

[107] N. N. Lal, Y. Dkhissi, W. Li, Q. Hou, Y. B. Cheng, and U. Bach, “Perovskite Tandem Solar Cells,” *Adv. Energy Mater.*, vol. 7, no. 18, pp. 1–18, 2017.

[108] T. Jesper Jacobsson *et al.*, “Exploration of the compositional space for mixed lead halogen perovskites for high efficiency solar cells,” *Energy Environ. Sci.*, vol. 9, no. 5, pp. 1706–1724, 2016.

[109] A. Amat *et al.*, “Cation-induced band-gap tuning in organohalide perovskites: Interplay of spin-orbit coupling and octahedra tilting,” *Nano Lett.*, vol. 14, no. 6, pp. 3608–3616, 2014.

[110] S. De Wolf *et al.*, “Organometallic halide perovskites: Sharp optical absorption edge and its relation to photovoltaic performance,” *J. Phys. Chem. Lett.*, vol. 5, no. 6, pp. 1035–1039, 2014.

[111] G. E. Eperon *et al.*, “Perovskite-perovskite tandem photovoltaics with optimized band gaps,” *Science (80-.).*, vol. 354, no. 6314, pp. 861–865, 2016.

[112] J. Werner, B. Niesen, and C. Ballif, “Perovskite/Silicon Tandem Solar Cells: Marriage of Convenience or True Love Story? – An Overview,” *Adv. Mater. Interfaces*, vol. 5, no. 1, pp. 1–19, 2018.

[113] T. Duong *et al.*, “Rubidium Multication Perovskite with Optimized Bandgap for Perovskite-Silicon Tandem with over 26% Efficiency,” *Adv. Energy Mater.*, vol. 7, no. 14, pp. 1–11, 2017.

[114] E. T. Hoke, D. J. Slotcavage, E. R. Dohner, A. R. Bowring, H. I. Karunadasa, and M. D. McGehee, “Reversible photo-induced trap formation in mixed-halide hybrid perovskites for photovoltaics,” *Chem. Sci.*, vol. 6, no. 1, pp. 613–617, 2015.

[115] Y. Ogomi *et al.*, “$CH_3NH_3Sn_xPb_{(1-x)}I_3$ perovskite solar cells covering up to 1060 nm,” *J. Phys. Chem. Lett.*, vol. 5, no. 6, pp. 1004–1011, 2014.

[116] D. T. Moore *et al.*, “Crystallization kinetics of organic-inorganic trihalide perovskites and the role of the lead anion in crystal growth,” *J. Am. Chem. Soc.*, vol. 137, no. 6, pp. 2350–2358, Feb. 2015.

[117] U. Köster, “Crystallization of amorphous silicon films,” *Phys. Status Solidi*, vol. 48, no. 2, pp. 313–321, Aug. 1978.

[118] Q. Wang, Y. Shao, Q. Dong, Z. Xiao, Y. Yuan, and J. Huang, “Large fill-factor bilayer iodine perovskite solar cells fabricated by a low-temperature solution-process,” *Energy Environ. Sci.*, vol. 7, no. 7, pp. 2359–2365, 2014.

[119] K. Hwang *et al.*, “Toward large scale roll-to-roll production of fully printed perovskite solar cells,” *Adv. Mater.*, vol. 27, no. 7, pp. 1241–1247, 2015.

[120] J. Huang, Y. Yuan, Y. Shao, and Y. Yan, “Understanding the physical properties of hybrid perovskites for photovoltaic applications,” *Nat. Rev. Mater.*, vol. 2, no. 7, p. 17042, Jul. 2017.

[121] D. Shi *et al.*, “Low trap-state density and long carrier diffusion in organolead trihalide perovskite single crystals,” *Science (80-.).*, vol. 347, no. 6221, pp. 519–522, Jan. 2015.

[122] Q. Dong *et al.*, “Electron-hole diffusion lengths > 175 μm in solution-grown $CH_3NH_3PbI_3$ single crystals,” *Science (80-.).*, vol. 347, no. 6225, pp. 967–970, Feb. 2015.

[123] A. Miyata *et al.*, “Direct measurement of the exciton binding energy and effective masses for charge carriers in organic-inorganic tri-halide perovskites,” *Nat. Phys.*, vol. 11, no. 7, pp. 582–587, Jul. 2015.

[124] K. Tanaka, T. Takahashi, T. Ban, T. Kondo, K. Uchida, and N. Miura, “Comparative study on the excitons in lead-halide-based perovskite-type crystals $CH_3NH_3PbBr_3CH_3NH_3PbI_3$,” *Solid State Commun.*, vol. 127, no. 9–10, pp. 619–623, Sep. 2003.

[125] M. Hirasawa, T. Ishihara, T. Goto, K. Uchida, and N. Miura, “Magnetoabsorption of the lowest exciton in perovskite-type compound (CH3NH3)PbI3,” *Phys. B Phys. Condens. Matter*, vol. 201, no. C, pp. 427–430, Jul. 1994.

[126] V. D’Innocenzo *et al.*, “Excitons versus free charges in organo-lead tri-halide perovskites,” *Nat. Commun.*, vol. 5, no. 1, p. 3586, May 2014.

[127] N. C. Giebink, G. P. Wiederrecht, M. R. Wasielewski, and S. R. Forrest, “Thermodynamic efficiency limit of excitonic solar cells,” *Phys. Rev. B - Condens. Matter Mater. Phys.*, vol. 83, no. 19, p. 195326, May 2011.

[128] G. Xing *et al.*, “Long-range balanced electron-and hole-transport lengths in organic-inorganic $CH_3NH_3PbI_3$,” *Science (80-.).*, vol. 342, no. 6156, pp. 344–347, Oct. 2013.

[129] S. D. Stranks *et al.*, “Electron-hole diffusion lengths exceeding 1 micrometer in

an organometal trihalide perovskite absorber," *Science (80-.).*, vol. 342, no. 6156, pp. 341–344, 2013.

[130] M. Grätzel, "The light and shade of perovskite solar cells," *Nat. Mater.*, vol. 13, no. 9, pp. 838–842, Sep. 2014.

[131] H. Zhou *et al.*, "Interface engineering of highly efficient perovskite solar cells," *Science (80-.).*, vol. 345, no. 6196, pp. 542–546, Aug. 2014.

[132] H. S. Kim *et al.*, "Lead iodide perovskite sensitized all-solid-state submicron thin film mesoscopic solar cell with efficiency exceeding 9%," *Sci. Rep.*, vol. 2, no. 1, p. 591, Dec. 2012.

[133] C. C. Chueh, C. Z. Li, and A. K. Y. Jen, "Recent progress and perspective in solution-processed Interfacial materials for efficient and stable polymer and organometal perovskite solar cells," *Energy Environ. Sci.*, vol. 8, no. 4, pp. 1160–1189, 2015.

[134] Y. Zhao and K. Zhu, "Charge transport and recombination in perovskite (CH_3NH_3)PbI_3 sensitized TiO_2 Solar Cells," *J. Phys. Chem. Lett.*, vol. 4, no. 17, pp. 2880–2884, Sep. 2013.

[135] S. Ito *et al.*, "Fabrication of screen-printing pastes from TiO_2 powders for dye-sensitised solar cells," *Prog. Photovoltaics Res. Appl.*, vol. 15, no. 7, pp. 603–612, Nov. 2007.

[136] L. Kavan and M. Grätzel, "Highly efficient semiconducting TiO2 photoelectrodes prepared by aerosol pyrolysis," *Electrochim. Acta*, vol. 40, no. 5, pp. 643–652, Apr. 1995.

[137] J. Aarik, A. Aidla, T. Uustare, M. Ritala, and M. Leskelä, "Titanium isopropoxide as a precursor for atomic layer deposition: Characterization of titanium dioxide growth process," *Appl. Surf. Sci.*, vol. 161, no. 3, pp. 385–395, Jul. 2000.

[138] I. Jeong *et al.*, "A tailored TiO_2 electron selective layer for high-performance flexible perovskite solar cells via low temperature UV process," *Nano Energy*, vol. 28, pp. 380–389, Oct. 2016.

[139] A. N. Banerjee *et al.*, "Low-temperature deposition of ZnO thin films on PET and glass substrates by DC-sputtering technique," *Thin Solid Films*, vol. 496, no. 1, pp. 112–116, Feb. 2006.

[140] F. C. Krebs, T. Tromholt, and M. Jørgensen, "Upscaling of polymer solar cell fabrication using full roll-to-roll processing," *Nanoscale*, vol. 2, no. 6, pp. 873–

886, 2010.

[141] W. Ke *et al.*, “Lowerature solution-processed tin oxide as an alternative electron transporting layer for efficient perovskite solar cells,” *J. Am. Chem. Soc.*, vol. 137, no. 21, pp. 6730–6733, Jun. 2015.

[142] A. K. Chandiran, M. Abdi-Jalebi, M. K. Nazeeruddin, and M. Grätzel, “Analysis of electron transfer properties of ZnO and TiO_2 photoanodes for dye-sensitized solar cells,” *ACS Nano*, vol. 8, no. 3, pp. 2261–2268, 2014.

[143] Q. Zhang, C. S. Dandeneau, X. Zhou, and C. Cao, “ZnO nanostructures for dye-sensitized solar cells,” *Adv. Mater.*, vol. 21, no. 41, pp. 4087–4108, Nov. 2009.

[144] Q. Hu *et al.*, “Engineering of electron-selective contact for perovskite solar cells with efficiency exceeding 15%,” *ACS Nano*, vol. 8, no. 10, pp. 10161–10167, 2014.

[145] J. Yang, B. D. Siempelkamp, E. Mosconi, F. De Angelis, and T. L. Kelly, “Origin of the Thermal Instability in $CH_3NH_3PbI_3$ Thin Films Deposited on ZnO,” *Chem. Mater.*, vol. 27, no. 12, pp. 4229–4236, 2015.

[146] Y. Dkhissi *et al.*, “Stability Comparison of Perovskite Solar Cells Based on Zinc Oxide and Titania on Polymer Substrates,” *ChemSusChem*, vol. 9, no. 7, pp. 687–695, 2016.

[147] G. Yang, H. Tao, P. Qin, W. Ke, and G. Fang, “Recent progress in electron transport layers for efficient perovskite solar cells,” *J. Mater. Chem. A*, vol. 4, no. 11, pp. 3970–3990, 2016.

[148] E. H. Anaraki *et al.*, “Highly efficient and stable planar perovskite solar cells by solution-processed tin oxide,” *Energy Environ. Sci.*, vol. 9, no. 10, pp. 3128–3134, 2016.

[149] D. Liu and T. L. Kelly, “Perovskite solar cells with a planar heterojunction structure prepared using room-temperature solution processing techniques,” *Nat. Photonics*, vol. 8, no. 2, pp. 133–138, 2014.

[150] K. Mahmood, B. S. Swain, and A. Amassian, “16.1% Efficient Hysteresis-Free Mesostructured Perovskite Solar Cells Based on Synergistically Improved ZnO Nanorod Arrays,” *Adv. Energy Mater.*, vol. 5, no. 17, pp. 1–11, 2015.

[151] D. Yang *et al.*, “Stable Efficiency Exceeding 20.6% for Inverted Perovskite Solar Cells through Polymer-Optimized PCBM Electron-Transport Layers,” *Nano Lett.*, vol. 19, no. 5, pp. 3313–3320, 2019.

[152] Y. Zheng *et al.*, “Spray coating of the PCBM electron transport layer significantly improves the efficiency of p-i-n planar perovskite solar cells,” *Nanoscale*, vol. 10, no. 24, pp. 11342–11348, 2018.

[153] X. Liu *et al.*, “Triple cathode buffer layers composed of PCBM, C_{60}, and LiF for high-performance planar perovskite solar cells,” *ACS Appl. Mater. Interfaces*, vol. 7, no. 11, pp. 6230–6237, Mar. 2015.

[154] D. Liu *et al.*, “Aqueous-Containing Precursor Solutions for Efficient Perovskite Solar Cells,” *Adv. Sci.*, vol. 5, no. 1, 2018.

[155] U. Bach *et al.*, “Solid-state dye-sensitized mesoporous TiO_2 solar cells with high photon-to-electron conversion efficiencies,” *Nature*, vol. 395, no. 6702, pp. 583–585, Oct. 1998.

[156] N. J. Jeon *et al.*, “O-methoxy substituents in spiro-OMeTAD for efficient inorganic-organic hybrid perovskite solar cells,” *J. Am. Chem. Soc.*, vol. 136, no. 22, pp. 7837–7840, 2014.

[157] Z. Hawash, L. K. Ono, and Y. Qi, “Photovoltaics: Moisture and Oxygen Enhance Conductivity of LiTFSI-Doped Spiro-MeOTAD Hole Transport Layer in Perovskite Solar Cells (Adv. Mater. Interfaces 13/2016),” *Adv. Mater. Interfaces*, vol. 3, no. 13, p. 1600117, Jul. 2016.

[158] M. Salado *et al.*, “Impact of moisture on efficiency-determining electronic processes in perovskite solar cells,” *J. Mater. Chem. A*, vol. 5, no. 22, pp. 10917–10927, 2017.

[159] W. S. Yang *et al.*, “High-performance photovoltaic perovskite layers fabricated through intramolecular exchange,” *Science (80-.).*, vol. 348, no. 6240, pp. 1234–1237, Jun. 2015.

[160] P. Docampo, J. M. Ball, M. Darwich, G. E. Eperon, and H. J. Snaith, “Efficient organometal trihalide perovskite planar-heterojunction solar cells on flexible polymer substrates,” *Nat. Commun.*, vol. 4, no. 1, p. 2761, Dec. 2013.

[161] Y. Zhu, S. Wang, R. Ma, and C. Wang, “The improvement of inverted perovskite solar cells by the introduction of CTAB into PEDOT:PSS,” *Sol. Energy*, vol. 188, no. February, pp. 28–34, Aug. 2019.

[162] Q. Wang, C. C. Chueh, M. Eslamian, and A. K. Y. Jen, “Modulation of PEDOT:PSS pH for efficient inverted perovskite solar cells with reduced potential loss and enhanced stability,” *ACS Appl. Mater. Interfaces*, vol. 8, no. 46, pp. 32068–32076, 2016.

[163] J. Liu *et al.*, “Employing PEDOT as the p-type charge collection layer in regular organic-inorganic perovskite solar cells,” *J. Phys. Chem. Lett.*, vol. 6, no. 9, pp. 1666–1673, May 2015.

[164] C. Chappaz-Gillot, R. Salazar, S. Berson, and V. Ivanova, “Room temperature template-free electrodeposition of CuSCN nanowires,” *Electrochem. commun.*, vol. 24, no. 1, pp. 1–4, Oct. 2012.

[165] C. Chappaz-Gillot, R. Salazar, S. Berson, and V. Ivanova, “Insights into CuSCN nanowire electrodeposition on flexible substrates,” *Electrochim. Acta*, vol. 110, pp. 375–381, Nov. 2013.

[166] W. Yu *et al.*, “Ultrathin Cu_2O as an efficient inorganic hole transporting material for perovskite solar cells,” *Nanoscale*, vol. 8, no. 11, pp. 6173–6179, 2016.

[167] W. C. Lai, K. W. Lin, Y. T. Wang, T. Y. Chiang, P. Chen, and T. F. Guo, “Oxidized Ni/Au Transparent Electrode in Efficient $CH_3NH_3PbI_3$ Perovskite/Fullerene Planar Heterojunction Hybrid Solar Cells,” *Adv. Mater.*, vol. 28, no. 17, pp. 3290–3297, May 2016.

[168] S. Ito, S. Tanaka, and H. Nishino, “Lead-halide perovskite solar cells by CH_3NH_3I dripping on PbI_2-CH_3NH_3I-DMSO precursor layer for planar and porous structures using CuSCN hole-transporting material,” *J. Phys. Chem. Lett.*, vol. 6, no. 5, pp. 881–886, Mar. 2015.

[169] G. A. Sepalage *et al.*, “Copper(I) Iodide as Hole-Conductor in Planar Perovskite Solar Cells: Probing the Origin of J-V Hysteresis,” *Adv. Funct. Mater.*, vol. 25, no. 35, pp. 5650–5661, Sep. 2015.

[170] J. Liu *et al.*, “Novel low cost hole transporting materials for efficient organic-inorganic perovskite solar cells,” in *2015 IEEE 42nd Photovoltaic Specialist Conference, PVSC 2015*, 2015, pp. 1–4.

[171] K. C. Wang *et al.*, “Low-temperature sputtered nickel oxide compact thin film as effective electron blocking layer for mesoscopic NiO/$CH_3NH_3PbI_3$ perovskite heterojunction solar cells,” *ACS Appl. Mater. Interfaces*, vol. 6, no. 15, pp. 11851–11858, Aug. 2014.

[172] V. E. Madhavan *et al.*, “Copper Thiocyanate Inorganic Hole-Transporting Material for High-Efficiency Perovskite Solar Cells,” *ACS Energy Lett.*, vol. 1, no. 6, pp. 1112–1117, 2016.

[173] C. Zuo and L. Ding, “Solution-Processed Cu_2O and CuO as Hole Transport Materials for Efficient Perovskite Solar Cells,” *Small*, vol. 11, no. 41, pp. 5528–

5532, 2015.

[174] F. Behrouznejad, S. Shahbazi, N. Taghavinia, H. P. Wu, and E. Wei-Guang Diau, “A study on utilizing different metals as the back contact of $CH_3NH_3PbI_3$ perovskite solar cells,” *J. Mater. Chem. A*, vol. 4, no. 35, pp. 13488–13498, 2016.

[175] M. M. Lee, J. Teuscher, T. Miyasaka, T. N. Murakami, and H. J. Snaith, “Efficient hybrid solar cells based on meso-superstructured organometal halide perovskites,” *Science (80-.).*, vol. 338, no. 6107, pp. 643–647, Nov. 2012.

[176] A. R. Pascoe *et al.*, “Planar versus mesoscopic perovskite microstructures: The influence of $CH_3NH_3PbI_3$ morphology on charge transport and recombination dynamics,” *Nano Energy*, vol. 22, pp. 439–452, Apr. 2016.

[177] J.-H. Im, C.-R. Lee, J.-W. Lee, S.-W. Park, and N.-G. Park, “6.5% efficient perovskite quantum-dot-sensitized solar cell,” *Nanoscale*, vol. 3, no. 10, p. 4088, 2011.

[178] H. S. Jung and N.-G. G. Park, “Perovskite Solar Cells: From Materials to Devices,” *Small*, vol. 11, no. 1, pp. 10–25, Jan. 2015.

[179] T. Minemoto and M. Murata, “Device modeling of perovskite solar cells based on structural similarity with thin film inorganic semiconductor solar cells,” *J. Appl. Phys.*, vol. 116, no. 5, 2014.

[180] E. Della Gaspera *et al.*, “Ultra-thin high efficiency semitransparent perovskite solar cells,” *Nano Energy*, vol. 13, pp. 249–257, Apr. 2015.

[181] R. J. J. Schwartz and M. D. Lammert, “Silicon solar cells for high concentration applications,” *1975 Int. Electron Devices Meet.*, vol. 21, pp. 350–352, 2008.

[182] E. Van Kerschaver and G. Beaucarne, “Back-contact solar cells: A review,” *Prog. Photovoltaics Res. Appl.*, vol. 14, no. 2, pp. 107–123, 2006.

[183] P. J. Verlinden, R. M. Swanson, and R. A. Crane, “7000 high-eficiency cells for a dream,” *Prog. Photovoltaics Res. Appl.*, vol. 2, no. 2, pp. 143–152, Apr. 1994.

[184] D. Fu, X. Li Zhang, R. L. Barber, and U. Bach, “Dye-sensitized back-contact solar cells,” *Adv. Mater.*, vol. 22, no. 38, pp. 4270–4274, Oct. 2010.

[185] X. Lin *et al.*, “Dipole-field-assisted charge extraction in metal-perovskite-metal back-contact solar cells,” *Nat. Commun.*, vol. 8, no. 1, pp. 1–8, Dec. 2017.

[186] L. M. Pazos-Outón *et al.*, “Photon recycling in lead iodide perovskite solar cells,” *Science (80-.).*, vol. 351, no. 6280, pp. 1430–1433, Mar. 2016.

[187] M. Alsari *et al.*, “In situ simultaneous photovoltaic and structural evolution of perovskite solar cells during film formation,” *Energy Environ. Sci.*, vol. 11, no. 2, pp. 383–393, 2018.

[188] A. N. Jumabekov *et al.*, “Back-contacted hybrid organic-inorganic perovskite solar cells,” *J. Mater. Chem. C*, vol. 4, no. 15, pp. 3125–3130, 2016.

[189] T. Ma, Q. Song, D. Tadaki, M. Niwano, and A. Hirano-Iwata, “Unveil the Full Potential of Integrated-Back-Contact Perovskite Solar Cells Using Numerical Simulation,” *ACS Appl. Energy Mater.*, vol. 1, no. 3, pp. 970–975, Mar. 2018.

[190] X. Lin *et al.*, “Effect of Grain Cluster Size on Back-Contact Perovskite Solar Cells,” *Adv. Funct. Mater.*, vol. 28, no. 45, pp. 1–9, 2018.

[191] Q. Hou *et al.*, “Back-contact perovskite solar cells with honeycomb-like charge collecting electrodes,” *Nano Energy*, vol. 50, pp. 710–716, 2018.

[192] A. N. Jumabekov, J. A. Lloyd, D. M. Bacal, U. Bach, and A. S. R. Chesman, “Fabrication of Back-Contact Electrodes Using Modified Natural Lithography,” *ACS Appl. Energy Mater.*, vol. 1, no. 3, pp. 1077–1082, Mar. 2018.

[193] Q. Hou, “Semitransparent and back-contact perovskite solar cells for the application in tandem solar cells,” 2019.

[194] Z. Xiao *et al.*, “Giant switchable photovoltaic effect in organometal trihalide perovskite devices,” *Nat. Mater.*, vol. 14, no. 2, pp. 193–197, 2015.

[195] Y. Yuan *et al.*, “Photovoltaic Switching Mechanism in Lateral Structure Hybrid Perovskite Solar Cells,” *Adv. Energy Mater.*, vol. 5, no. 15, pp. 1–7, 2015.

[196] Q. Dong, J. Song, Y. Fang, Y. Shao, S. Ducharme, and J. Huang, “Lateral-Structure Single-Crystal Hybrid Perovskite Solar Cells via Piezoelectric Poling,” *Adv. Mater.*, vol. 28, no. 14, pp. 2816–2821, Apr. 2016.

[197] W. Zhang *et al.*, “Ultrasmooth organic–inorganic perovskite thin-film formation and crystallization for efficient planar heterojunction solar cells,” *Nat. Commun.*, vol. 6, no. 1, p. 6142, May 2015.

[198] F. Huang *et al.*, “Gas-assisted preparation of lead iodide perovskite films consisting of a monolayer of single crystalline grains for high efficiency planar solar cells,” *Nano Energy*, vol. 10, pp. 10–18, 2014.

[199] T. Salim, S. Sun, Y. Abe, A. Krishna, A. C. Grimsdale, and Y. M. Lam, “Perovskite-based solar cells: Impact of morphology and device architecture on device performance,” *J. Mater. Chem. A*, vol. 3, no. 17, pp. 8943–8969, 2015.

[200] Y. Li *et al.*, “A review on morphology engineering for highly efficient and stable hybrid perovskite solar cells,” *J. Mater. Chem. A*, vol. 6, no. 27, pp. 12842–12875, 2018.

[201] G. W. P. Adhyaksa, E. Johlin, and E. C. Garnett, “Nanoscale Back Contact Perovskite Solar Cell Design for Improved Tandem Efficiency,” *Nano Lett.*, vol. 17, no. 9, pp. 5206–5212, 2017.

[202] G. Deluca *et al.*, “Transparent Quasi-Interdigitated Electrodes for Semitransparent Perovskite Back-Contact Solar Cells,” *ACS Appl. Energy Mater.*, vol. 1, no. 9, pp. 4473–4478, Sep. 2018.

[203] M. Wong-Stringer *et al.*, “A flexible back-contact perovskite solar micro-module,” *Energy Environ. Sci.*, vol. 12, no. 6, pp. 1928–1937, 2019.

[204] A. H. Ip *et al.*, “A two-step route to planar perovskite cells exhibiting reduced hysteresis,” *Appl. Phys. Lett.*, vol. 106, no. 14, p. 143902, 2015.

[205] J. Peng *et al.*, “Interface passivation using ultrathin polymer-fullerene films for high-efficiency perovskite solar cells with negligible hysteresis,” *Energy Environ. Sci.*, vol. 10, no. 8, pp. 1792–1800, 2017.

[206] Y. Li *et al.*, “Multifunctional Fullerene Derivative for Interface Engineering in Perovskite Solar Cells,” *J. Am. Chem. Soc.*, vol. 137, no. 49, pp. 15540–15547, 2015.

[207] K. Wojciechowski *et al.*, “Heterojunction modification for highly efficient organic-inorganic perovskite solar cells,” *ACS Nano*, vol. 8, no. 12, pp. 12701–12709, 2014.

[208] C. Bi, Q. Wang, Y. Shao, Y. Yuan, Z. Xiao, and J. Huang, “Non-wetting surface-driven high-aspect-ratio crystalline grain growth for efficient hybrid perovskite solar cells,” *Nat. Commun.*, vol. 6, pp. 1–7, 2015.

[209] G. Yang *et al.*, “Interface engineering in planar perovskite solar cells: Energy level alignment, perovskite morphology control and high performance achievement,” *J. Mater. Chem. A*, vol. 5, no. 4, pp. 1658–1666, 2017.

[210] L. Zuo *et al.*, “Tailoring the interfacial chemical interaction for high-efficiency perovskite solar cells,” *Nano Lett.*, vol. 17, no. 1, pp. 269–275, 2017.

[211] L. Zuo *et al.*, “Enhanced photovoltaic performance of $CH_3NH_3PbI_3$ perovskite solar cells through interfacial engineering using self-assembling monolayer,” *J. Am. Chem. Soc.*, vol. 137, no. 7, pp. 2674–2679, 2015.

[212] H. Bin Kim *et al.*, “Enhancement of photovoltaic properties of CH_3 NH_3 $PbBr_3$

heterojunction solar cells by modifying mesoporous TiO_2 surfaces with carboxyl groups," *J. Mater. Chem. A*, vol. 3, no. 17, pp. 9264–9270, 2015.

[213] H. Nagaoka *et al.*, "Zr incorporation into TiO_2 electrodes reduces hysteresis and improves performance in hybrid perovskite solar cells while increasing carrier lifetimes," *J. Phys. Chem. Lett.*, vol. 6, no. 4, pp. 669–675, 2015.

[214] F. Giordano *et al.*, "Enhanced electronic properties in mesoporous TiO_2 via lithium doping for high-efficiency perovskite solar cells," *Nat. Commun.*, vol. 7, pp. 1–6, 2016.

[215] T. Supasai, N. Rujisamphan, K. Ullrich, A. Chemseddine, and T. Dittrich, "Formation of a passivating $CH_3NH_3PbI_3/PbI_2$ interface during moderate heating of $CH_3NH_3PbI_3$layers," *Appl. Phys. Lett.*, vol. 103, no. 18, pp. 1–4, 2013.

[216] L. Wang, C. McCleese, A. Kovalsky, Y. Zhao, and C. Burda, "Femtosecond time-resolved transient absorption spectroscopy of $CH_3NH_3PbI_3$ perovskite films: Evidence for passivation effect of PbI_2," *J. Am. Chem. Soc.*, vol. 136, no. 35, pp. 12205–12208, 2014.

[217] Y. C. Kim *et al.*, "Beneficial Effects of PbI_2 Incorporated in Organo-Lead Halide Perovskite Solar Cells," *Adv. Energy Mater.*, vol. 6, no. 4, pp. 1–8, 2016.

[218] F. Jiang *et al.*, "Synergistic Effect of PbI_2 Passivation and Chlorine Inclusion Yielding High Open-Circuit Voltage Exceeding 1.15 V in Both Mesoscopic and Inverted Planar $CH_3NH_3PbI_3$(Cl)-Based Perovskite Solar Cells," *Adv. Funct. Mater.*, vol. 26, no. 44, pp. 8119–8127, 2016.

[219] T. J. Jacobsson *et al.*, "Unreacted PbI_2 as a Double-Edged Sword for Enhancing the Performance of Perovskite Solar Cells," *J. Am. Chem. Soc.*, vol. 138, no. 32, pp. 10331–10343, 2016.

[220] F. Liu *et al.*, "Is Excess PbI_2 Beneficial for Perovskite Solar Cell Performance?," *Adv. Energy Mater.*, vol. 6, no. 7, pp. 1–9, 2016.

[221] D. Y. Son *et al.*, "Self-formed grain boundary healing layer for highly efficient $CH_3NH_3PbI_3$ perovskite solar cells," *Nat. Energy*, vol. 1, no. 7, pp. 1–8, 2016.

[222] M. Long *et al.*, "Textured $CH_3NH_3PbI_3$ thin film with enhanced stability for high performance perovskite solar cells," *Nano Energy*, vol. 33, no. December 2016, pp. 485–496, 2017.

[223] Z. Hawash, S. R. Raga, D. Y. Son, L. K. Ono, N. G. Park, and Y. Qi, "Interfacial Modification of Perovskite Solar Cells Using an Ultrathin MAI Layer

Leads to Enhanced Energy Level Alignment, Efficiencies, and Reproducibility," *J. Phys. Chem. Lett.*, vol. 8, no. 17, pp. 3947–3953, 2017.

[224] J. Xu *et al.*, "Perovskite-fullerene hybrid materials suppress hysteresis in planar diodes," *Nat. Commun.*, vol. 6, no. May, pp. 1–8, 2015.

[225] X. Fang *et al.*, "Graphene quantum dot incorporated perovskite films: Passivating grain boundaries and facilitating electron extraction," *Phys. Chem. Chem. Phys.*, vol. 19, no. 8, pp. 6057–6063, 2017.

[226] Y. Shao, Z. Xiao, C. Bi, Y. Yuan, and J. Huang, "Origin and elimination of photocurrent hysteresis by fullerene passivation in $CH_3NH_3PbI_3$ planar heterojunction solar cells," *Nat. Commun.*, vol. 5, 2014.

[227] Z. Zhou *et al.*, "Methylamine-Gas-Induced Defect-Healing Behavior of $CH_3NH_3PbI_3$ Thin Films for Perovskite Solar Cells," *Angew. Chemie - Int. Ed.*, vol. 54, no. 33, pp. 9705–9709, 2015.

[228] Y. Jiang *et al.*, "Post-annealing of $MAPbI_3$ perovskite films with methylamine for efficient perovskite solar cells," *Mater. Horizons*, vol. 3, no. 6, pp. 548–555, 2016.

[229] B. Conings *et al.*, "Structure-Property Relations of Methylamine Vapor Treated Hybrid Perovskite $CH_3NH_3PbI_3$ Films and Solar Cells," *ACS Appl. Mater. Interfaces*, vol. 9, no. 9, pp. 8092–8099, 2017.

[230] W. Zhu *et al.*, "A facile, solvent vapor-fumigation-induced, self-repair recrystallization of $CH_3NH_3PbI_3$ films for high-performance perovskite solar cells," *Nanoscale*, vol. 7, no. 12, pp. 5427–5434, 2015.

[231] A. Abate *et al.*, "Supramolecular halogen bond passivation of organic-inorganic halide perovskite solar cells," *Nano Lett.*, vol. 14, no. 6, pp. 3247–3254, 2014.

[232] N. K. Noel *et al.*, "Enhanced photoluminescence and solar cell performance via Lewis base passivation of organic-inorganic lead halide perovskites," *ACS Nano*, vol. 8, no. 10, pp. 9815–9821, 2014.

[233] Y. Yue *et al.*, "Enhanced Stability of Perovskite Solar Cells through Corrosion-Free Pyridine Derivatives in Hole-Transporting Materials," *Adv. Mater.*, vol. 28, no. 48, pp. 10738–10743, 2016.

[234] S. M. Jain *et al.*, "Frustrated Lewis pair-mediated recrystallization of $CH_3NH_3PbI_3$ for improved optoelectronic quality and high voltage planar perovskite solar cells," *Energy Environ. Sci.*, vol. 9, no. 12, pp. 3770–3782, 2016.

[235] B. Qi and J. Wang, “Fill factor in organic solar cells,” *Phys. Chem. Chem. Phys.*, vol. 15, no. 23, p. 8972, 2013.

[236] P. Tiwana, P. Docampo, M. B. Johnston, L. M. Herz, and H. J. Snaith, “The origin of an efficiency improving ‘light soaking’ effect in SnO_2 based solid-state dye-sensitized solar cells,” *Energy Environ. Sci.*, vol. 5, no. 11, p. 9566, 2012.

[237] L. Yang *et al.*, “Initial Light Soaking Treatment Enables Hole Transport Material to Outperform Spiro-OMeTAD in Solid-State Dye-Sensitized Solar Cells,” *J. Am. Chem. Soc.*, vol. 135, no. 19, pp. 7378–7385, May 2013.

[238] B. O’Regan and D. T. Schwartz, “Large Enhancement in Photocurrent Efficiency Caused by UV Illumination of the Dye-Sensitized Heterojunction TiO_2 /RuLL‘NCS/CuSCN: Initiation and Potential Mechanisms,” *Chem. Mater.*, vol. 10, no. 6, pp. 1501–1509, Jun. 1998.

[239] J. Gilot, M. M. Wienk, and R. A. J. Janssen, “Double and triple junction polymer solar cells processed from solution,” *Appl. Phys. Lett.*, vol. 90, no. 14, p. 143512, Apr. 2007.

[240] S. Sista *et al.*, “Highly Efficient Tandem Polymer Photovoltaic Cells,” *Adv. Mater.*, vol. 22, no. 3, pp. 380–383, Jan. 2010.

[241] M. Herman, M. Jankovec, and M. Topič, “Optimal I-V Curve Scan Time of Solar Cells and Modules in Light of Irradiance Level,” *Int. J. Photoenergy*, vol. 2012, pp. 1–11, 2012.

[242] H. J. Snaith *et al.*, “Anomalous Hysteresis in Perovskite Solar Cells,” *J. Phys. Chem. Lett.*, vol. 5, no. 9, pp. 1511–1515, May 2014.

[243] H. S. Kim and N. G. Park, “Parameters affecting I-V hysteresis of $CH_3NH_3PbI_3$ perovskite solar cells: Effects of perovskite crystal size and mesoporous TiO_2 layer,” *J. Phys. Chem. Lett.*, vol. 5, no. 17, pp. 2927–2934, 2014.

[244] E. L. Unger *et al.*, “Hysteresis and transient behavior in current–voltage measurements of hybrid-perovskite absorber solar cells,” *Energy Environ. Sci.*, vol. 7, no. 11, pp. 3690–3698, 2014.

[245] B. Chen, M. Yang, S. Priya, and K. Zhu, “Origin of J-V Hysteresis in Perovskite Solar Cells,” *Journal of Physical Chemistry Letters*, vol. 7, no. 5. pp. 905–917, 2016.

[246] J. P. Correa Baena *et al.*, “Highly efficient planar perovskite solar cells through band alignment engineering,” *Energy Environ. Sci.*, vol. 8, no. 10, pp. 2928–2934, 2015.

[247] D. A. Jacobs *et al.*, “Hysteresis phenomena in perovskite solar cells: the many and varied effects of ionic accumulation,” *Phys. Chem. Chem. Phys.*, vol. 19, no. 4, pp. 3094–3103, 2017.

[248] Y. Yuan and J. Huang, “Ion Migration in Organometal Trihalide Perovskite and Its Impact on Photovoltaic Efficiency and Stability,” *Acc. Chem. Res.*, vol. 49, no. 2, pp. 286–293, Feb. 2016.

[249] H. Yu, H. Lu, F. Xie, S. Zhou, and N. Zhao, “Native Defect-Induced Hysteresis Behavior in Organolead Iodide Perovskite Solar Cells,” *Adv. Funct. Mater.*, vol. 26, no. 9, pp. 1411–1419, Mar. 2016.

[250] H. Tsai *et al.*, “Optimizing Composition and Morphology for Large-Grain Perovskite Solar Cells via Chemical Control,” *Chem. Mater.*, vol. 27, no. 16, pp. 5570–5576, Aug. 2015.

[251] P. Docampo *et al.*, “Solution Deposition-Conversion for Planar Heterojunction Mixed Halide Perovskite Solar Cells,” *Adv. Energy Mater.*, vol. 4, no. 14, p. 1400355, Oct. 2014.

[252] H.-L. Hsu, C.-P. Chen, J.-Y. Chang, Y.-Y. Yu, and Y.-K. Shen, “Two-step thermal annealing improves the morphology of spin-coated films for highly efficient perovskite hybrid photovoltaics,” *Nanoscale*, vol. 6, no. 17, p. 10281, Jun. 2014.

[253] M. Kim *et al.*, “High-Temperature–Short-Time Annealing Process for High-Performance Large-Area Perovskite Solar Cells,” *ACS Nano*, vol. 11, no. 6, pp. 6057–6064, Jun. 2017.

[254] J. Kim *et al.*, “Nucleation and Growth Control of $HC(NH_2)_2PbI_3$ for Planar Perovskite Solar Cell,” *J. Phys. Chem. C*, vol. 120, no. 20, pp. 11262–11267, May 2016.

[255] V. L. Pool *et al.*, “Thermal engineering of $FAPbI_3$ perovskite material via radiative thermal annealing and in situ XRD,” *Nat. Commun.*, vol. 8, no. 1, p. 14075, Apr. 2017.

[256] A. Dualeh, N. Tétreault, T. Moehl, P. Gao, M. K. Nazeeruddin, and M. Grätzel, “Effect of annealing temperature on film morphology of organic-inorganic hybrid pervoskite solid-state solar cells,” *Adv. Funct. Mater.*, vol. 24, no. 21, pp. 3250–3258, Jun. 2014.

[257] L. Huang, Z. Hu, J. Xu, K. Zhang, J. Zhang, and Y. Zhu, “Multi-step slow annealing perovskite films for high performance planar perovskite solar cells,”

Sol. Energy Mater. Sol. Cells, vol. 141, pp. 377–382, Oct. 2015.

[258] Z. Xiao, Q. Dong, C. Bi, Y. Shao, Y. Yuan, and J. Huang, "Solvent Annealing of Perovskite-Induced Crystal Growth for Photovoltaic-Device Efficiency Enhancement," *Adv. Mater.*, vol. 26, no. 37, pp. 6503–6509, Oct. 2014.

[259] C. H. Chiang, M. K. Nazeeruddin, M. Grätzel, and C. G. Wu, "The synergistic effect of H_2O and DMF towards stable and 20% efficiency inverted perovskite solar cells," *Energy Environ. Sci.*, vol. 10, no. 3, pp. 808–817, 2017.

[260] L. Zuo *et al.*, "Morphology Evolution of High Efficiency Perovskite Solar Cells via Vapor Induced Intermediate Phases," *J. Am. Chem. Soc.*, vol. 138, no. 48, pp. 15710–15716, Dec. 2016.

[261] C. Quarti *et al.*, "Structural and optical properties of methylammonium lead iodide across the tetragonal to cubic phase transition: Implications for perovskite solar cells," *Energy Environ. Sci.*, vol. 9, no. 1, pp. 155–163, 2016.

[262] M. V. Lee *et al.*, "Transamidation of dimethylformamide during alkylammonium lead triiodide film formation for perovskite solar cells," *J. Mater. Res.*, vol. 32, no. 1, pp. 45–55, 2017.

[263] A. Wakamiya *et al.*, "Reproducible fabrication of efficient perovskite-based solar cells: X-ray crystallographic studies on the formation of $CH_3NH_3PbI_3$ layers," *Chem. Lett.*, vol. 43, no. 5, pp. 711–713, 2014.

[264] P. Scherrer, "Bestimmung der größe und der inneren struktur von kolloidteilchen mittels röntgenstrahlen [Determination of the size and internal structure of colloidal particles using X-rays]," *Nachr Ges Wiss Goettingen, Math-Phys Kl.*, vol. 1918, pp. 98–100, 1918.

[265] A. L. Patterson, *X-Ray Diffraction Procedures for Polycrystalline and Amorphous Materials.*, vol. 77, no. 7. 1955.

[266] B. D. Cullity, "Elements of X-Ray Diffraction," *Addison-Wesley*, 1978.

[267] F. T. L. Muniz, M. A. R. Miranda, C. Morilla Dos Santos, and J. M. Sasaki, "The Scherrer equation and the dynamical theory of X-ray diffraction," *Acta Crystallogr. Sect. A Found. Adv.*, vol. 72, no. 3, pp. 385–390, 2016.

[268] N. Bano and R. Ikram, "Histopathological and biochemical assessment of Kidney damage in albino wistar rats treated with cytotoxic platinum compounds in combination with 5-FU," *Pak. J. Pharm. Sci.*, vol. 30, no. 5, pp. 1595–1601, 2017.

[269] H. Do Kim, H. Ohkita, H. Benten, and S. Ito, "Photovoltaic Performance of

Perovskite Solar Cells with Different Grain Sizes," *Adv. Mater.*, vol. 28, no. 5, pp. 917–922, 2016.

[270] X. Ren *et al.*, "Modulating crystal grain size and optoelectronic properties of perovskite films for solar cells by reaction temperature," *Nanoscale*, vol. 8, no. 6, pp. 3816–3822, 2016.

[271] T. Niu *et al.*, "Stable High-Performance Perovskite Solar Cells via Grain Boundary Passivation," *Adv. Mater.*, vol. 30, no. 16, pp. 1–11, 2018.

[272] K. P. Mingard *et al.*, "Int . Journal of Refractory Metals & Hard Materials Comparison of EBSD and conventional methods of grain size measurement of hardmetals," *Int. J. Refract. Met. Hard Mater.*, vol. 27, no. 2, pp. 213–223, 2009.

[273] H. Engqvist and B. Uhrenius, "Determination of the average grain size of cemented carbides," *Int. J. Refract. Met. Hard Mater.*, vol. 21, no. 1–2, pp. 31–35, 2003.

[274] Q. Chen *et al.*, "Controllable self-induced passivation of hybrid lead iodide perovskites toward high performance solar cells," *Nano Lett.*, vol. 14, no. 7, pp. 4158–4163, Jul. 2014.

[275] W. Tress, N. Marinova, T. Moehl, S. M. Zakeeruddin, M. K. Nazeeruddin, and M. Grätzel, "Understanding the rate-dependent J–V hysteresis, slow time component, and aging in $CH_3NH_3PbI_3$ perovskite solar cells: the role of a compensated electric field," *Energy Environ. Sci.*, vol. 8, no. 3, pp. 995–1004, 2015.

[276] W. Li *et al.*, "Montmorillonite as bifunctional buffer layer material for hybrid perovskite solar cells with protection from corrosion and retarding recombination," *J. Mater. Chem. A*, vol. 2, no. 33, pp. 13587–13592, 2014.

[277] S. N. Habisreutinger, N. K. Noel, H. J. Snaith, and R. J. Nicholas, "Investigating the Role of 4-Tert Butylpyridine in Perovskite Solar Cells," *Adv. Energy Mater.*, vol. 7, no. 1, pp. 1–8, 2017.

[278] W. Tress *et al.*, "Interpretation and evolution of open-circuit voltage, recombination, ideality factor and subgap defect states during reversible light-soaking and irreversible degradation of perovskite solar cells," *Energy Environ. Sci.*, vol. 11, no. 1, pp. 151–165, 2018.

[279] H. Seidel, L. Csepregi, A. Heuberger, and H. Baumgärtel, "Anisotropic Etching of Crystalline Silicon in Alkaline Solutions II. Influence of Dopants," *J.*

Electrochem. Soc., vol. 137, no. 11, pp. 3626–3632, 1990.

[280] Y. Inomata, K. Fukui, and K. Shirasawa, “Surface texturing of large area multicrystalline silicon solar cells using reactive ion etching method,” *Sol. Energy Mater. Sol. Cells*, vol. 48, no. 1–4, pp. 237–242, 1997.

[281] D. H. Macdonald *et al.*, “Texturing industrial multicrystalline silicon solar cells,” *Sol. Energy*, vol. 76, no. 1–3, pp. 277–283, Jan. 2004.

[282] G. Beadie, M. Brindza, R. A. Flynn, A. Rosenberg, and J. S. Shirk, “Refractive index measurements of poly(methyl methacrylate) (PMMA) from 0.4–1.6μm,” *Appl. Opt.*, vol. 54, no. 31, pp. 139–143, 2015.

[283] P. Löper *et al.*, “Complex refractive index spectra of $CH_3NH_3PbI_3$ perovskite thin films determined by spectroscopic ellipsometry and spectrophotometry,” *J. Phys. Chem. Lett.*, vol. 6, no. 1, pp. 66–71, 2015.

[284] H. Yu, F. Wang, F. Xie, W. Li, J. Chen, and N. Zhao, “The role of chlorine in the formation process of "$CH_3NH_3PbI_{3-x}Cl_x$ perovskite,” *Adv. Funct. Mater.*, vol. 24, no. 45, pp. 7102–7108, 2014.

[285] T. Dittrich, C. Awino, P. Prajongtat, B. Rech, and M. C. Lux-Steiner, “Temperature Dependence of the Band Gap of $CH_3NH_3PbI_3$ Stabilized with PMMA: A Modulated Surface Photovoltage Study,” *J. Phys. Chem. C*, vol. 119, no. 42, pp. 23968–23972, 2015.

[286] S. N. Habisreutinger, T. Leijtens, G. E. Eperon, S. D. Stranks, R. J. Nicholas, and H. J. Snaith, “Carbon nanotube/polymer composites as a highly stable hole collection layer in perovskite solar cells,” *Nano Lett.*, vol. 14, no. 10, pp. 5561–5568, Oct. 2014.

[287] T. Leijtens, G. E. Eperon, N. K. Noel, S. N. Habisreutinger, A. Petrozza, and H. J. Snaith, “Stability of metal halide perovskite solar cells,” *Adv. Energy Mater.*, vol. 5, no. 20, p. 1500963, Oct. 2015.

[288] B. Philippe *et al.*, “Chemical and electronic structure characterization of lead halide perovskites and stability behavior under different exposures-A photoelectron spectroscopy investigation,” *Chem. Mater.*, vol. 27, no. 5, pp. 1720–1731, 2015.

[289] Z. Chu *et al.*, “Impact of grain boundaries on efficiency and stability of organic-inorganic trihalide perovskites,” *Nat. Commun.*, vol. 8, no. 1, pp. 1–8, 2017.

[290] L. A. A. Pettersson, L. S. Roman, and O. Inganäs, “Modeling photocurrent action spectra of photovoltaic devices based on organic thin films,” *J. Appl.*

Phys., vol. 86, no. 1, pp. 487–496, 1999.

[291] P. B. Johnson and R. W. Christy, “Optical constants of the noble metals,” *Phys. Rev. B*, vol. 6, no. 12, pp. 4370–4379, 1972.

[292] A. D. Rakić, A. B. Djurišić, J. M. Elazar, and M. L. Majewski, “Optical properties of metallic films for vertical-cavity optoelectronic devices,” *Appl. Opt.*, vol. 37, no. 22, p. 5271, 1998.

[293] I. H. Malitson, “Refraction and Dispersion of Synthetic Sapphire,” *J. Opt. Soc. Am.*, vol. 52, no. 12, p. 1377, 1962.

[294] J. M. Ball *et al.*, “Optical properties and limiting photocurrent of thin-film perovskite solar cells,” *Energy Environ. Sci.*, vol. 8, no. 2, pp. 602–609, 2015.

[295] J. R. DeVore, “Refractive Indices of Rutile and Sphalerite,” *J. Opt. Soc. Am.*, vol. 41, no. 6, p. 416, 1951.

[296] J. Peng *et al.*, “A Universal Double-Side Passivation for High Open-Circuit Voltage in Perovskite Solar Cells: Role of Carbonyl Groups in Poly(methyl methacrylate),” *Adv. Energy Mater.*, vol. 8, no. 30, p. 1801208, Oct. 2018.

[297] S. H. Turren-Cruz, A. Hagfeldt, and M. Saliba, “Methylammonium-free, high-performance, and stable perovskite solar cells on a planar architecture,” *Science (80-.).*, vol. 362, no. 6413, pp. 449–453, Oct. 2018.

[298] F. Wang *et al.*, “Highly efficient and stable perovskite solar cells by interfacial engineering using solution-processed polymer layer,” *J. Phys. Chem. C*, vol. 121, no. 3, pp. 1562–1568, Jan. 2017.

[299] C. Wu *et al.*, “Highly-Stable Organo-Lead Halide Perovskites Synthesized Through Green Self-Assembly Process,” *Sol. RRL*, vol. 2, no. 6, p. 1800052, 2018.

9. Nomenclature

2AP – 2-amylpyridine

4AP – 4-amylpyridine

AFM – atomic force microscope

AR5 – 5th Assessment Report on Climate Change

ARC – antireflective coating

BC – back – contact

CBZ – chlorobenzene

CIGS – copper indium gallium selenide

COP – Conference of Parties to United Nations Framework Convention on Climate Change

DMF – N-N dimethylformamide

DSSCs – dye – sensitized solar cells

ER – evaporation rate

ESL – electron selective layer

FF – fill factor

FFCIP – emissions of carbon dioxide through combustion of fossil fuels and industrial processes

FOLU – emissions of carbon dioxide through forestry and other land use

FTO – fluorine doped tin oxide

FWHM – full width at half maximum

GBs – grain boundaries

GHGs – greenhouse gasses

HQIBC – honeycomb quasi-interdigitated back-contact electrodes

HSL – hole selective layer

IBC – interdigitated back-contact

IPCC – Intergovernmental Panel on Climate Change

IPFB – iodopentafluorobenzene

ITO – indium tin oxide

Li-TFSI – lithium-bis(trifluoromethanesulfonyl)imide

$MAPbI_3$ – methylammonium lead iodide

MPP – maximum power point

NDCs – nationally determined contributions

PA – Paris Agreement

PCBM – [6,6]-phenyl C61 butyric acid methyl ester

PCE – power conversion efficiency

PEDOT:*PSS* – poly(3,4-ethylenedioxythiophene)-poly(styrenesulfonate)

PL – photoluminescence

PMMA – poly(methyl methacrylate)

PSCs – perovskite solar cells

PV – photovoltaic

QIBC – quasi-interdigitated back-contact

RE – renewable energy

ROI – return on investment time

SC – solar cells

SEM – Scanning electron microscope

Spiro-OMeTAD – 2,2',7,7'-Tetrakis-(N,N-di-p- methoxyphenyl-amine)9,9'-spirobifluorene

SR1.5 – Special Report on "Global Warming of 1.5°C"

TBP – 4-tert-butyl pyridine

TCO – transparent conductive oxide

TM – transfer matrix

TSC – tandem solar cell

UNFCCC – United Nations Framework Convention on Climate Change

XRD – X-ray diffraction